# SYNCHROTRON IMAGING OF BOVINE AND HUMAN OVARIES *EX VIVO*

A Thesis Submitted to the College of

Graduate Studies and Research

In Partial Fulfillment of the Requirements

For the Degree of Master of Health Sciences

In the Department of Obstetrics, Gynecology and Reproductive Science

University of Saskatchewan

Saskatoon

By

UPEKHA PIYUMRAMINI BASNAYAKA MUDIYANSELAGE

© Copyright Upekha Piyumramini Basnayaka Mudiyanselage, July 2013.
All rights reserved.

PERMISSION TO USE

In presenting this thesis in partial fulfilment of the requirements for a Postgraduate degree from the University of Saskatchewan, I agree that the Libraries of this University may make it freely available for inspection. I further agree that permission for copying of this thesis in any manner, in whole or in part, for scholarly purposes may be granted by the professor or professors who supervised my thesis work or, in their absence, by the Head of the Department or the Dean of the College in which my thesis work was done. It is understood that any copying or publication or use of this thesis or parts thereof for financial gain shall not be allowed without my written permission. It is also understood that due recognition shall be given to me and to the University of Saskatchewan in any scholarly use which may be made of any material in my thesis.

Requests for permission to copy or to make other use of material in this thesis in whole or part should be addressed to:

Head of the Department of Obstetrics, Gynecology, and Reproductive Sciences
College of Medicine
University of Saskatchewan
Saskatoon, Saskatchewan
S7N 0W8

## ABSTRACT

**Background and Rationale:** Reproductive dysfunction affects more than 15% of Canadian women; however, the underlying causes remain largely unknown. Ultrasonography is the most commonly used research and diagnostic tool for imaging the ovaries and uterus. However, current ultrasonographic techniques allow the detection of ovarian structures (eg. follicles, corpora lutea) at diameters of only ≥2 mm. The increased effectiveness of synchrotron technology for imaging ovaries in comparison to conventional imaging methods is currently unknown.

**Overall Objective:** The overall objective of this research was to determine the effectiveness of synchrotron techniques for imaging ovaries. We hypothesized that synchrotron techniques would provide greater contrast for visualizing structural details of follicles, corpora lutea (CL), and cumulus oocyte complexes (COC), compared to conventional ultrasonography.

**Materials and Methods:** Three studies were conducted to evaluate phase-contrast based synchrotron imaging methods. The first study involved Diffraction Enhanced Imaging (DEI) of bovine ovaries (n=6). The second study involved Propagation-Based Computed Tomography (PB-CT) imaging of bovine (n=4) and human ovaries (n=4). A third, preliminary study was conducted to explore the use of Talbot Grating Interferometry (TGI-CT) imaging of bovine (n=1) and human ovaries (n=1). Fresh and formalin-fixed bovine and human ovaries were imaged without or with contrast injection into the ovarian artery. Following synchrotron imaging, all ovarian samples were evaluated using diagnostic ultrasonography and histology. Images obtained using synchrotron techniques, ultrasonography and histology were qualitative and quantitatively compared.

**Results:** DEI allowed the identification of 71% of follicles ≥2 mm and 67% of CL detected using ultrasonography. Mean follicle diameter was similar between DEI (9.6 ± 2.4 mm), ultrasonography (9.0 ± 2.6 mm), and histology (6.9 ± 1.9 mm) for fresh ovaries without contrast ($P = 0.70$). Likewise, no difference in CL diameter was detected between DEI (11.64 ± 1.67 mm), ultrasonography (9.34 ± 0.35 mm), and histology (9.6 ± 0.4 mm), ($P = 0.34$). Antral

Follicle Count (AFC; ≥2 mm) was similar between ultrasonography (6.5 ± 0.7 mm, fresh with no contrast; 6.5 ± 2.5 mm, preserved with no contrast) and DEI ( 4.5 ± 0.5 mm, fresh with no contrast; 6.5 ± 0.50 mm, preserved with no contrast) ($P > 0.05$). However, the contrast resolution for differentiating follicles and CL was inferior with DEI compared to ultrasonography. Small antral follicles <2 mm, cell layers comprising the follicle wall and COC were not detected using either DEI or ultrasonography.

PB-CT imaging enabled the visualization of 100% of follicles ≥2 mm and 100% of CL that were detected with ultrasonography. CL containing a central cystic cavity were identified using PB-CT; however, CL without a central cystic cavity were not well-visualized. Mean follicle and luteal diameters did not differ among PB-CT, ultrasonography and histology ($P>0.05$). PB-CT was superior to ultrasonography for detecting small antral follicles <2 mm in bovine ovaries ($P = 0.04$), and the granulosa and theca cell layers of the follicle wall in bovine and human ovaries ($P < 0.0001$). However, TGI-CT images exhibited greater contrast resolution for visualizing small and large antral follicles, CL, and the cell layers of the follicle wall compared to both PB-CT and ultrasonography. High contrast structures resembling COC were detected with both PB-CT and TGI-CT, but not with ultrasonography. Only TGI-CT permitted the visualization of the oocyte within the COC in fresh and preserved ovaries.

**Conclusions:** DEI was inferior to ultrasonography for detecting ovarian follicles and CL. PB-CT was superior to ultrasonography for visualizing follicles <2mm, COC, and the cell layers of the follicle wall. However, PB-CT was as effective as ultrasonography for detecting and measuring follicles ≥2 mm and cystic CL. Preliminary findings suggest that TGI-CT provides the greatest contrast for imaging both ovarian macro- and microanatomy compared to PB-CT, DEI, and ultrasonography.

## ACKNOWLEDGEMENTS

The research presented in this thesis would not have been possible without the collaboration of many people. I would foremost like to thank my primary supervisor, Dr. Angela Baerwald, for her continuous support, guidance and friendship she has given me in the past few years. I would also like to express my gratitude to my committee members, Drs. Dean Chapman, Gregg Adams, Roger Pierson, and Rani Kanthan for always finding the time to assist with my research. Thank you to Drs. Rajni Chibbar, Jaswant Singh, and Darren Nesbitt for assisting with the histology work of my thesis. I am very thankful for the assistantship I received from faculty members at the Canadian Light Source (CLS), including Drs. Tomasz Wysokinski, George Belev, Adam Webb and Zhouping Wei. I am also very grateful for the scientists (Drs. Naoto Yagi, Kentaro Uesugi and Masato Hoshino) at the SPring-8 synchrotron facility in Japan who assisted us with the imaging of ovaries using the new x-ray grating technique.

I would like to express my deepest appreciation for the Reproductive Science and Medicine Research group, as well as the CIHR-THRUST (Canadian Institutes of Health Research-Training Grant in Health Research Using Synchrotron Techniques) group for making my graduate years worthwhile and challenging. I enjoyed the intellectually stimulating seminars and conferences, and the fun social events that were organized by both groups. I would specially like to thank the fellow graduate students of the Reproductive Biology Research Unit, including Heidi Vanden Brink, Heather Allaway, Shani Serrao, and Sandhya Roy. Whether it was a simple smile or an offer of advice, you have all helped me to develop as a researcher and as an individual.

Thank you to my beloved parents (Thilak Basnayaka and Devini de Silva), brother (Pubudu Basnayaka), and my fiancé (Buddhika Menikge) for showering me with unconditional love, support and encouragement. I would also like to extend my warmest gratitude towards my relatives and friends who have helped me throughout this wonderful journey.

Finally, I would like to thankfully acknowledge the University of Saskatchewan, CIHR-THRUST, and Mitacs-Accelerate for funding my graduate work.

**DEDICATION**

*This thesis is dedicated to my loving parents,*
*Thilak and Devini,*
*and my wonderful fiancé, Buddhika.*

## TABLE OF CONTENTS

## LIST OF TABLES

## LIST OF FIGURES

## LIST OF ABBREVIATIONS

| | |
|---|---|
| G2 | Absorbing Analyzer Grating |
| A-mode | Amplitude Mode |
| ANOVA | Analysis of Variance |
| AFC | Antral Follicle Count |
| BMIT | BioMedical Imaging and Therapy |
| B-mode | Brightness Mode |
| CIHR | Canadian Institutes of Health Research |
| CLS | Canadian Light Source |
| cm | Centimeter |
| CCD | Charged Coupled Device |
| CIHR-THRUST | CIHR-Training Grant in Health Research Using Synchrotron Techniques |
| CE | Common Era |
| CT | Computed Tomography |
| CNR | Contrast-to-Noise Ratio |
| CA | Corpus Albicans |
| CL | Corpus Luteum |
| COC | Cumulus Oocyte Complex |
| DEI | Diffraction Enhanced Imaging |
| DICOM | Digital Imaging and Communications in Medicine |
| 2D | 2-Dimensional |
| 3D | 3-Dimensional |
| e-beam | Electron beam |
| FSH | Follicle Stimulating Hormone |
| GeV | Gigaelectron Volt |
| Hz | Hertz |
| IL | Illinois |
| IOI | Interovulatory Interval |
| keV | Kiloelectron Volt |
| kHz | Kilohertz |
| LH | Luteinizing Hormone |
| MA | Massachusetts |
| MeV | Megaelectron Volt |
| MHz | Megahertz |
| µm | Micrometer |
| mA | Milliampere |
| mGy | Milligray |
| mm | Millimeter |
| M-mode | Motion Mode |
| nm | Nanometer |
| NY | New York |
| G1 | Phase Grating |
| PB-CT | Propagation-Based Computed Tomography |

| | |
|---|---|
| PBI | Propagation-Based Imaging |
| n | Sample Size |
| SNR | Signal-to-Noise Ratio |
| SPSS | Statistical Package for the Social Sciences |
| SPring-8 | Super Photon Ring – 8 GeV |
| mSv | Millisievert |
| TGI | Talbot Grating Interferometry |
| UK | United Kingdom |
| USA | United States of America |

# Chapter 1

# GENERAL INTRODUCTION

## 1.1 The Human Ovary

### 1.1.1 Historical Perspective on Human Ovarian Research

The study of the structure and function of the human ovary has been of interest to scientists and clinicians for several decades. The ovaries house the female germ cells, oocytes, which are essential for procreation. Soranus of Ephesus (Greece, 100 CE) described the ovaries as a didymi ("paired organs") with a loose texture, but concluded that the female seed (egg) had no role in reproduction since it was excreted with urine [1, 2]. The term "ovary" was later created by Girolamo Fabrici d'Aquapendente (Italy, 1600) [3]. The follicles (i.e., the fluid-filled sacs containing the oocytes within the ovary) were first described by Andreas Vesalius (Belgium) in the 1540s [3]. Mature ovarian follicles were characterized by Regnier de Graaf (Netherlands, 1672); however, de Graaf had assumed that the follicle itself was the egg [2, 3]. The distinction between the egg and the follicle was made in 1827 by Karl Ernst von Baer (Russia)[2, 3]. During the nineteenth century, surgical examination of the reproductive organs allowed a better understanding of the structures within the ovaries, including antral follicles, corpora lutea (CL), and their associated vasculature. Since then, research has been conducted to understand ovarian anatomy, physiology (i.e., follicle development, luteal function, menstrual cyclicity), pathophysiology (i.e., ovarian tumors, endometriosis, polycystic ovary syndrome), as well as the hormonal and non-hormonal control of reproduction during the use of contraception or assisted reproduction.

### 1.1.2 Anatomy of the Ovary

The human ovaries are two oval shaped organs located in the lower abdomen, posterior to the bladder and anterior to the rectum. The ovaries are attached to the uterus below the cornua (i.e., uterine horn) via the proper ovarian ligament and to the pelvic walls by the suspensory ligaments [4]. The ovaries are about 3 cm long, 2 cm wide and 1.5 cm thick [5]. The internal anatomy of the human ovary is shown in Figure 1.1. The ovary is divided into the outer cortex

and the inner medulla, which are collectively referred to as the stroma [6, 7]. The stroma is composed of connective tissue, blood vessels and nervous tissues that permeate both the medulla and cortex. The cortex which constitutes the majority of the ovary contains the follicles and CL [8]. Follicles, at various developmental stages, may be present on a given day during the menstrual cycle (described later). In general, a mature follicle is enclosed by a wall consisting of theca and granulosa cell layers which encapsulates a fluid-filled cavity (referred to as the antrum). The oocyte is surrounded by a specialized layer of granulosa cells (termed the cumulous oophorus), and is attached to the follicle wall [7]. The medulla contains numerous blood and lymph vessels that branch out into the cortex to supply the growing follicles and CL [6, 7, 9]. The ovarian cortex is enclosed by a dense connective tissue known as the tunica albuginea [3, 6, 7]. The surface or germinal epithelium is present on the surface of the ovary (i.e., above the tunica albuginea) and is composed a single layer of cuboidal or columnar epithelium [3, 7].

The functioning of the ovary is maintained by its vasculature, innervation and lymphatic circulation. The ovarian artery, branching from the abdominal aorta, enters the ovary at the hilum and provides the primary blood supply to the ovary [4, 10]. The left and right ovarian veins lie parallel to the arterial system and drain into the renal vein and inferior vena cava, respectively [4, 11]. Antral follicles contain a capillary network in the theca cell layer of the follicular wall that promotes follicular growth [8, 12, 13]. The granulosa cell layer is considered avascular until after ovulation or during atresia [11]. Ovarian vasculature plays a crucial role in follicle growth, ovulation and luteal development [12, 14]. Ovarian innervation arises superiorly from the intermesenteric nerves and renal plexus, intermediately from the hypogastric nerve, and inferiorly from the pelvic plexus [15]. The majority of the nerves of the ovary are adrenergic with the main neurotransmitter being noradrenaline [8, 11]. The extrinsic nerves enter the ovary through the hilar perivascular plexus and regulate blood flow [16-18]. The lymphatic vessels run along the surface of the ovary and also line the outside of growing follicles [11]. The lymph vessels in the ovary excrete unnecessary hormones and tissue debris [19].

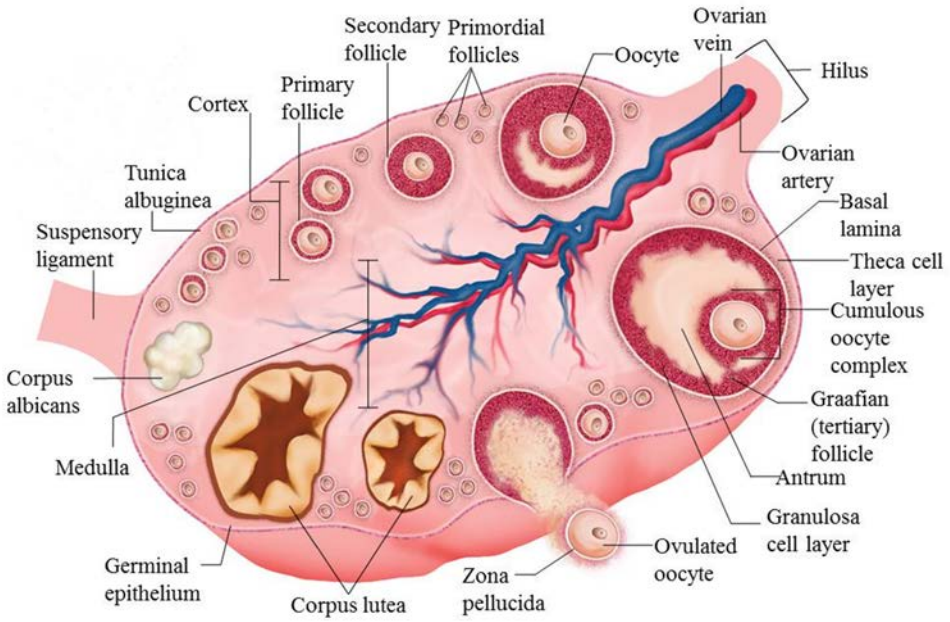


**Figure 1.1:** Anatomy of the human ovary. **(**Basnayaka, et al., 2013, unpublished)

### 1.1.3 Human Ovarian Physiology

#### 1.1.3.1 Pre-Antral Folliculogenesis

The development of ovarian follicles occurs in four stages throughout a woman's menstrual cycle. During the earliest stage, the follicles are termed primordial follicles. A primordial follicle contains a primary oocyte (25 µm in diameter) which is surrounded by a single layer of squamous follicular cells [7, 8, 20]. The primary oocyte is arrested at prophase I of meiosis until ovulation and contains of a large, asymmetrically placed nucleus and a homogeneous cytoplasm [7, 21-23]. Primordial follicle growth is characterized by an increase in oocyte size as well as the growth and proliferation of follicular cells, the granulosa and theca cells [7]. A primary follicle develops in the second stage of follicle growth and is characterized by a multilayered arrangement of cuboidal granulosa cells around the oocyte [7, 24]. During the third stage of follicular growth, theca interna and theca externa cell layers form within the follicle wall to form secondary follicles [22]. The theca interna cell layer is highly-vascular and contains cuboidal-shaped steroidal secretory cells, fibroblasts, and collagen bundles [7, 21, 22, 25-27]. The connective tissue cells of the theca externa are spindle-shaped and surrounded by collagen fibers and some smooth muscle [7, 25, 27]. A thin basement membrane separates the

theca interna and externa cell layers from the granulosa cells [21, 22, 25, 28]. Secondary follicles undergo major changes during the late tertiary stage of follicular development, including expansion of the oocyte to about 120 µm, development of inner cellular components (i.e. mitochondria, endoplasmic reticulum, and golgi complexes), and the formation of a zona pellucida [7]. The zona pellucida is an extracellular matrix containing glycoproteins that surround the oocyte [6-8].

Pre-antral follicle development occurs independent of gonadotropins, FSH and LH, and is regulated by paracrine and autocrine stimuli, such as growth factors [29]. Hormonal and non-hormonal regulation of follicular development is not the focus of this thesis and is therefore not reviewed in detail.

#### 1.1.3.2 Antral Ovarian Folliculogenesis

An antral cavity will begin forming inside the follicles when they are 0.2 mm in diameter [30]. Tertiary follicles develop during the fourth stage of development [6, 8, 9, 31]. Tertiary follicles are also referred to as Graafian follicles. The total diameter of a tertiary follicle ranges from 8-30 mm in diameter [6, 31]. The antrum is filled with follicular fluid which contains growth factors, hyaluronate, plasminogen, fibrinogen, anticoagulants, and steroids that provide a nourishing environment for the growth of the oocyte [7, 8]. The granulosa cell layer differentiates into two separate components: the mural granulosa cells of the follicular wall, and the cumulus oophorus (i.e., cells that aggregate around the oocyte), [6, 7, 31]. The cumulus oophorus and oocyte are collectively known as the cumulus-oocyte complex (COC) [8].

The final stage of follicle development involves the cyclic formation of antral follicles throughout the menstrual cycle [32]. The human menstrual cycle begins at the time of menarche (i.e., 8.5 – 13 years) and lasts until menopause (i.e., approximately 51 years) [33, 34]. The menstrual cycle in women is divided into two main phases: (1) follicular phase and (2) luteal phase. The average menstrual cycle occurs over 26 – 35 days [35]. The follicular and luteal phases of a woman's menstrual cycle can vary from 10-23 days and 8-17 days, respectively [36]. Antral ovarian follicles develop in either 2 or 3 waves during a woman's menstrual cycle [32, 37-39]. Each antral follicle wave of the cycle may also be referred to as a "recruited cohort" [37, 38]. The wave-model for follicular development in reproductive age women is similar to that of cows and mares, where the final wave of the interovulatory interval (IOI) is ovulatory and all

preceding waves of the IOI are anovulatory [5, 37, 40]. Major waves are those in which a dominant follicle is preferentially selected for growth [40]. Minor waves are characterized by the absence of a dominant follicle [40]. Therefore, the final 'ovulatory' wave of the IOI is major, while the anovulatory waves which precede the ovulatory wave may be major or minor.

Emergence of the first follicular wave of the menstrual cycle occurs at a diameter of approximately 4 - 5 mm, and selection of the dominant follicle occurs at a diameter of approximately 10 mm [38]. The dominant follicle is a tertiary follicle with a diameter of 20 mm prior to ovulation [7, 8, 31]. Graafian follicles prior to ovulation contain a serrated granulosa cell layer and a fragmented basal lamina [21].

FSH levels rise during the late-luteal-early follicular phase to induce emergence of a follicular wave [41]. Inhibin B production from follicles of the recruited cohort or wave act to suppress FSH concentrations [42]. At the time of selection of the dominant follicle in the mid-follicular phase, FSH is low and estradiol gradually increases. At the time of selection, there is also a transition from inhibin B to inhibin A production and a shift from FSH to LH responsiveness [41]. Increased estradiol levels from the developing follicles during the follicular phase stimulates the growth of the endometrial lining to prepare for a potential pregnancy [43]. Pre-ovulatory surges in LH and FSH occur at the end of the follicular phase in response to positive feedback from dominant follicle estradiol production [37]. The rise in both FSH and LH occur approximately 24 hours after the surge in estradiol [21]. Ovulation occurs approximately 36 to 40 hours following the LH surge [44]. In some women, the first wave of the follicular phase is anovulatory and a second wave develops in the mid-follicular phase to result in ovulation. A second rise in FSH has been associated with emergence of the second follicular wave [38].

The pre-ovulatory FSH surge induces another wave of follicle development in the early luteal phase, at which time the CL is developing. By the mid-luteal phase, LH and FSH are low while progesterone and estradiol concentrations reach peak concentrations [37, 45]. The regression of the CL in the late-luteal stage is marked by a decrease in both progesterone and estradiol concentrations and a subsequent rise in FSH [45]. The loss of progesterone and estradiol leads to the shedding of the endometrium [35]. With the rise in FSH, a new wave emerges and the follicular phase of the next menstrual cycle is initiated [35, 37].

#### 1.1.3.3 Ovulation

Ovulation is the process by which the oocyte is released from the ovarian follicle. The pre-ovulatory LH surge induces a series of morphologic and physiologic changes in the follicle and oocyte. Morphological changes include the expansion of the cumulus, increased blood supply to the theca intern, folding of the granulosa cell layer and fragmentation of the basal lamina [8, 21]. One of the most conspicuous indications of imminent ovulation is the cone-like stigma that forms on the surface of the follicle wall [8, 46]. The oocyte becomes detached from the Graafian follicle wall approximately 25 minutes prior to ovulation [47]. An inflammatory process stimulates the degradation and rupture of the follicle wall under a steady intrafollicular pressure [46]. Following the LH surge, the oocyte completes the first meiotic division and the first polar body is released [48]. The oocyte that is ovulated is therefore in the metaphase II stage of meiotic development [44]. The COC along with the antral fluid is released into the peritoneal cavity towards the fimbria of the fallopian tube [7, 8, 48]. The time required for ovulation is highly variable, but on average, occurs within 10 minutes [49]. Following ovulation, the remaining cells of the follicular wall undergo vascular and endocrinological changes to form the CL [45, 50, 51]

#### 1.1.3.4 Luteogenesis and Luteolysis

The CL is composed of endothelial cells and luteinized theca and granulosa cells as well as immune and fibroblast cells [7, 8, 50, 52]. Granulosa-lutein cells are modified granulosa cells [22, 53]. Theca-lutein cells are modified theca cells located on the periphery of the CL [22, 53]. Compared to granulosa-lutein cells, theca-lutein cells contain more lipid droplets and are more abundant in the CL [53]. The luteal structure is known as a corpus hemorrhagicum when blood accumulates inside the cavity during and/or following follicle rupture [54]. Peak luteal diameter and optimal blood flow to the CL is observed 7 days after ovulation [55]. The mature CL is 25-40 mm in diameter and appears yellow [52, 54]. The term ‘corpus luteum’ is Latin for “yellow body”. The CL functions as a temporary endocrine gland as it is the main source of steroid hormones (i.e., progesterone and estradiol) during early pregnancy [7, 50].

If conception occurs, the CL increases in size until approximately the $12^{th}$ week of gestation, at which time the placenta has formed to maintain the pregnancy [56]. In the absence of conception, the CL begins to regress approximately 7 days post-ovulation [7, 8, 52].

Luteolysis is associated with a decline in progesterone concentration, as well as apoptosis and tissue involution [8]. The regressing CL is referred to as the corpus albicans (CA), which is Latin for 'white body' [7]. The CA appears as a small mass of amorphous scar tissue that may persist in the ovary for several months post-ovulation [56].

#### 1.1.3.5 Follicular Atresia

The number of follicles within the human ovary is constantly changing. Women are born with approximately 2 million resting follicles, but only hundreds of follicles remain at the time of menopause [57]. Approximately 400-500 follicles will ovulate during a women's lifetime, if she is not pregnant or taking oral contraceptives [7, 8, 58]. Follicular regression or 'atresia' is a physiologically-normal phenomenon that occurs throughout a woman's lifetime. The rate of atresia is thought to be about 1000 follicles per menstrual cycle [59]; more than 90% of follicles are destined for atresia throughout a woman's lifetime. Follicle atresia begins at the $24^{th}$ week of gestation and is influenced by factors such as health, age, stage of follicular development, environmental factors, and genetics [21, 57, 60, 61]. Atretic changes in the granulosa cells precede oocyte degeneration [28, 62, 63]. Granulosa cells near the antrum develop pyknotic nuclei and are shed into the antral cavity; the remaining granulosa cells undergo nuclear condensation and are phagocytosed [27, 60]. Other changes that indicate follicular atresia are reduced translucency and an increased androgen to estrogen ratio in the follicular antrum [21]. Later stages of follicular atresia are characterized by the development of apoptotic bodies and cytoplasmic droplets in granulosa cells, hypertrophied theca interna cells, and a hyalanized zona pellucida [21, 27]. The separation of the COC and disintegration of cellular organelles are also apparent [21, 64]. Macrophages and neutrophils eventually invade the atretic follicles and remove debris from the ovary [21]. Factors known to promote atresia include hyophysectomy, antibodies to gonadotrophins, ligation of the ovarian artery, exposure to environmental contaminants, and smoking [21, 65].

The number of pre-antral follicles within the ovaries is referred to as the ovarian reserve. With age, follicular atresia and to a lesser degree ovulation, lead to a continued depletion of the ovarian reserve. Menopause refers to the stage of a woman's cycle when menstruation ceases [30]. The number of antral follicles (Antral Follicle Count, AFC) that can be visualized ultrasonographically has been shown to be a marker of the ovarian reserve [37, 66, 67]. AFC is

used to predict the ovarian response to assisted reproductive therapy. AFC is also used to predict the timing of the onset of menopause [68-71].

#### 1.1.3.6 Aging and Ovarian Function

Follicular wave dynamics change as women approach menopause. It has been shown that as women age, luteal phase dominant follicles emerge earlier relative to ovulation, grow larger and for a longer period of time compared to women of reproductive age [72].

The ovary of a postmenopausal woman is smaller in weight and volume and shriveled in appearance compared to a younger ovary due to the depletion of follicles [8, 73]. Preovulatory oocytes in the aging ovary are more likely to contain cellular and chromosomal defects [74]. The aging ovary is associated with the development of excess fibrous connective and scar tissues in the ovarian stroma [8]. An overall reduction in blood flow to the ovary related to reduced vascular network and thickened vessel walls are also observed in aging ovaries [8]. The surface epithelium of the ovary in older women contains fewer and flatter cells with shorter microvilli [8]. Smoking has been found to be an environmental factor that accelerates aging of the ovary by inducing follicular apoptosis through intrafollicular oxidative stress [8, 75]. These age-related changes in the ovary can hinder oocyte development and thereby compromise pregnancy outcomes.

## 1.2 The Bovine Ovary

### 1.2.1 The Bovine Model for Studying Human Ovaries

The conduct of human reproductive studies is often challenged by ethical limitations. As a result, the bovine species has been established as a model to study ovarian anatomy and physiology in women of reproductive age, advanced reproductive age, and those undergoing assisted reproduction [5, 37, 38, 76]. Both human and bovine species are monovular and polycyclic [5]. Physical characteristics of cow ovaries are similar to human ovaries, including size (i.e., 3 x 2 x 1.5 cm). Furthermore, the growth dynamics of follicles and CL are similar between species [5]. Pathological conditions, such as follicular cysts and luteinized anovulatory follicles, are also observed in both bovine and human species [5]. Research in both cows [77]

and women [78] have shown that quantitative ultrasonographic image analyses of follicles and CL corresponds with their physiological status.

### 1.2.2 Estrus versus Menstrual Cycle

In cows, the reproductive cycle is based on “estrus”, the period of increased sexual receptivity that occurs prior to ovulation [37]. The estrus cycle lasts for an average of 21 days and is divided into four mains stages: (i) proestrus, (ii) estrus, (iii) metestrus, and (iv) diestrus [79-81]. The proestrus and estrus stages are collectively referred to as the follicular phase [82]. Likewise, the metestrus and diestrus phases are known as the luteal phase [82]. The follicular and luteal phases of cows consist of 3-4 days and 16-18 days, respectively [37]. Ovulation and behavioral patterns indicative of sexual receptivity (i.e., heat and vaginal discharge) occurs during the estrus phase [80, 82]. Signs of sexual receptiveness have also been observed in humans but are less obvious compared to cows [83].

Endocrinologic changes during the estrus cycle are generally consistent with those during the human menstrual cycle [37]. Proestrus is marked by the regression of the CL and the development of the preovulatory follicle [80]. Proestrus and estrus stages include decreased progesterone from the CL and an increase in estradiol from the follicle [79, 80, 82]. Dominant follicle estradiol production leads to pre-ovulatory surges in LH and FSH [79, 82]. The metestrus stage includes the formation of the CL and progesterone secretion after ovulation [82]. Metestrus uterine bleeding, associated with the increasing progesterone-to-estradiol ratio, occurs in 48-60% of cows [84]. During the diestrus period, the CL becomes fully-functional and secretes high levels of progesterone [79, 82]. Early structural and functional regression of the CL occurs during late diestrus stage in the absence of pregnancy [80]. Luteal regression and a corresponding decline in progesterone occur earlier (i.e., mid-luteal phase) in women compared to the bovine species (i.e., late-follicular phase) [45].

## 1.3 Ovarian Imaging Techniques

The development of medical imaging techniques has contributed immensely to the understanding of reproductive anatomy and physiology, and enhanced clinical diagnoses. This chapter focuses on early, conventional, and emerging methods of ovarian tissues imaging.

### 1.3.1 Histological Imaging

Histologic evaluation of the ovaries was first conducted in 1951, and is currently the most common method used to diagnose ovarian pathology *ex vivo* [85, 86]. Histological evaluation of ovarian tissues typically involves fixing the tissues of interest in formalin and embedding them in paraffin. Fresh tissues require fixation to preserve cell structures and prevent post-mortem changes such as putrefaction and autolysis [87, 88]. The classic fixative for most soft tissues, including ovaries, is 10% neutral buffered formalin, consisting of formaldehyde (primary fixative) and methanol (coagulative fixative) [26, 87, 89-91]. The purpose of fixation is to stabilize chemical bonds within the living cells prior to tissue processing [26]. Inadequate fixation can result in cellular changes within the tissues, including a disruption of the mitochondrial matrix and smooth endoplasmic reticulum [87]. Prolonged fixation using formaldehyde can also cause shrinkage of the tissues [92]. Following fixation, the tissues are sectioned at 3 to 4 mm in thickness and placed in embedding cassettes [26]. Tissue processing begins by dehydrating the tissue sections using alcohol [22, 26, 91]. The dehydrated tissues are then treated with a clearing agent, such as xylene, chloroform, or toluene [26, 88]. Infiltration is a process by which paraffin is infused into the tissue [22, 26, 88, 91]. The infiltrated tissues are then embedded into melted paraffin and allowed to solidify [22, 26, 88, 91]. Embedding creates solid paraffin blocks of the tissue samples for microsectioning [22, 26]. Microsectioning involves slicing the prepared tissue paraffin blocks into very thin sections using a microtome. Selected slices of the tissue sample are then placed on a warm water-bath prior to transferring them onto a microscope slide. The water-bath helps to smooth out wrinkles or folds in the sections [88]. The microscopic slides with the tissue sections are placed on a heating block overnight [26, 88].

Staining the prepared slides involve a series of steps, beginning with deparaffinization using xylene or toluene [26, 88]. The slides are then dipped in a series of alcohol solutions [26]. The sections are hydrated and then stained with hematoxylin and eosin. [26, 88]. The slides are rinsed in running water to remove excess stain and dipped into 1% hydrochloric acid in 70% ethanol until a brown color appears [26]. The slides are washed again in water, soaked in 0.5 % eosin, and then dipped through a series of alcohol baths [26]. The last steps of the staining process include washing the slides with xylene and mounting the coverslips. Staining is used to differentiate structural components of biological tissues. Hematoxylin is a base that stains the acidic portions of a cell (i.e., nucleus and ribosome-rich regions of the cytoplasm) with a bluish

color [88, 91]. Eosin is an acid that stains basic components of the tissues (i.e., cytoplasm) with a reddish tint [88, 91]. An example of a histological photograph of a bovine ovary is shown in Figure 1.2. One of the common problems in histology is over or under-staining, which can interfere with the microscopic analysis of the slides.

Histology is a useful technique for identifying structures within an organ, diagnosing lesions, and detecting parasites or regions of degenerations and regeneration [92]. The earliest histological ovarian evaluations were conducted in the 1950s [85, 86]. These studies involved the development of a classification system for ovarian follicles, comparison of growth and degeneration of follicles in the ovary, and variations in follicle growth in women of different ages [85, 86]. Histology can only be performed after surgical removal of the ovaries or post-mortem. Therefore, histology does not enable the real-time investigation of ovarian structures across the menstrual cycle. Histological techniques also do not allow the evaluation of fluid volume within a cavity (i.e., follicle), direction or amount of blood flow within the tissues, as well as cellular interactions [92]. Despite these limitations, histology has become the gold standard for pathological evaluations because of its ability to visualize tissues at the cellular level.

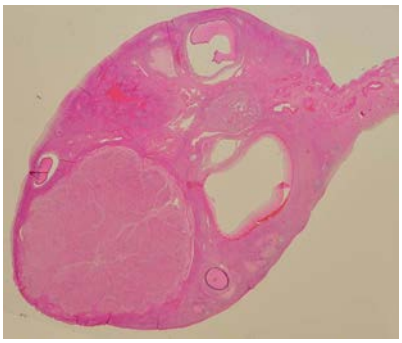

**Figure 1.2** A histological photograph of a bovine ovary sectioned at 10 µm and stained with hematoxylin and eosin. (Basnayaka, et al., 2013, unpublished)

### 1.3.2 Ultrasonographic Imaging

Ultrasonography was first used in 1914, during the First World War, as a method for detecting submarines. Ultrasonography was first introduced to the field of medicine during the late 1940s [93, 94]. Alfred Kratochwil was the first person to obtain a clear ultrasonographic image of the human ovary [93]. He demonstrated that morphological changes in the ovary including luteal development and regression, can be detected with ultrasonography [93]. Since

then, ultrasonographic imaging has become the most commonly-used tool for real-time examination of anatomical and physiological changes in the female pelvis [95]. Diagnostic ultrasonographic imaging systems are easily accessible, user-friendly, non-invasive, inexpensive, and portable [96, 97].

In ultrasonography, sound waves are created by vibrations of crystals [97]. The crystals are piezoelectric and can thereby produce mechanical sound waves from an electric current [98, 99]. Ultrasound is a sound wave with a frequency above the audible range of hearing (20 Hz – 20 kHz) [100]. Sound is a longitudinal wave, meaning that the vibrations oscillate back and forth along the direction of propagation of the wave [100]. The frequency range of sound waves for medical diagnostic imaging is 2-15 MHz [100]. Once the sound waves are transmitted into the tissues, they can be either reflected, scattered or refracted [98, 99]. Acoustic impedance describes the inherent characteristic of a certain medium to propagate sound waves [99, 100]. Reflection of sound waves occurs at large interfaces (i.e., between organs) when the difference in acoustic impedance is high. The sound wave is scattered when it encounters objects that are equal or smaller than the wavelength [100]. A low acoustic impedance difference between tissues borders indicates less reflection, more refraction, and more transmission of the sound waves [99]. In contrast, a high acoustic impedance between tissues leads to the loss in energy of the sound wave as it travels through tissue which is also known as attenuation [100, 101]. Attenuation is influenced mostly by absorption of energy into the tissues, as well as some scattering [101, 102]. Only the reflected and scattered sound waves will return back to the transducer. The returned ultrasound wave is converted into an electric signal and displayed on the imaging monitor [101]. Sound waves that are refracted can sometimes produce echoes that are detected in an ultrasonographic image. However, the refracted echo is displayed as originating from an undeviated axis and is misplaced from its original position in the ultrasonographic image [103].

#### 1.3.2.1 Generation of Ultrasonographic Images

The overall process of ultrasonographic imaging is shown in Figure 1.3. The mechanical signal of the returning sound wave is detected by a receiver. Upon receipt, the signal is amplified to compensate for attenuation [98]. The strength or amplitude of the returning signal at regular intervals in time is measured [98, 103]. A digital scan converter converts the mechanical echo

signal into a digital electrical signal which is stored as binary digits, or 'bits'[103]. Each bit is assigned a gray-scale value corresponding to the amplitude of the returning signal, which is displayed on the imaging monitor [103]. The echoes are stored in vertical scan lines and then read by the scan converter as horizontal or raster lines [103]. A picture element or 'pixel' is located at the intersection of a scan and raster line. After an ultrasound pulse is emitted, B-mode (Brightness mode) imaging displays the brightness of pixels, which corresponds to the amplitude of the signal [101, 104]. Each pixel represents one of the 256 shades of gray. The location of each pixel depends on the location of the stored digital signal in the scan converter, [103]. Digitized ultrasound signals are less prone to noise, and allow real-time scanning and stable post-processing of the images [103, 105]. Real-time B-mode imaging is the most commonly-used form of ultrasonographic imaging [97]. Fluids (i.e., follicular fluid) are considered non-reflective or 'anechoic' and appear black in the ultrasonographic image [98]. In contrast, highly dense structures, such as bone and calcifications, are reflective, and are displayed as white or 'hyperechoic' foci in the images [98]. Tissue structures that appear as darker shades of gray in the ultrasonographic image are considered hypoechoic.

Other types of ultrasonographic imaging include Amplitude (A)-mode, Motion (M)-mode, and Doppler. A-mode imaging displays the amplitude or the strength of the reflected signal with imaging depth [101]. A-mode imaging was one of the earliest types of ultrasonography, and is no longer used. M-mode imaging is currently used to evaluate structural movement with time (i.e., cardiac function) [101]. Doppler imaging is used to detect characteristics of blood flow, such as speed and direction [97, 101].

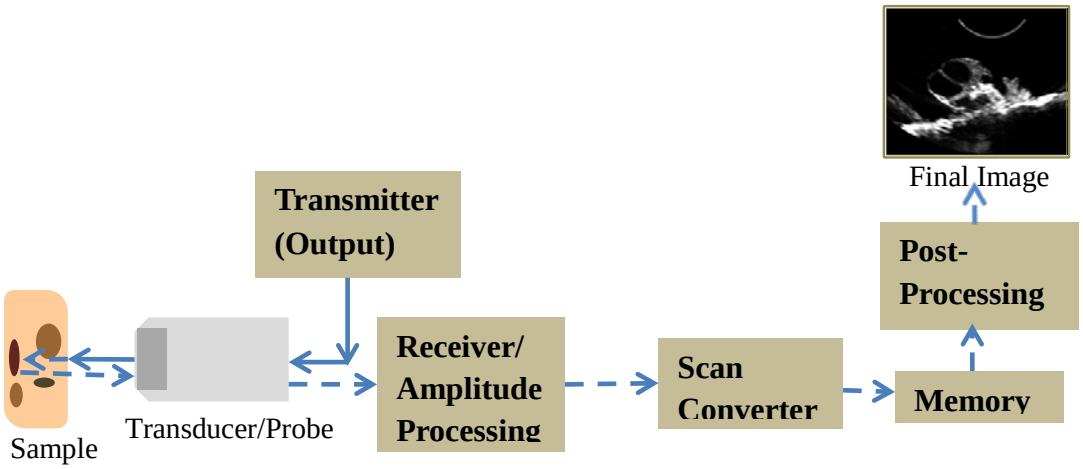


**Figure 1.3** Basic processes of conventional ultrasonographic imaging. (Basnayaka, et al., 2013, unpublished)

### 1.3.2.2 Ultrasonographic Imaging of the Ovaries

Ultrasonographic imaging of ovaries can be achieved transabdominally (3 – 5 MHz) or transvaginally (5 – 7.5 MHz) in women. Furthermore, transrectal ultrasonography is often conducted (7.5 – 10 MHz) in animals [106, 107]. Transabdominal scanning was the first type of imaging adopted for diagnostic purposes. Transabdominal imaging for evaluating the ovaries involves placing the transducer directly above the symphysis pubis [96, 107]. A full bladder can improve the visualization of the ovaries [107]. In contrast, transvaginal or transrectal approaches offer improved resolution of the ovaries because of the close proximity of the transducer to the target tissues [96]. Filling of the urinary bladder is not necessary for the transrectal or transvaginal methods [96]. Transvaginal ultrasonography is now the preferred imaging modality for evaluating the ovaries in women. The advent of transvaginal ultrasonography has substantially improved the ability to visualize normal and abnormal morphology of the ovary. It has been found that ultrasonographic image attributes of ovaries correspond to structural, functional and haemodynamic changes [45, 77].

### 1.3.2.3 Artifacts and Limitations of Ultrasonographic Imaging

The ability of ultrasonography to resolve structures within biological tissues (i.e., ovaries) is determined by axial, lateral, and elevation resolution. Axial resolution describes the ability to distinguish between two tissue reflectors that are along the beam axis while lateral resolution

describes the ability to resolve 2 reflectors positioned perpendicular to the beam axis [101, 102]. Axial resolution is based on the wavelength and the number of wave cycles emitted per transmitted pulse [108]. Therefore, the axial resolution can be improved by increasing the imaging frequency [102]. Lateral resolution is dependent on the width of the piezoelectric elements, and can be optimized by focusing the beam [109]. Elevation resolution is based on the ultrasound beam thickness perpendicular to the scan plane [110].

Ultrasonographic images are subject to artifacts, which are added, removed or misplaced echoes that decrease image quality [101, 110]. Artifacts are primarily caused by variations in the tissue structure and/or the mechanics of the transducer [101]. Understanding the mechanisms underlying common artifacts is essential for accurately interpreting ultrasonographic images. Reverberation artifacts are formed when a sound wave encounters two interfaces with a high mismatch in acoustic impedances [102]. Shadowing and reverberations are the most common artifacts that are visualized during imaging of the pelvis [96]. Reverberations are caused by the reflection of sound waves by strong reflecting interfaces, such as liquid-filled areas [110]. Reverberations can be identified as a series of parallel lines of decreasing brightness in the ultrasonographic image [96, 101, 110]. Shadowing is created by structures that have strong attenuation, such as bowel, which creates a dark shadow posterior to the structure [96, 99, 102, 110]. Enhancement artifacts are created when the transmitted wave encounters structures with poor attenuation, such as fluid-filled structures in the ovary [96, 110]. Enhancement produces a bright signal in the image area that is distal to the fluid-filled structure [44, 96, 110].

Ultrasonography has most certainly increased our understanding of ovarian structure and function over the past 30 years. However, it is worthwhile to recognize that the resolution of standard routine ultrasonography limits the visualization of ovarian structures < 2mm in diameter such as early antral follicles and COC. Another limitation associated with ultrasonography is the difficulty in visualizing tissues that lie deep within the body, a particular concern in women with a large body habitus [96, 111]. Furthermore, the presence of air-filled bowel can impede sound wave transmission and interfere with image quality [96]. Ultrasonography does not emit radiation, but some of the ultrasound energy can be lost as heat into the tissues [112]. Furthermore, ultrasound waves transmitted at high frequencies for long periods of time can cause the generation of gas bubbles within the body (i.e., cavitation), which may cause health concerns.

Appropriate actions must be taken by the ultrasonographer to minimize patient risk by optimizing and maintaining equipment according to the current safety standards [112].

### 1.3.3 Synchrotron Imaging

Radiation-based medical imaging was first used in 1895, after the discovery of X-rays by Wilhelm Röntgen (Germany) [113, 114]. X-rays are electromagnetic, transverse, waves containing photons which range in energy from 0.1 to 150 keV [115, 116]. The corresponding X-ray wavelength is about 0.01 to 10 nm [116, 117]. Synchrotron imaging is a novel X-ray technique in which a high-energy light beam is generated. Synchrotron-based visible radiation was first created in 1947 by General Electric [118]. Since then, more than 70 synchrotron facilities have been established worldwide and numerous studies have been conducted to optimize synchrotron methods for biomedical imaging.

In a synchrotron, electrons are injected into a vacuum-sealed tube and are accelerated to reach very high speeds and energy states [119]. The accelerated electrons are stored in a centrally-located, closed-loop tube, known as the storage ring [120]. A series of 'bending' magnets are placed along the storage ring to maneuver the beam in a circular direction [119, 120]. In the storage ring, the electrons will emit electromagnetic radiation (i.e., synchrotron radiation or light) when their trajectories are bent by a magnetic field [119, 120]. The production of synchrotron light is governed by inverse Compton scattering [119]. During inverse Compton scattering, an electron collides with an incoming photon and loses energy while emitting another photon of higher energy [119]. In the synchrotron, the storage ring consists of a static magnetic field which acts as an incoming virtual photon with which the electrons collide and generate synchrotron light [119]. The light that is emitted can be directed along tangential straight tubes or beamlines, which can then be used for conducting experiments with various applications [120]. An important characteristic of a synchrotron is that the electrons circulate around the storage ring in discrete bunches [120]. Therefore, synchrotron light is emitted as a pulse rather than a continuous form. The synchrotron consists of a radiofrequency cavity which accelerates the electric field to compensate for the loss of energy in the electron beam as waves are emitted [119]. Insertion devices can be placed along the electron pathway to optimize radiation characteristics, such as energy and bandwidth [119].

X-rays that enter an object can lose energy or become attenuated through photoelectric absorption and Compton scattering (i.e., inelastic scattering). Photoelectric Absorption is the absorption of the incident X-ray by tissue, which results in a loss in beam energy as it travels through an object [121]. Compton scattering arises when the X-rays encounter small objects within the tissues that redirect the photons from the original direction of the beam [121, 122]. The redirected photon will contain a lower energy than the incoming photon [116]. Both photoelectric absorption and Compton scattering primarily exist in the X-ray medical imaging range of 20 to 150 keV [121, 123].

Other X-ray interactions that play an important role in medical imaging include refraction, coherent scattering (i.e., elastic scattering), and diffraction. Refraction is the transverse shift of the beam direction as the X-rays propagate through media [124]. Coherent scattering is similar to Compton scattering but results only in a change in direction of the scattered photon and therefore does not contribute to attenuation [123]. Diffraction occurs due to the interference of coherently scattered X-rays by a solid object, such as a crystal [113].

In conventional radiology, only the X-ray absorption in the object is used for biomedical imaging [125, 126]. Conventional X-rays will therefore have to be powerful enough to provide enough signal to be absorbed to visualize objects, but also maintain low radiation exposure to the tissues [120]. Alternatively, the synchrotron offers the possibility of imaging biological tissues with various techniques that do not rely only on absorption of X-ray characteristics, which translates to lower radiation exposure to the patient.

Advantages of using synchrotron radiation for biomedical imaging include the availability of an X-ray beam that is polarized, collimated, high intensity and tunable over a wide energy spectrum ranging from infrared to hard x-rays [120, 127]. One of the biggest limitations of conventional radiographic imaging of biological tissues is radiation damage to the tissues. Irradiation of biological tissues may disrupt cell division and induce cell death [116]. Radiation doses less than 50 mSv is considered to be safe and do not cause any observable physiological damage to tissues [128]. A crystal monochromator is used at the synchrotron to select a specific wavelength of energy which allows samples to be imaged with less radiation exposure compared to conventional radiography [113].

Synchrotron imaging has been used to examine physical (i.e., density, morphology) and chemical (i.e., state and structure) properties of biological tissues [129]. The synchrotron has

been adapted as a tool to examine feeding patterns in beetles and butterflies [128], lung function in mice and rabbits [124, 130, 131] as well as respiratory function in grasshoppers [132]. Researchers have also examined synchrotron radiation angiography in rabbits [133], mice [134], dogs [135], pigs [136] and humans [137]. Synchrotron technologies have provided improved resolution for differentiating normal and abnormal breast tissue, compared to conventional mammography [138-141]. The synchrotron can be used to image renal and prostate tissue [142]. Synchrotron technologies also show promise as a source of radiotherapy for patients [143]. The high collimation of synchrotron X-rays can improve tissue targetability and decrease radiation exposure to patients [143].

A few reproductive imaging studies have been conducted using the synchrotron. A proof-of-principle study was conducted by members of our research group in 2002 to examine the usefulness of early synchrotron techniques for imaging bovine ovaries [144]. Synchrotron-based high resolution X-ray computed microtomography has also been used to image genital morphology of caecilian amphibians [145] and reproductive organs of mites [146]. In addition, synchrotron imaging has been used to examine the molecular architecture and elemental composition of mice oocytes *in vitro* [147, 148] as well as mammalian oocyte coat assembly and oocyte-sperm interactions [149].

#### 1.3.3.1 Phase-Contrast Based Imaging Techniques

Phase-contrast based synchrotron techniques are emerging as novel approaches to biomedical imaging. Contrast is the difference in brightness between image pixels [116]. The contrast in the images obtained using phase-contrast techniques is derived from the refraction and absorption properties of tissues, such as tissue thickness and density [113, 123-125, 138, 150]. There are three main phase-contrast imaging techniques:

(1) *Analyzer-based or Diffraction Enhanced Imaging (DEI);*

(2) *Propagation-Based Imaging (PBI)*; and

(3) *Talbot Grating Interferometry (TGI).*

The main setup of the beamline for the three different phase contrast-based techniques compared to absorption imaging (i.e., conventional radiography) is shown in Figure 1.4. Beamline components include a monochromator, sample stage, and a detector (Fig.1.4 A - D). The monochromator consist of two crystals, which allow the selection of a very narrow band of

wavelengths [119, 120]. The main purpose of the detector is to convert the detected photons into an electronic signal that is suitable for digitalization [120]. However, the mechanism by which the conversion occurs can vary according to the type of detector. Two common types of detectors are ionization chambers and CCD (i.e., charged coupled device) detectors. The current signals in the ionization chambers are directly created by the interaction of gas molecules with incoming photons [120]. Charged coupled devices will generate electrical charge through the sequential movement of photons through a series of bins [120]. The resulting electrical signal will be converted into a digital bit stream by an analog-to-digital converter [116].

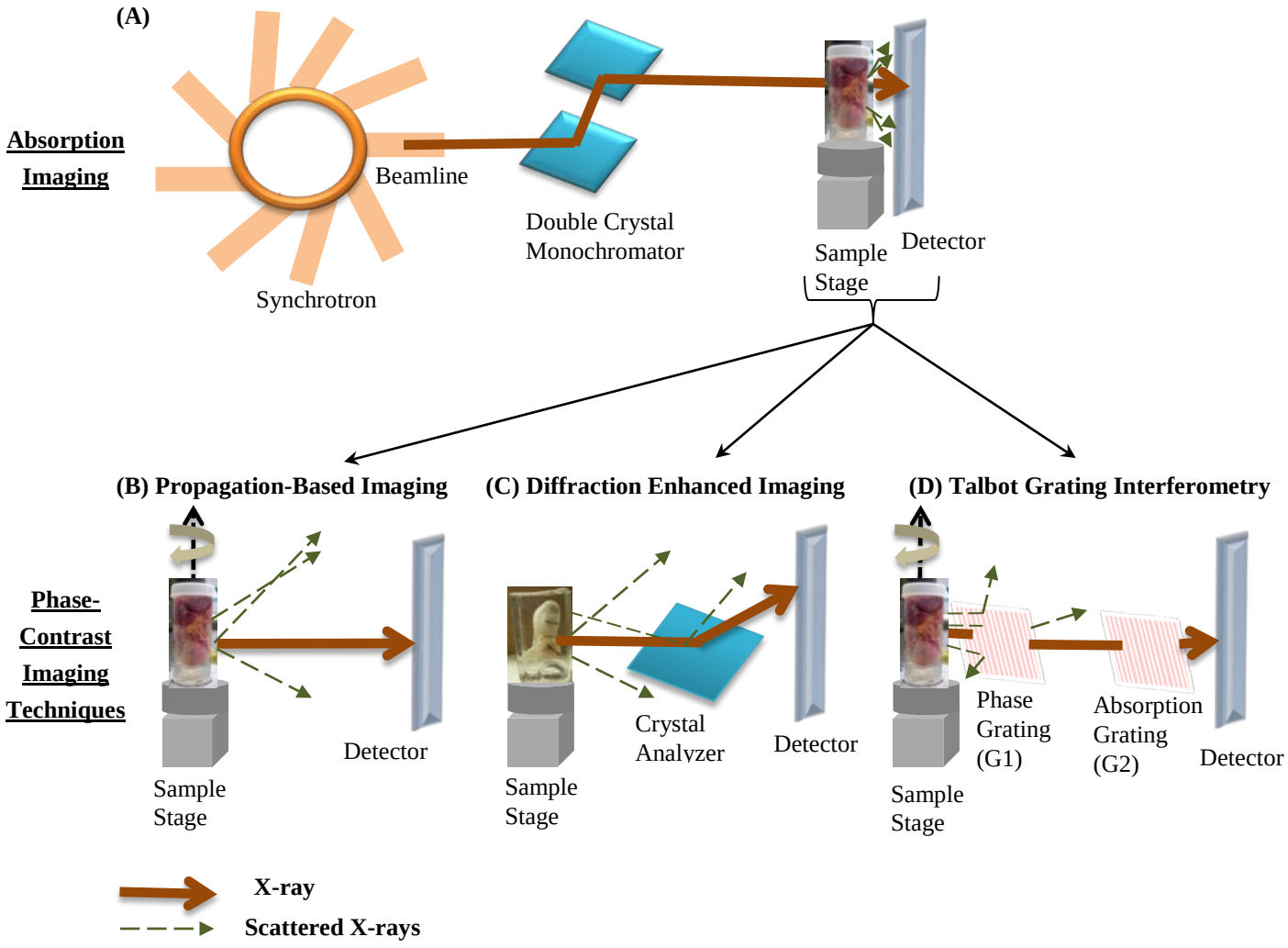


**Figure 1.4** Synchrotron beamline setup for absorption imaging (A) and phase-contrast techniques, including Propagation-Based Imaging (B), Diffraction Enhanced Imaging (C), and Talbot Grating Interferometry (D). The direction of the synchrotron light beam and the scattering of the X-rays are also indicated. (Basnayaka, et al., 2013, unpublished)

#### 1.3.3.1.1 Diffraction Enhanced Imaging (DEI)

DEI involves the placement of a crystal, referred to as an analyzer, between the sample and detector (Figure 1.4C) [151]. The analyzer is rotated at various positions on a curve (known as the 'rocking curve') which allows the investigator to measure relative energy intensity as a function of the angular position of the crystal [152, 153]. Only X-rays that are selectively accepted by the crystal will be diffracted and detected in the final image [152]. Images obtained with DEI contain contrast information based on the absorption, refraction and scatter rejection of X-rays [152]. The crystal acts as an anti-scatter device as it removes most of the X-rays that are scattered from the sample [123]. 'Apparent absorption' images contain contrast based on absorption and scattering of X-rays [141, 154]. The crystal analyzer is placed at the top of the rocking curve to obtain an absorption image that is nearly free from scatter [154]. Refraction images obtained with DEI will only contain refracted contrast from the sample [152]. DEI has been useful for detecting boundaries and edges of samples, as well as changes in the refractive indices between materials [152]. Studies have been conducted to examine DEI as a tool for evaluating human samples, including bone and soft tissues of the foot and ankle [155], breast tissues [141, 156, 157], articular cartilage in knees [158], and uterine leiomyomas [154]. DEI is not highly reliant on imaging energy and therefore, allows samples to be imaged with less radiation exposure compared to conventional methods [152, 159]. It was found that the surface radiation dose of breast tissue specimens imaged with DEI at 60 keV was substantially lower (0.1 mGy) than conventional mammography at 30 keV (25.6 mGy) [157].

#### 1.3.3.1.2 Propagation-Based Imaging (PBI)

In PBI, the detector is placed further away from the sample compared to conventional radiography (Figure 1. 4A, B). The placement of the detector close to the sample, as in conventional radiography, enables the detection of only absorption contrast [160, 161]. Increasing the sample-detector distance will allow the transmitted X-rays from the sample to propagate further and produce phase distortions due to the interference of refracted and unrefracted X-rays [138, 150, 162, 163]. Increasing the gap between sample and detector also prevents scatter from reaching the detector whereas conventional radiographic images always contain scatter [123, 141]. In propagation based images, strong interference patterns are observed when there is a large difference between the refractive indices of two materials. The interference

pattern is also known as the ‘edge-enhancement effect’ because it creates dark and bright fringes at sample boundaries (i.e., between fluid and soft tissue) and improves the overall image quality [126, 138, 163]. The edge-enhancement feature of PBI has been shown to improve the identification of breast tumors [139, 140].

#### 1.3.3.1.3 Talbot Grating Interferometry (TGI)

The beamline setup for TGI imaging includes two identical crystals known as ‘gratings’:1) phase grating, and 2) absorption grating (Figure 1.4D) [164, 165]. The phase grating (G1) is placed behind the object to allow the interference of diffracted x-rays. The absorbing analyzer grating (G2) is placed between the first grating and the detector to transform the interference fringes into an intensity signal [166]. Without G2, it would be difficult to resolve the closely-spaced interference fringes created by G1 [166]. Both refraction and absorption contrast can be measured using the grating-based technique [167]. Grating-based imaging is more difficult to implement than the other types of phase contrast imaging, because it requires careful alignment of the crystals [126]. Grating-based synchrotron techniques have been used to image rat kidney tissues [168] and heart ventricle muscles [166].

Propagation- and analyzer-based synchrotron imaging methods are more effective for detecting large variations in the refractive index of tissue structures [168]. The grating-based technique is more powerful for detecting subtle refractions of the X-ray beam caused by small variations in refractive index of tissues (i.e., weakly absorbing objectives, such as soft tissues) [164]. Phase contrast synchrotron imaging can be further optimized by incorporating computed tomography (CT) techniques. During CT, the object is rotated while the X-ray beam transversely crosses the object of interest [169]. Three dimensional (3D) visualization and characterization of biological tissue samples are possible with synchrotron CT imaging [170].

### 1.3.3.2 Synchrotron Image Resolution and Common Artifacts

Synchrotron image quality can be quantitatively determined by the signal-to-noise ratio (SNR), contrast-to-noise ratio (CNR), and spatial resolution [171]. Noise refers to any unwanted information that is detected along with the x-ray signal. The SNR is defined by the ratio of the signal to the standard deviation of the noise. The measurement of contrast in relation to noise will provide a better calculation of how well structures are differentiated from one another [116].

Factors that influence the SNR and CNR include the X-ray energy, imaging time, sample size and thickness, and the efficiency of the detector [122]. Spatial resolution is the smallest distance at which two individual features can be resolved [171]. Features of the detector and the distances from the source (i.e., source-to-object, source-to-detector) contribute to the spatial resolution of the image [122].

Two artifacts that are commonly observed in synchrotron images are beam hardening and ring artifacts. Beam hardening is most common when an X-ray beam with a range of wavelengths (i.e., polychromatic beam) is used to image a sample [170]. As the polychromatic beam traverses an object, the low-energy X-rays are absorbed faster into the tissues than the high-energy X-rays [123, 170]. Therefore, the average energy of the outgoing beam is higher than the incident beam. The beam hardening effects cause an artificial darkening in the center and brightening in the edges of the images [170]. Ring artifacts are generated from imperfect detector elements [172]. These shifts can be produced by scanning conditions, such as temperature and beam strength [170]. Filtering and calibrating the X-ray beam before it passes through the object are possible solutions to synchrotron image artifacts [170].

## 1.4 References


1. **Soranus o. E.** Soranus' gynecology. O. Temkin, trans. Baltimore: Johns Hopkins University Press; 1991:258.
2. **Hunter R. H. F.** Mammalian ovaries, Graafian follicles and oocytes: selected historical landmarks. *Physiology of the Graafian Follicle and Ovulation*. 2003 ed. Cambridge: Cambridge University Press; 2003:379.
3. **Speroff L. F., M**. The ovary - Embryology and development. *Clinical Gynecologic Endocrinology and Infertility*. Vol 7ed. Philadelphia: Lippincott Williams & Wilkins; 2005:97-99.
4. **Netter F. H.** Atlas of human anatomy. Summit: Ciba-Geigy Corporation; 1989.
5. **Adams G. P. and Pierson R. A.** Bovine model for study of ovarian follicular dynamics in humans. Theriogenology. 1995; 43(1): 113-120.
6. **Gougeon A.** Dynamics of human follicle growth: Morphologic, fynamic, and functional aspects. In: E. Y. A. Peter C.K. Leung, ed. *The Ovary*. 2 ed. California: Elsevier Academic Press; 2004:25-38.
7. **Junqueira L. C. U.** The female reproductive system. In: A. L. Mescher, ed. *Junqueira's basic histology : text and atlas* 12th ed. New York: McGraw-Hill Medical; 2010.
8. **Strauss J. F. and Williams C. J.** The ovarian life cycle. *Yen & Jaffe's Reproductive Endocrinology (6th Edition)*. Philadelphia: W.B. Saunders; 2009:155-190.
9. **Mossman H. W. and Duke K. L.** Comparative morphology of the mammalian ovary. Madison: The University of Wisconsin Press; 1973:461.
10. **Reynolds S. R. M.** The vascularity of the ovary and ovarian function. Recent Prog. Horm. Res. 1950; 565 - 100.
11. **Peters H. and McNatty K.** Morphology of the ovary. *The ovary - A correlation of structure and function in mammals*. Great Britain: Paul Elek Ltd.; 1980:12-18.
12. **Acosta T. J. and Miyamoto A.** Vascular control of ovarian function: ovulation, corpus luteum formation and regression. Animal Reproduction Science. 2004; 82-83127-140.
13. **Basset D.** The changes in the vascular pattern of the ovary of the albino rat during the oestrous cycle. Am. J. Anat. 1943; 73251 - 291.
14. **Eli G. and Jaffe R.** Ovarian angiogenesis. In: E. Y. A. Peter and C. K. Leung, eds. *The Ovary*. 2 ed. California: Elsevier Academic Press; 2004:305 - 317.
15. **Mitchell G. A.** The innervation of the ovary, uterine tube, testis and epididymis. J Anat. 1938; 72(Pt 4): 508-517.
16. **Mohsin S. and Pennefather J. N.** The sympathetic innervation of the mammalian ovary. A review of pharmacological and histological studies. Clin Exp Pharmacol Physiol. 1979; 6(3): 335-354.
17. **Neilson D., Seegar J., Donald W. and Benjamin G.** The innervation of the ovary. Obstet Gynecol Surv. 1970; 25889 - 904.
18. **Owman C., Rosenbren E. and Sjoberg N. O.** Adrenergic innervation of the human female reproductive organs: a histochemical and chemical investigation. Obstet Gynecol. 1967; 30(6): 763-773.
19. **Morris B. and Sass M.** The formation of lymph in the ovary. Proc. Roy. Soc. B. 1966; 164577 - 591.
20. **Kezele P. and Skinner M.** Regulation of ovarian primordial follicle assembly and development by estrogen and progesterone: endocrine model of follicle assembly. Endocrinology. 2003; 144(8): 3329-3337.

21. **Crisp T.** Organization of the ovarian follicle and events in its biology: oogenesis, ovulation or atresia. Mutation Research/Reviews in Genetic Toxicology. 1992; 296(1-2): 89 - 106.
22. **Gartner L. P., Hiatt, J. L.** Color textbook of histology. Third ed. Philadelphia: Elsevier Inc. ; 2007:573.
23. **Kacinskis M. A., Lucci C. M., Luque M. C. and Bao S. N.** Morphometric and ultrastructural characterization of Bos indicus preantral follicles. Anim Reprod Sci. 2005; 87(1-2): 45-57.
24. **Gougeon A.** Human ovarian follicular development: From activation of resting follicles to preovulatory maturation. Ann Endocrinol (Paris). 2010; 71(3): 132-143.
25. **Cui D.** Atlas of histology: with functional and clinical correlations. First ed. Philadelphia: Lippincott Williams & Wilkins; 2011:439.
26. **McManus J. and Mowry R.** Staining mehods - histologic and histochemical. New York: Hoeber Medical Division, Harper & Row Publishers; 1965: 8-57
27. **Ross MH, Pawlina W and TA B.** Female reproductive system. *Atlas of Descriptive Histology*. Massachusetts: Sinauer Associates; 2009:304-312.
28. **Rodgers R. J., Irving-Rodgers H. F. and van Wezel I. L.** Extracellular matrix in ovarian follicles. Mol Cell Endocrinol. 2000; 163(1–2): 73-79.
29. **Binelli M. and Murphy B. D.** Coordinated regulation of follicle development by germ and somatic cells. Reprod Fertil Dev. 2010; 22(1): 1-12.
30. **McGee E. A. and Hsueh A. J.** Initial and cyclic recruitment of ovarian follicles. Endocr Rev. 2000; 21(2): 200-214.
31. **Eppig J. J.** Oocyte control of ovarian follicular development and function in mammals. Reproduction. 2001; 122(6): 829-838.
32. **Baerwald A. R., Adams G. P. and Pierson R. A.** A new model for ovarian follicular development during the human menstrual cycle. Fertil Steril. 2003; 80(1): 116-122.
33. **Park S., Goldsmith L. and Weiss G.** Age-related changes in the regulation of luteinizing hormone secretion by estrogen in women. Experimental Biology and Medicine. 2002; 227455 - 464.
34. **Weiss G. and Goldsmith L.** Puberty and pediatric and adolescent gynecology. In: J. Scott, P. DiSaia, C. Hammond and W. Spellacy, eds. *Danforth's Obstetrics and Gynecology*. 7 ed. Philadelphia: JP Lippincott Co.; 1994:611 - 619.
35. **Mihm M., Gangooly S. and Muttukrishna S.** The normal menstrual cycle in women. Anim Reprod Sci. 2011; 124(3-4): 229-236.
36. **Harlow S., Windham G. and Paramsothy P.** Menstruation and menstrual disorders: the epidemiology of menstruation and menstrual dysfunction. In: M. Goldman, R. Troisi and K. Rexrode, eds. *Women and Health*. San Diego, CA: Academic Press; 2000:99 - 113.
37. **Adams G. P., Singh J. and Baerwald A. R.** Large animal models for the study of ovarian follicular dynamics in women. Theriogenology. 2012; 78(8): 1733-1748.
38. **Baerwald A.** Human antral folliculogenesis: what we have learned from the bovine and equine models. Anim. Reprod. 2009; 6(1): 20-29.
39. **Baerwald A. R., Adams G. P. and Pierson R. A.** Ovarian antral folliculogenesis during the human menstrual cycle: a review. Hum Reprod Update. 2012; 18(1): 73-91.
40. **Ginther O. J., Gastal E. L., Gastal M. O., Bergfelt D. R., Baerwald A. R. and Pierson R. A.** Comparative study of the dynamics of follicular waves in mares and women. Biol Reprod. 2004; 71(4): 1195-1201.

41. **Smith M.** Estrus and menstrual cycles: neuroendocrine control. In: L. Squire, ed: Academic Press; 2009:1-5.
42. **O.J. G., Beg M. A., Bergfelt D. R., Donadeu F. X. and Kot K.** Follicle selection in monovular species. Biol Reprod. 2001; 65638-647.
43. **Hess A., Nayak N. and Giudice L.** Oviduct and endometrium: cyclic changes in the primate oviduct and endometrium. In: J. Neill, ed. *Physiology of Reproduction*. 3 ed. St. Louis, MO: Elsevier Academic Press; 2006:337-382.
44. **Bomsel-Helmreich O.** Ultrasound and the preovulatory human follicle. Oxf Rev Reprod Biol. 1985; 71-22.
45. **Baerwald A. R., Adams G. P. and Pierson R. A.** Form and function of the corpus luteum during the human menstrual cycle. Ultrasound Obstet Gynecol. 2005; 25(5): 498-507.
46. **Espey L. and Richards J.** Ovulation. In: J. Neill, ed. *Knobil and Neill's Physiology of Reproduction.* Vol 1. St. Louis, MO: Elsevier Academic Press; 2006:425-474.
47. **Pierson R. A., Martinuk S. D., Chizen D. R. and Simpson C. W.** Ultrasonographic visualization of human ovulation. In: J. Evers and M. Heineman, eds. *From Ovulation to Implantation: Proceedings of the 7th Reinier de Graaf Symposium*. Amsterdam: Elsevier Science Publishers (Biomedical Division); 1990:73-79.
48. **Croxatto H. B.** Female reproductive physiology/function. In: H. Kris, ed. *International Encyclopedia of Public Health*. Oxford: Academic Press; 2008:603-613.
49. **Pierson R. A. and Chizen D. R.** Transvaginal diagnostic ultrasonography in evaluation and management of infertility. Journal SOGC. 1991; 37 - 49.
50. **Devoto L., Fuentes A., Kohen P., Céspedes P., Palomino A., Pommer R., Muñoz A. and Strauss Iii J. F.** The human corpus luteum: life cycle and function in natural cycles. Fertility and Sterility. 2009; 92(3): 1067-1079.
51. **Eppig J.** Oocyte control of ovarian follicular development and function in mammals. Reproduction. 2001; 122829 - 838.
52. **Augustin H. G.** Vascular morphogenesis in the ovary. Baillière's Best Practice and Research in Clinical Obstetrics and Gynaecology. 2000; 14(6): 867-882.
53. **Fields MJ and PA F.** Morphological characteristics of the bovine corpus luteum during the estrous cycle and pregnancy. Theriogenology. 1996; 45(7): 1295-1325.
54. **Baerwald AR A. G., Pierson RA.** Form and function of the corpus luteum during the human menstrual cycle. Ultrasound Obstet Gynecol. 2005; 25(5): 498 -507.
55. **Miyazaki T., Tanaka M., Miyakoshi K., Minegishi K., Kasai K. and Yoshimura Y.** Power and colour Doppler ultrasonography for the evaluation of the vasculature of the human corpus luteum. Hum Reprod. 1998; 13(1O): 2836-2841.
56. **Backstrom T., Nakata M. and Pierson R. A.** Ultrasonography of normal and aberrrant luteogenesis. In: R. Jaffe, R. Pierson and J. Abramowicz, eds. *Imaging in infertility and reproductive endocrinology*. Philadelphia: J.B. Lippincott Company; 1994:143-154.
57. **Gougeon A.** Dynamics for human follicular growth: Morphologic, dynamic, and functional aspects. In: P. Leung and E. Adashi, eds. *The Ovary*. 2nd ed. San Diego, California: Elseiver Academic Press; 2004:25 - 38.
58. **Macklon N. S. and Fauser B. C. J. M.** Follicle-stimulating hormone and advanced follicle development in the human. Archives of Medical Research. 2001; 32(6): 595-600.

59. **Chang M.D M.-Y., Chiang M.D C.-H., Hsieh M.D T. s.-T. a., Soong M.D Y.-K. and Hsu Ph.D K.-H.** Use of the antral follicle count to predict the outcome of assisted reproductive technologies. Fertility and Sterility. 1998; 69(3): 505-510.
60. **Rodgers R. J., Irving-Rodgers H. F., van Wezel I. L., Krupa M. and Lavranos T. C.** Dynamics of the membrana granulosa during expansion of the ovarian follicular antrum. Molecular and Cellular Endocrinology. 2001; 171(1–2): 41-48.
61. **Fauser B. C.** Follicle pool depletion: factors involved and implications. Fertil Steril. 2000; 74(4): 629-630.
62. **Alonso-Pozos I., Rosales-Torres A. M., Avalos-Rodriguez A., Vergara-Onofre M. and Rosado-Garcia A.** Mechanism of granulosa cell death during follicular atresia depends on follicular size. Theriogenology. 2003; 60(6): 1071-1081.
63. **Gutierrez C. G., Glazyrin A. L., Robertson G. W., Campbell B. K., Gong J. G., Bramley T. A. and Webb R.** Ultra-structural characteristics of bovine granulosa cells associated with maintenance of oestradiol production in vitro. Mol Cell Endocrinol. 1997; 134(1): 51-58.
64. **Krause W. and Cutts J.** The female reproduction sSystem. *Concise Text of Histology*. Baltimore: Williams & Wilkins; 1981:367-371.
65. **Westhoff C., Murphy P. and Heller D.** Predictors of ovarian follicle number. Fertil Steril. 2000; 74(4): 624-628.
66. **Ruess M. L., Kline J., Santos R., Levin B. and Timor-Tritsch I.** Age and the ovarian follicle pool assessed with transvaginal ultrasonography. Am J Obstet Gynecol. 1996; 174(2): 624-627.
67. **Baker T.** A quantitative and cytological study of germ cells in human ovaries. Proc R Soc Biol. 1963; 158417 - 433.
68. **Hsu A., Arny M., Knee A., Bell C., Cook E., AL N. and DR G.** Antral follicle count in clinical practice: analyzing clinical relevance. Fertility and Sterility. 2010; 95(2): 474 - 479.
69. **Bancsi L., Broekmans F., Eijkemans M., DeJong F., Habbema J. and TeVelde E.** Predictors of poor ovarian response in in-vitro fertilization: a prospective study comparing basal markers of ovarian reserve. Fertil Steril. 2002; 77328 - 336.
70. **Gibreel A., Maheshwari A., Bhattacharya S. and Johnson N.** Ultrasound tests of ovarian reserve; a systematic review of accuracy in predicting fertility outcomes. Hum Fertil (Camb). 2009; 1295 - 106.
71. **Ng E., Tang O. and Ho P.** The significance of the number of antral follicles prior to stimulation in predicting ovarian responses in an IVF programme. Hum Reprod. 2000; 151937 -1942.
72. **Vanden Brink H., Chizen D., Hale G. and Baerwald A. R.** Age-related changes in major ovarian follicular wave dynamics during the human menstrual cycle. Menopause. 2013.
73. **Bigelow B.** Comparison of ovarian and endometrial morphology spanning the menopause. Obstet Gynecol 1958; 11(5): 487 - 513.
74. **Tatone C. and Amicarelli F.** The aging ovary-the poor granulosa cells. Fertil Steril. 2013; 99(1): 12-17.
75. **Paszkowski T., Clarke R. and Hornstein M.** Smoking induces oxidative stress inside the Graafian follicle. Human Reproduction. 2002; 17(4): 921 - 925.

76. **Malhi P. S., Adams G. P. and Singh J.** Bovine model for the study of reproductive aging in women: follicular, luteal, and endocrine characteristics. Biol Reprod. 2005; 73(1): 45-53.
77. **Singh J., Pierson R. A. and Adams G. P.** Ultrasound image attributes of the bovine corpus luteum: structural and functional correlates. J Reprod Fertil. 1997; 109(1): 35-44.
78. **Pierson R. A. and Adams G. P.** Computer-assisted image analysis, diagnostic ultrasonography and ovulation induction: Strange bedfellows. Theriogenology. 1995; 43(1): 105-112.
79. **Forde N., Beltman M. E., Lonergan P., Diskin M., Roche J. F. and Crowe M. A.** Oestrous cycles in Bos taurus cattle. Anim Reprod Sci. 2011; 124(3–4): 163-169.
80. **Peter A. T., Levine H., Drost M. and Bergfelt D. R.** Compilation of classical and contemporary terminology used to describe morphological aspects of ovarian dynamics in cattle. Theriogenology. 2009; 71(9): 1343-1357.
81. **Sartori R. and Barros C. M.** Reproductive cycles in Bos indicus cattle. Animal Reproduction Science. 2011; 124(3–4): 244-250.
82. **Senger P.** Pathways to pregnancy and parturition. Pullman, WA: Current Conceptions, Inc.; 2003.
83. **Gangestad S. W. and Thornhill R.** Human oestrus. Proc Biol Sci. 2008; 275(1638): 991-1000.
84. **Hansel W. and Asdell S.** The causes of bovine metestrous bleeding. J ANIM SCI. 1952; 11346-354.
85. **Block E.** Quantitaive morphological investigations of the follicular system in women; methods of quantitative determinations. Acta Anatomica. 1951; 12(3): 267 - 285.
86. **Block E.** Quantitaive morphological investigatiosn of the follicular system in women; variations int he different phases of the sexual cycle. Acta endocrinol 1951; 333 - 54.
87. **Crang RFE and KL K.** Artefacts in biological electron microscopy. New York: Plenium Press; 1988.
88. **Luna L. G.** Manual of histologic staining methods of the armed forces institute of pathology. Third ed. New York: McGraw-Hill Book Company; 1968:258.
89. **Buesa R.** Histology without formalin? Annals of Diagnostic Pathology. 2008; 12.
90. **Burns W. and Bretschneider A.** Thin is in: Plastic embedding of tissues for light microscopy. Chicago: American Society of Clinical Pathologists; 1981.
91. **Junqueira L.** The female reproductive system. In: A. Mescher, ed. *Junqueira's basic histology: text and atlas*. 12 ed. New York: McGraw-Hill MEdical; 2010:1-15.
92. **Hillman H.** Limitations of clinical and biological histology. Medical Hypotheses. 2000; 54(4): 553-564.
93. **Levi S.** The history of ultrasound in gynecology 1950-1980. Ultrasound Med Biol. 1997; 23(4): 481-552.
94. **McNay M. B. and Fleming J. E.** Forty years of obstetric ultrasound 1957-1997: from A-scope to three dimensions. Ultrasound Med Biol. 1999; 25(1): 3-56.
95. **Hildebrandt T., Hermes R., Jewgenow K. and Goritz F.** Ultrasonography as an important tool for the development and application of reproductive technologies in non-domestic species. Theriogenology. 2000; 5373-84.
96. **Hearn-Stebbins B., Jaffe R. and Brown H.** Ultrasonographic evaluation of normal pelvic anatomy. In: R. Jaffe, R. Pierson and J. Abramowicz, eds. *Imaging in Infertility and Reproductive Endocrinology*. Philadelphia: J. B. Lippincott Company; 1994:1-21.

97. **Medan M. S. and Abd El-Aty A. M.** Advances in ultrasonography and its applications in domestic ruminants and other farm animals reproduction. Journal of Advanced Research. 2010; 1(2): 123-128.
98. **Pierson R. A., Kastelic J. P. and Ginther O. J.** Basic principles and techniques for transrectal ultrasonography in cattle and horses. Theriogenology. 1988; 29(1): 3-20.
99. **Herbener T. E.** Ultrasound physics: principles of ultrasonography. Gastrointestinal Endoscopy. 1996; 43(2, Part 2): S4-S5.
100. **Martin K. and Ramnarine K.** Physics. In: P. Hoskins, K. Martin and A. Thrush, eds. *Diagnostic Ultrasound; Physics and Equipment*. 2 ed. Cambridge: Cambridge University Press; 2010:4-22.
101. **Case T. D.** Ultrasound physics and instrumentation. Surgical Clinics of North America. 1998; 78(2): 197-217.
102. **Coltrera M. D.** Ultrasound physics in a nutshell. Otolaryngologic Clinics of North America. 2010; 43(6): 1149-1159.
103. **Martin K.** B-mode instrumentation. In: P. Hoskins, K. Martin and A. Thrush, eds. *Diagnostic Ultrasound: Physics and Equipment*. Cambridge: Cambridge University Press; 2010:47 - 63.
104. **Martin K.** Introduction to B-mode imaging. In: P. Hoskins, K. Martin and A. Thrush, eds. *Diagnostic Ultrasound: Physics and Equipment*. 2nd ed. Cambridge: Cambridge University Press; 2010:1-22.
105. **Srivastava A. K.** Basic Ultrasound instrumentation. In: S. K. Bhargava, ed. *Principles and Practice of Ultrasonography*. Pangbourne, UK: Alpha Science International Ltd.; 2003:27-40.
106. **Gonzalez-Bulnes A., Pallares P. and Vazquez M. I.** Ultrasonographic imaging in small ruminant reproduction. Reprod Domest Anim. 2010; 45 Suppl 29-20.
107. **Speca S., Summaria V. and Marano P.** Ultrasonography in gynecology: normal anatomy. European Journal of Ultrasound. 1996; 477-89.
108. **Bushberg J., Seibert J., Leidholdt E. and Boone J.** Ultrasound. In: J.-R. John, A. Snyder and T. DeGeorge, eds. *The essential physics of medical imaging*. 2 ed. Philadelphia, PA: Lippincott Williams & Wilkins; 2002:469-498.
109. **Ng A. and Swanevelder J.** Resolution in ultrasound imaging. Contin Educ Anaesth Crit Care Pain. 2011; 11(5): 186-192.
110. **Martin K.** Properties, limitations and artefacts of B-mode images. In: P. Hoskins, K. Martin and A. Thrush, eds. *Diagnostic Ultrasound: Physics and Equipment*. Cambridge: Cambridge University Press; 2010:64-74.
111. **Edmondson A. J., Fissore R. A., Pashen R. L. and Bondurant R. H.** The use of ultrasonography for the study of the bovine reproductive tract. I. Normal and pathological ovarian structures. Anim Reprod Sci. 1986; 12(3): 157-165.
112. **Duck F. and Shaw A.** Safety of diagnostic ultraound. In: P. Hoskins, K. Martin and A. Thrush, eds. *Diagnostic Ultrasound: Physics and Equipment*. 2 ed. Cambridge: Cambridge University Press; 2010:155-170.
113. **Suortti P. and Thomlinson W.** Medical applications of synchrotron radiation. Phys Med Biol. 2003; 48(13): R1-35.
114. **Elliott A.** Medical Imaging. Nucl Instrum Meth A. 2005; 5461-13.
115. **Hoheisel M.** Review of medical imaging with emphasis on X-ray detectors. Nucl Instrum Meth A. 2006; 563215-224.

116. **Suetens P.** Radiology. *Fundamentals of medical imaging*. Cambridge, UK: Cambridge University Press; 2002:47-64.
117. **Westneat M. W., Socha J. J. and Lee W. K.** Advances in biological structure, function, and physiology using synchrotron X-ray imaging*. Annu Rev Physiol. 2008; 70119-142.
118. **Elder F., Gurewitsch A., Langmuir R. and Pollock H.** Radiation from electrons in a synchrotron. Physical Review. 1947; 71(829): 3, 7, 8.
119. **Garcia-Gutierrez M. and Rueda D.** Bases of synchrotron radiation, light sources, and features of X-ray scattering beamlines. In: M. Gomez, A. Nogales, M. Garcia-Gutierrez and T. Ezquerra, eds. *Applications of synchrotron light to scattering and diffraction in materials and life sciences.* Vol 776. Online: Lecture Notes in Physics; 2009:1-22.
120. **Margaritondo G.** Elements of Synchrotron Light for Biology, Chemistry and Medical Research. Oxford: Oxford University Press; 2002:1-255.
121. **Bharath A.** Introductory Medical Imaging. Vol 27. San Rafael, California: Morgon and Claypool Publishers; 2009:3-37.
122. **Smith N. and Webb A.** X-ray planar radiology and computed tomography. *Introduction to medical imaging: Physics, engineering and clinical applications*. Cambridge, UK: Cambridge University Press; 2011:34-83.
123. **Guy C. and ffytche D.** An introduction to the principles of medical imaging. Revised ed. Covent Garden, London: Imperial College Press; 2005:1-374.
124. **Kitchen M. J., Lewis R. A., Yagi N., Uesugi K., Paganin D., Hooper S. B., Adams G., Jureczek S., Singh J., Christensen C. R., Hufton A. P., Hall C. J., Cheung K. C. and Pavlov K. M.** Phase contrast X-ray imaging of mice and rabbit lungs: a comparative study. The British Journal of Radiology. 2005; 781018-1027.
125. **Lewis R.** Medical phase contrast x-ray imaging: current status and future prospects. Physics in Medicine and Biology. 2004; 493573 - 3583.
126. **Margaritondo G.** Applications of synchrotron light *Elements of synchrotron light for Biology, Chemistry, & Meidcal Research*. Oxford: Oxford University Press; 2002.
127. **Kocsis M. and Snigirev A.** Imaging using synchrotron radiation. Nucl Instrum Meth A. 2004; 525(1–2): 79-84.
128. **Socha J. J., Westneat M. W., Harrison J. F., Waters J. S. and Lee W.-K.** Real-time phase-contrast x-ray imaging: a new technique for the study of animal form and function. BMC Biology. 2007; 5(6).
129. **Baruchel J., Bleuet P., Bravin A., Coan P., Lima E., Madsen A., Ludwig W., Pernot P. and Susini J.** Advances in synchrotron hard X-ray based imaging. Comptes Rendus Physique. 2008; 9(5–6): 624-641.
130. **Monfraix S., Bayat S., Porra L., Berruyer G., Nemoz C., Thomlinson W., Suortti P. and Sovijarvi R.** Quantitative measurement of regional lung gas volume by synchrotron radiation computed tomography. Physics in Medicine and Biology. 2004; 501-11.
131. **Porra L., Monfraix S., Berruyer G., Le Duc G., Nemoz C., Thomlinson W., Suortti P., Sovijarvi A. R. and Bayat S.** Effect of tidal volume on distribution of ventilation assessed by synchrotron radiation CT in rabbit. J Appl Physiol. 2004; 96(5): 1899-1908.
132. **Greenlee K. J., Henry J. R., Kirkton S. D., Westneat M. W., Fezzaa K., Lee W.-K. and Harrison J. F.** Synchrotron imaging of the grasshopper tracheal system: morphological and physiological components of tracheal hypermetry. Am J. Physiol Regul Integr Comp Physiol. 2009; 297R1343 - R1350.

133. **Umetani K., Uesugi K., Kobatake M., Yamamoto A., Yamashita T. and Imai S.** Synchrotron radiation microimaging in rabbit models of cancer for preclinical testing. Nucl Instrum Meth A. 2009; 609(1): 38-49.
134. **Chien C. C., Wang C. H., Wang C. L., Li E. R., Lee K. H., Hwu Y., Lin C. Y., Chang S. J., Yang C. S., Petibois C. and Margaritondo G.** Synchrotron microangiography studies of angiogenesis in mice with microemulsions and gold nanoparticles. Anal Bioanal Chem. 2010; 397(6): 2109-2116.
135. **Tanaka E., Tanaka A., Sekka T., Shinozaki Y., Hyodo K., Umetani K. and Mori H.** Digitized cerebral synchrotron radiation angiography: quantitative evaluation of the canine circle of Willis and its large and small branches. Am J Neuroradiol. 1999; 20(5): 801-806.
136. **Schültke E., Fiedler S., Nemoz C., Ogieglo L., Kelly M. E., Crawford P., Esteve F., Brochard T., Renier M., Requardt H., Le Duc G., Juurlink B. and Meguro K.** Synchrotron-based intra-venous K-edge digital subtraction angiography in a pig model: A feasibility study. European Journal of Radiology. 2010; 73(3): 677-681.
137. **Ohtsuka S., Hyodo K., Jin W., Takeda T., Maruhashi A., Yamaguchi I. and Ando M.** Overview of clinical intravenous coronary angiography both in Japan and at ESRF. Nucl Instrum Meth A. 2005; 548(1-2): 78-83.
138. **Arfelli F., Bonvicini V., Bravin A., Cantatore G., Castelli E., Palma L., Michiel M., Fabrizioli M., Longo R., Menk R., Olivo A., Pani S., Pontoni D., Poropat P., Prest M., Rashevsky A., Ratti M., Rigon L., Tromba G., Vacchi A., Vallazza E. and Zanconati F.** Mammography with synchrotron radiaiton: Phase-detection techniques. Radiology. 2000; 215286 - 293.
139. **Ingal V., Beliaevskaya E., Brianskaya A. and Merkurieva R.** Phase mammography - a new technique for breast investigation. Phys. Med. Biol. 1998; 432555 - 2567.
140. **Keyrilainen J., Bravin A., Fernandez M., Tenhunen M., Virkkunen P. and Suortti P.** Phase-contrast X-ray imaging of breast. Acta Radiol. 2010; 51(8): 866-884.
141. **Pisano E., Johnston R., Chapman D., Geradts J., Iacocca M., Livasy C., Washburn D., Sayers D., Zhong Z., Kiss M. and Thomlinson W.** Human breast cancer specimens: Diffraction enhacned imaging with histologic correlation - improved conspicuity of lesion detail compared with digital radiography. Radiology. 2000; 214895 - 901.
142. **Yoon C. Y., Sung D. J., Lee J. H., Kim A. R., Oh C. W., Je J. H., Weon B. M., Seol S. K., Pyun A., Hwu Y., Margaritondo G., Joo K. J. and Yoon D. K.** Imaging of renal and prostate carcinoma with refractive index radiology. Int J Urol. 2007; 14(2): 96-103.
143. **Blattmann H., Gebbers J. O., Bräuer-Krisch E., Bravin A., Le Duc G., Burkard W., Di Michiel M., Djonov V., Slatkin D. N., Stepanek J. and Laissue J. A.** Applications of synchrotron X-rays to radiotherapy. Nucl Instrum Meth A. 2005; 548(1–2): 17-22.
144. **Christensen C., Singh J., Adams G., Choo-Smith L.-P. and Jackson M.** Infrared and Raman spectroscopic imaging of bovine corpora lutea. Microsc Microanal. 2004; 10(Suppl 2): 1324-1325.
145. **Kuehnel S., Reinhard S., Schmidt J., Herzen J., Beckmann F., Kleinteich T. and Kupfer A.** Evolutionary reproductive biology of amphibians: Novel insights using synchrotron based highresolution X-ray computed microtomography. *Photon Science-HASYLAB Annual report*. DESY Photon Science2009:1-2.

146. **Bergmann P., Laumann M., Cloetens P. and Heethoff M.** Morphology of the internal reproductive organs of *Archegozetes longisetosus* Aoki (Acari, Oribatida). Soil Organisms. 2008; 80(2): 171-195.
147. **Wood B. R., Chernenko T., Matthaus C., Diem M., Chong C., Bernhard U., Jene C., Brandli A. A., McNaughton D., Tobin M. J., Trounson A. and Lacham-Kaplan O.** Shedding new light on the molecular architecture of oocytes using a combination of synchrotron Fourier transform-infrared and Raman spectroscopic mapping. Anal Chem. 2008; 80(23): 9065-9072.
148. **Kim A. M., Bernhardt M. L., Kong B. Y., Ahn R. W., Vogt S., Woodruff T. K. and O'Halloran T. V.** Zinc sparks are triggered by fertilization and facilitate cell cycle resumption in mammalian eggs. ACS Chem Biol. 2011; 6(7): 716-723.
149. **Han L., Monné M., Okumura H., Schwend T., Cherry A. L., Flot D., Matsuda T. and Jovine L.** Insights into egg coat assembly and egg-sperm interaction from the X-ray structure of full-length ZP3. Cell. 2010; 143(3): 404-415.
150. **Zhou S. A. and Brahme A.** Development of phase-contrast X-ray imaging techniques and potential medical applications. Phys Med. 2008; 24(3): 129-148.
151. **Chapman D., Pisano E., Thomlinson W., Zhong Z., Johnston R. E., Washburn D., Sayers D. and Malinowska K.** Medical applications of diffraction enhanced imaging. Breast Disease. 1998; 10(3-4): 197-207.
152. **Chapman D., Thomlinson W., Johnston R. E., Washburn D., Pisano E., Gmur N., Zhong Z., Menk R., Arfelli F. and Sayers D.** Diffraction enhanced x-ray imaging. Phys Med Biol. 1997; 42(11): 2015-2025.
153. **Pagot E., Fiedler S., Cloetens P., Bravin A., Coan P., Fezzaa K., Baruchel J., Hartwig J., Von Smitten K., Leidenius M., Karjalainen-Lindsberg M. and Keyrilainen J.** Quantitative comparison between two phase contrast techniques: diffraction enhanced imaging and phase propagation imaging. Phys Med Biol. 2005; 50(4): 709 - 724.
154. **Liu C., Zhang Y., Zhang X., Yang W., Peng W., Shi D., Zhu P., Tian Y. and Huang W.** X-ray diffraction-enhanced imaging of uterine leiomyomas. Med Sci Monitor. 2005; 11(5): MT33-38.
155. **Li J., Zhong Z., Lidtke R., Kuettner K. E., Peterfy C., Aliyeva E. and Muehleman C.** Radiography of soft tissue of the foot and ankle with diffraction enhanced imaging. J Anat. 2003; 202(5): 463-470.
156. **Bravin A., Keyrilainen J., Fernandez M., Fiedler S., Nemoz C., Karjalainen-Lindsberg M. L., Tenhunen M., Virkkunen P., Leidenius M., von Smitten K., Sipila P. and Suortti P.** High-resolution CT by diffraction-enhanced x-ray imaging: mapping of breast tissue samples and comparison with their histo-pathology. Phys Med Biol. 2007; 52(8): 2197-2211.
157. **Faulconer L., Parham C., Connor D., Zhong Z., Kim E., Zeng D., Livasy C., Cole E. B., Kuzmiak C., Koomen M., Pavic D. and Pisano E.** Radiologist evaluation of an x-ray tube-based diffraction-enhanced imaging prototype using full-thickness breast specimens Acad Radiol. 2009; 161329-1337.
158. **Mollenhauer J., Aurich M. E., Zhong Z., Muehleman C., Cole A. A., Hasnah M., Oltulu O., Kuettner K. E., Margulis A. and Chapman L. D.** Diffraction-enhanced X-ray imaging of articular cartilage. Osteoarth Cartilage. 2002; 10(3): 163-171.

159. **Parham C., Zhong Z., Connor D. M., Chapman L. D. and Pisano E. D.** Design and implementation of a compact low-dose diffraction enhanced medical imaging system. Acad Radiol. 2009; 16(8): 911-917.
160. **Arfelli F., Assante M., Bonvicini V., Bravin A., Cantatore G., Castelli E., Dalla Palma L., Di Michiel M., Longo R., Olivo A., Pani S., Pontoni D., Poropat P., Prest M., Rashevsky A., Tromba G., Vacchi A., Vallazza E. and Zanconati F.** Low-dose phase contrast x-ray medical imaging. Phys Med Biol. 1998; 43(10): 2845-2852.
161. **Olivo A., Rigon L., Vinnicombe S. J., Cheung K. C., Ibison M. and Speller R. D.** Phase contrast imaging of breast tumours with synchrotron radiation. Applied Radiation and Isotopes. 2009; 67(6): 1033-1041.
162. **Fitzgerald R.** Phase-sensitive X-ray imaging. Physics Today. 2000; 53(7): 23-26.
163. **Snigirev A., Snigireva I., Kohn V., Kuznetsov S. and Schelokov I.** On the possibilities of x-ray phase contrast microimaging by coherent high-energy synchrotron radiation. Rev. Sci. Instrum. 1995; 66(12): 5486 - 5492.
164. **Momose A., Washiro W., Takeda Y., Suzuki Y. and Hattori T.** Phase-imaging with an x-ray talbot interferometer. JCPDS-International Centre for Diffraction Data. 2006; 21-30.
165. **Pinzer B. R., Cacquevel M., Modregger P., McDonald S. A., Bensadoun J. C., Thuering T., Aebischer P. and Stampanoni M.** Imaging brain amyloid deposition using grating-based differential phase contrast tomography. Neuroimage. 2012; 61(4): 1336-1346.
166. **Weitkamp T., David C., Bunk O., Bruder J., Cloetens P. and Pfeiffer F.** X-ray phase radiography and tomography of soft tissue using grating interferometry. Eur J Radiol. 2008; 68(3, Supplement): S13-S17.
167. **Donath T., Pfeiffer F., Bunk O., Grunzweig C., Hempel E., Popescu S., Vock P. and David C.** Toward clinical X-ray phase-contrast CT: demonstration of enhanced soft-tissue contrast in human specimen. Invest Radiol. 2010; 45(7): 445-452.
168. **Momose A.** Phase-sensitive imaging and phase tomography using X-ray interferometers. Optics Express. 2003; 11(9): 2303 - 2314.
169. **Arfelli F.** Synchrotron light and imaging systems for medical radiology. Nucl Instrum Meth A. 2000; 45411-25.
170. **Ketcham R. and Carlson W.** Acquisition, optimization and interpretation of X-ray computed tomographic imagery: applications to the geosciences. Computers & Geosciences. 2001; 27381-400.
171. **Smith N. and Webb A.** General image characteristics, data acquisition and image reconstruction. *Introduction to medical imaging: Physics, engineering and clinical applications*. Cambridge, UK: Cambridge University Press; 2011:1-30.
172. **Sijbers J. and Postnov A.** Reduction of ring artefacts in high resolution micro-CT reconstructions. Phys Med Biol. 2004; 49(14): N247-253.

# Chapter 2

## GENERAL OBJECTIVES AND HYPOTHESIS

The overall objective of the work presented was to determine if synchrotron-based biomedical imaging techniques would be effective for imaging ovaries compared to conventional ultrasonography and histology. The specific objectives were to: 1) explore Diffraction Enhanced Imaging (DEI) as a technique for evaluating bovine ovaries (Chapter 3), and 2) evaluate Propagation-Based CT (PB-CT) and Talbot Grating Interferometry-CT (TGI-CT) techniques for evaluating both bovine and human ovaries (Chapter 4).

The general hypothesis was that DEI, PB-CT and TGI-CT synchrotron techniques would provide improved image contrast for evaluating ovarian structures (i.e., follicles ≥2mm, small antral follicles <2mm, corpora lutea, cumulus oocyte complexes, and cell layers of the follicle wall) compared to conventional ultrasonography and histology.

The following specific hypotheses were examined.

Study 1 (Chapter 3 - Diffraction Enhanced Synchrotron Imaging of Bovine Ovaries *Ex Vivo*):

- Follicle and luteal diameter measurements would be more accurately assessed with DEI versus ultrasonography, using histology as a reference
- The number of follicles ≥2mm detected with DEI would be greater than that of ultrasonography.
- DEI would enable the detection of smaller antral follicles compared to ultrasonography.
- DEI would enable the detection of cumulus oocyte complexes and small antral follicles <2mm, whereas ultrasonography would not.

Study 2 (Chapter 4 - Synchrotron Imaging of Bovine and Human Ovaries *Ex Vivo:* Propagation-based Phase Contrast and Talbot Grating Interferometry Techniques):

- Follicle and luteal diameter measurements would be more accurately assessed with PB-CT versus ultrasonography, using histology as a reference.
- Follicle wall measurements would be more accurately assessed using PB-CT versus ultrasonography.
- PB-CT would enable the detection of smaller follicles compared to ultrasonography.
- PB-CT and TGI-CT would enable the detection of cumulus oocyte complexes and small antral follicles <2mm, whereas ultrasonography does not.

# Chapter 3

## Diffraction Enhanced Synchrotron Imaging of Bovine Ovaries *Ex Vivo*

Upekha Basnayaka BSc[1], Dean Chapman PhD[2], Gregg Adams DVM, PhD[3], Tomasz Wysokinski PhD[4], George Belev PhD[4], Angela Baerwald PhD[1]

[1]Department of Obstetrics, Gynecology & Reproductive Sciences, College of Medicine, University of Saskatchewan, Saskatchewan, Canada

[2]Department of Anatomy & Cell Biology, College of Medicine, University of Saskatchewan, Saskatchewan, Canada

[3]Department of Veterinary Biomedical Sciences, Western College of Veterinary Medicine, University of Saskatchewan, Saskatchewan, Canada

[4]Canadian Light Source, Saskatoon, Saskatchewan, Canada

## 3.0 Preface

The following study (Chapter 3) was conducted to qualitatively and quantitatively compare Diffraction Enhanced Imaging (DEI) and conventional ultrasonography for imaging bovine ovaries. In a preliminary study, Christensen et al. showed that DEI offers promise for imaging bovine ovaries. The study described in this chapter is an extension of the earlier study to compare both DEI and diagnostic ultrasonography to the gold standard, histology. DEI has been documented to be an effective synchrotron technique for imaging soft tissues, such as breast and lung tissue. The aim of our study was to determine whether DEI synchrotron methods are effective for imaging bovine and human ovaries.

This manuscript will be submitted for publication in the Journal of Medical Imaging and Radiation Sciences (JMIRS). The contributions of the primary author (Upekha Basnayaka) to this manuscript include the following: 10% study design, 70% data collection, 65% data analyses/interpretation, 45% manuscript preparation and 80% presentation of study findings. The co-authors are acknowledged for contributing to study design, data collection and developing the manuscript.

Research described in the following paper was performed at the Canadian Light Source (CLS, Saskatoon, SK) which is supported by the Natural Sciences and Engineering Research Council of Canada, the National Research Council Canada, the Canadian Institutes of Health Research (CIHR), the Province of Saskatchewan, Western Economic Diversification Canada, and the University of Saskatchewan. The authors would like to acknowledge Dr. Jaswant Singh and Darren Nesbitt (Veterinary Biomedical Sciences, Western College of Veterinary Medicine, University of Saskatchewan) for their assistance in conducting histological analysis in the present study. Appreciation is also expressed to Adam Webb at the CLS for his expertise in acquiring and analyzing synchrotron data. Funding for this study was provided by a CIHR-Training Grant in Health Research Using Synchrotron Techniques as well as new faculty start-up funds from the College of Medicine at the University of Saskatchewan.

### 3.1 Abstract

**Objectives:** The objective of this study was to test the hypothesis that Diffraction Enhanced Imaging (DEI), a synchrotron X-ray imaging technique, would provide greater contrast for evaluating bovine ovaries compared to conventional diagnostic ultrasonography.

**Materials and Methods:** Bovine ovaries were evaluated *ex vivo*: fresh without radiographic arterial contrast (n=2), fresh with contrast (n=1), preserved in 10% formalin without contrast (n=2), and preserved with contrast (n=1). Each ovary was imaged with DEI and subsequently with US and histology. The ability to visualize and differentiate pre-antral and antral follicles, corpora lutea (CL) and cumulus oocyte-complexes (COC) were compared using DEI, US and histology. The diameter of follicles and CL were measured and compared using ultrasonography, DEI, and histology. The diameter of the smallest follicle detected was reported using each of the three imaging methods. The number of antral follicles (Antral Follicle Count; AFC; ≥2mm) was compared between US and DEI.

**Results:** DEI enabled the detection of 71% of follicles and 67% of CL that were detected using ultrasonography. However, DEI did not allow the detection of COC and cell layers of the follicle wall that were visualized with histology. Luteal tissues were not easily distinguished using DEI; DEI was inferior for differentiating follicles and CL compared to US. Mean follicle diameter was similar between DEI (9.6 ± 2.4 mm), ultrasonography (9.0 ± 2.6 mm), and histology (6.9 ± 1.9 mm) in fresh ovaries with no contrast (P = 0.7). However, mean follicle diameter in fresh ovaries without contrast was greater using both DEI (4.0 ± 0.4 mm) and ultrasonography (3.9 ± 0.3 mm) compared to histology (2.2 ± 0.4 mm), (P=0.01). Mean CL diameter was similar between DEI (11.6 ± 1.7 mm), ultrasonography (9.3 ± 0.4 mm), and histology (9.6 ± 0.4 mm), (P = 0.34). The mean diameter of the smallest follicle detected was similar between DEI (3.1±0.4 mm) and ultrasonography (3.0 ± 0.7 mm), albeit both DEI and ultrasonography measurements were greater than histology (0.4 ± 0.04 mm), (P<0.0001). Mean AFC was similar between ultrasonography (6.5 ± 0.7 mm, fresh with no contrast; 6.5 ± 2.5 mm, preserved with no contrast) and DEI ( 4.5 ± 0.5 mm, fresh with no contrast; 6.5 ± 0.5 mm, preserved with no contrast), (P > 0.05). Preservation of tissues and the injection of contrast into the ovarian arteries did not alter the quality of images obtained with DEI.

**Discussion:** The contrast resolution of antral follicles, CL and COC in bovine ovaries using DEI was inferior to ultrasonography and histology. Additional synchrotron techniques, such as Phase-Contrast Computed Tomography (CT) or DEI-CT, may prove more effective for imaging ovaries *ex vivo*.

**Keywords:** Bovine – Ovary – Synchrotron – Ultrasonography – Diffraction Enhanced Imaging

### 3. 2 Introduction

The evaluation of morphologic and functional properties of human tissues is essential for understanding physiology and pathophysiology. The most commonly used method for examining reproductive tissues in women is conventional ultrasonography [1]. Ultrasonographic imaging is considered to be rapid, clinically safe and portable [1-4]. An ultrasonographic image consists of 2-dimensional pixels or 3-dimensional voxels with varying degrees of brightness. The brightness of each pixel or voxel corresponds to the amplitude of the echoes created as high frequency sound waves are reflected from tissue interfaces [5,6]. Human ovaries can be imaged either transvaginally or transabdominally [2,4]. Greater resolution for imaging the ovaries is achieved using a transvaginal versus a transabdominal probe [4]. Ultrasonography has enabled the assessment of ovarian structure and function (i.e., follicle and luteal development, ovulation), as well as detection of pathological abnormalities of the ovary (i.e., polycystic ovaries, ovarian tumors) [4,6-12].

Despite providing a direct and non-invasive method for examining the ovaries, ultrasonography is limited in its ability to provide high-resolution images of ovarian microanatomy. Conventional transvaginal ultrasonography enables the detection and measurement of structures ≥2 mm in diameter in the ovaries [13,14]. Thus, pre- and early- antral (i.e., fluid-filled) ovarian follicles, as well as the female germ cells (i.e., oocytes), are not visualized [15-17]. Ultrasonographic imaging in patients with a large body mass is often challenging because a lower frequency is required to penetrate deeper in to the target organs resulting in a lesser resolution of structures [18]. In addition, the presence of bowel gas can impede the transmission of ultrasound beams and create artifacts when imaging the ovaries. Thus, limitations of conventional ultrasonography provide rationale for the development of novel high resolution tools to image ovaries for both clinical and research purposes.

The synchrotron, a high energy particle accelerator, is a novel tool for imaging soft tissues. The synchrotron provides a wide X-ray energy spectrum with a high photon flux that allows the selection of a monochromatic photon beam with a narrow wavelength band [19-24]. The selection of a specific energy allows samples to be imaged with less radiation exposure or dose compared to conventional X-ray imaging [20,25]. Synchrotron radiation can be applied to studies in various fields including material science, crystallography, micro-spectroscopy, and biomedical imaging [19].

Diffraction Enhanced Imaging (DEI) is a type of phase-sensitive or refraction-based synchrotron imaging which can be used for imaging soft tissues. DEI involves the use of a crystal, known as an analyzer, which is placed between the sample and detector [26]. The setup for DEI imaging is shown in Figure 3.1. The analyzer can be placed in various positions on a rocking curve to obtain data from which images can be obtained of refraction, absorption, and scatter rejection [26,27]. The relative energy intensity of DEI is a function of the angular position of the crystal. X-rays that are aligned with the analyzer are detected [28]. Apparent absorption images are created by mapping contrast arising from the absorption and scattering of X-rays. X-ray scatter arises from small structures within the sample [29,30]. The majority of scatter from the sample is eliminated by the small angular acceptance of the crystal analyzer. Placing the analyzer at the top of the rocking curve yields an image that is nearly free from scatter. Therefore, DEI images from the top contain contrast from absorption and rejection of small and ultra-small X-ray scattering [29]. In conventional X-ray radiography, the separation of scatter from absorption contrast is not possible [30]. Refraction DEI images contain only refracted contrast information which arises from density variations in the sample [26]. In planar or 2D DEI, the structures within the entire sample are superimposed in a single image. DEI allows the investigator to detect minute changes in the projected refractive index of a sample, such as boundaries or edges which are often undetected with conventional radiography [26]. Another advantage of DEI is that it is not highly dependent on imaging energy allowing samples to be imaged with a lower radiation dose [26,31].

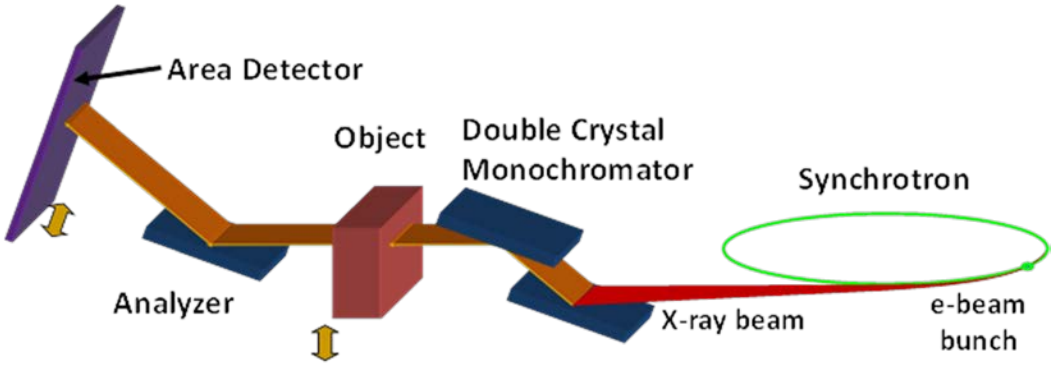


**Figure 3.1** Synchrotron beamline setup for Diffraction Enhanced Imaging (Chapman, et al., 2013, unpublished)

DEI has been used in humans to image bone and soft tissues of the foot and ankle [32], normal and pathological breast tissue [30,33,34], articular cartilage in knee joints [35] and uterine leiomyomas [29]. DEI has been further used to examine lung damage and liver tissue morphology in rats [36,37]. A preliminary study was conducted in 2002 to examine DEI of a single excised bovine ovary [38]. Results obtained from this early research indicated that bovine ovarian follicles >4 mm and corpora lutea (CL) could be detected using DEI at 40 keV [38]. This proof-of-principle study, however, did not include comparisons with conventional imaging methods or histology. Animal species are often used for initial imaging studies because of ethical restrictions associated with using human tissues. The bovine species has been well established as a model for studying reproductive functions in women [7,39]. Further investigations are required to determine the effectiveness of synchrotron DEI for evaluating bovine ovarian anatomy and physiology. Research of this nature may assist in optimizing medical imaging tools for the research and clinical evaluation of human ovaries.

The objective was to determine the effectiveness of DEI for evaluating bovine ovaries *ex vivo*. We hypothesized that DEI would provide greater contrast resolution for detecting and differentiating ovarian structures including antral follicles <2 mm, cell layers of the follicle wall, cumulus oocyte complexes (COC), and CL compared to conventional diagnostic ultrasonography.

## 3. 3 Materials and Methods

### 3.3.1 Study Samples

A prospective, observational pilot study was conducted from 2011 – 2013. Fresh bovine ovaries (n= 6) were obtained from local abattoirs. The ovarian artery of each specimen was flushed with saline immediately after collection, and the ovaries were transported in normal saline at room temperature to the Canadian Light Source (CLS) synchrotron facility at the University of Saskatchewan. The CLS operates at an energy of 2.9 GeV and a current of 250 mA [40]. The ovaries were imaged in the following conditions: fresh without contrast (n=2), fresh with an ovarian artery injection of 4 mL of iodine-based contrast agent (Ioversol, Optiray 240) (n=1), preserved in 10% formalin with no contrast (n=2), or preserved with contrast (n=1). The gross morphology of each ovary was imaged using a digital camera (Samsung NV24HD, Korea). Ethical approval for conducting this study was obtained from the Animal Research Ethics Board at the University of Saskatchewan.

### 3.3.2 Imaging Techniques

Ovarian samples were imaged with planar DEI at the BioMedical Imaging and Therapy (BMIT) beamline at the CLS using an energy of 40 keV and pixel size of 20 µm. Ovaries were placed in a saline-filled, rectangular, plastic container (6 cm x 3.5 cm x 2 cm) with a piece of rubber tubing on the bottom for stabilization (Figure 3.2). Visible air bubbles inside the container were manually removed using a pipette before imaging. A silicon crystal with a 2, 2, 0 lattice configuration was used. Images were obtained at the top, 0.5 (+/-), and 0.25 (+/-) positions on the rocking curve using a CCD array detector and camera (Photonic Science Ltd, Robertsbridge, East Sussex, UK).

**Figure 3.2** Sample setup for imaging a bovine ovary by Diffraction Enhanced Imaging at the Canadian Light Source synchrotron

Following synchrotron imaging, ovarian samples were imaged using a portable diagnostic ultrasonographic system equipped with a 6.6 MHz convex-array probe (MyLab Five, Esaote, Indianapolis, Indiana, USA). Ovaries were placed in degassed saline and imaged ultrasonographically along the long axis of the ovary. Imaging was conducted at a penetration depth of 6 cm using an overall gain of 52% for all ovaries, with no magnification. One focal zone was placed at a depth of 2.5 cm.

Ovarian samples were placed in 10% Formalin immediately following synchrotron and ultrasonographic imaging. Ovaries were serially sectioned at 5 µm thickness using a microtome. Every 4$^{th}$ section was selected for hematoxylin and eosin staining. Images of the histological slides were obtained using a digital camera with a 50mm focal length (Nikon D90, Nikon Inc., Melville, NY, USA).

### 3.3.3 Qualitative Analyses

Synchrotron images were reconstructed using ImageJ (Version 1.46, National Institutes of Health, Bethesda, MA, USA). DEI image reconstruction included images from the peak and both sides of the rocking curve. Apparent absorption and refraction images were also obtained by applying an algorithm on a pixel-by-pixel basis, as described by Chapman et al [26]. Interactive Data Language (ITT Exelis., Boulder, Colorado, USA) was used to remove artifacts seen as dark horizontal bands from the DEI images. Ultrasonographic images were evaluated using Sante

DICOM Editor (Version 3.1.23, Athens, Greece). Histologic images were edited using ViewNX™ (Version 2.3.0, Nikon Inc., Melville, NY, USA). Ovarian follicles were classified as either normal or atretic, based on histologic characteristics. Healthy follicles were characterized by the presence of a homogenous and continuous lumen-granulosa and granulosa-theca interface, as well as a tightly compacted COC [41]. Follicular atresia was characterized by the presence of nuclear condensation in the granulosa cell layer, hypertrophy of theca interna cells, presence of cytoplasmic droplets, hyalinized zona pellucida, and separation of cumulus cells [41-43]. Qualitative investigations using the three imaging techniques (DEI, ultrasonography and histology) included the ability to detect and differentiate ovarian structures (i.e., follicles, CL and COC), the quality of images obtained and the presence of artifacts or noise.

### 3.3.4 Quantitative Analyses

Structures of interest in corresponding DEI, ultrasonographic and histologic images were measured using ImageJ (Version 1.46, National Institutes of Health, Bethesda, MA, USA). For each follicle ≥2 mm or CL detected, diameter was calculated as the mean of the longest and widest perpendicular measurements (i.e., length and width) along the long axis of the ovary. Diameter measurements were made using a magnification of 1.5X for DEI images, 2.5X for ultrasonographic images, and 1.5X for histology images. The smallest follicle detected with all three imaging techniques was also reported [16]. Antral Follicle Count (AFC, defined as the number of follicles ≥2 mm detected) was tabulated for each ovary using both ultrasonography (1.33X magnification) and DEI (1.33X magnification). All images were scaled according to their pixel dimensions using ImageJ (Version 1.46, National Institutes of Health, Bethesda, MA, USA).

The primary study outcome measure was the ability to detect follicle, CL, or COC within the ovaries. Secondary outcomes measures included follicle diameter, luteal diameter and AFC. Study endpoints were compared among DEI, ultrasonography and histology techniques using One-Way Analysis of Variance (ANOVA) with Tukey's post hoc tests when significance ($P<0.05$) was detected. Statistical analyses were conducted using SPSS (Version 20.0, Chicago, IL, USA).

### 3.4 Results

#### 3.4.1 Qualitative Findings

DEI images of scatter rejection (top of the rocking curve), apparent absorption and refraction (both from the sides of the rocking curve) were obtained for each ovary (Figure 3.3a-c). Antral follicles of varying diameters were characterized as circular structures with less (Figure 3.3a) or similar (Figure 3.3c) contrast compared to the surrounding tissue. All follicles detected within the ovary were superimposed within a single DEI image (Figure 3.3c). The refraction image (Figure 3.3c) was more effective for discriminating the borders of antral follicles and CL compared to the scatter rejection (Figure 3.3a) and absorption (Figure 3.3b) images. The amount of contrast in the apparent absorption images was insufficient to visualize follicles or CL (Figure 3.3b). Artifacts, visualized as dark horizontal bands across the images (Figure 3.3b, c), were initially observed using DEI. Artifacts were attributed to the image reconstruction process and were removed prior to quantitative analyses.

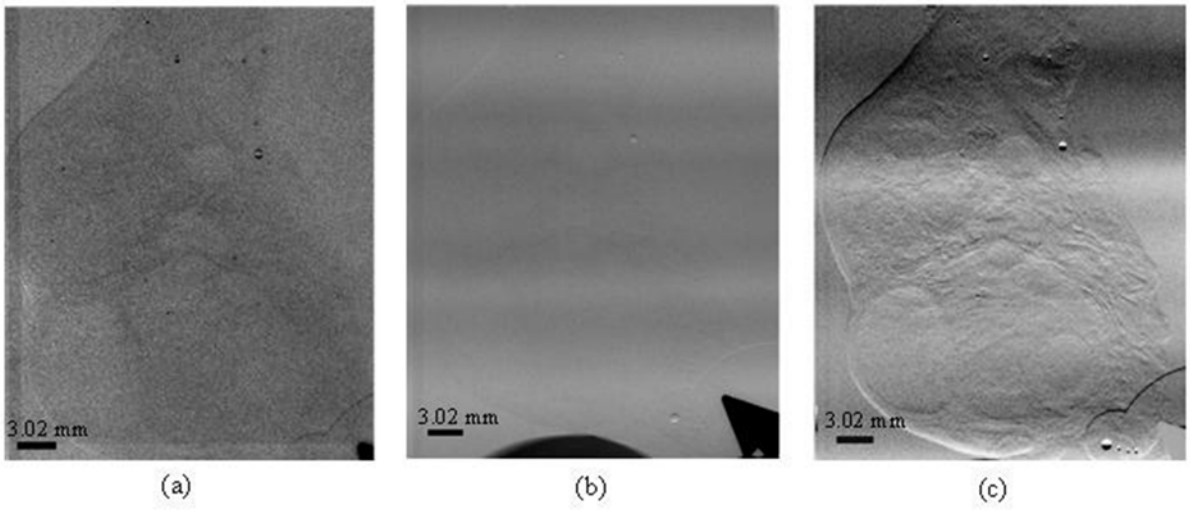


**Figure 3. 3** Diffraction enhanced images of a fresh bovine ovary with contrast. Images of the top of the rocking curve (a; scatter-free), apparent absorption (b), and refraction (c) are shown

Images of gross morphology (a, b), ultrasonography (c, d), DEI (e, f), and histology (g, h) of two fresh (i.e., unpreserved) ovaries are shown in Figure 3.4. In the ultrasonographic images, antral follicles appeared as dark, anechoic, circular structures with a poorly-defined border

(Figures 3.4c, d). In DEI images, follicles appeared as circular structures with a well-defined border and homogeneous echotexture within the antral cavity (Figures 3.4e, f). Antral cavity heterogeneity was observed when multiple follicles were superimposed on each other (Figure 3. 4f). About 37/52 (71%) of follicles ≥2 mm detected with ultrasonography were detected with DEI. COC were not detected in either ultrasonogrpahy or DEI images. COC, however, were detected as circular protrusions into the follicular antrum in some of the histological sections. Individual cell layers of the follicle wall (i.e., granulosa and theca) were detected with histology, but not DEI or ultrasonography. Ovarian blood vessels that were visualized within the ovarian medulla with histology were not detected in the DEI or grey-scale ultrasonographic images.

Six out of nine (67%) of CL identified with ultrasonography were retrospectively identified using DEI. In Figure 3.4c, the CL was visualized ultrasonographically as a circular structure containing a heterogeneous central cavity, representing a hemorrhagic cyst. The blood-filled central cystic cavity was visualized ultrasonographically to be hyperechoic compared to antral follicles. The CL was identified in the DEI images as a well-circumscribed circular structure with or without a central fluid-filled cavity. In Figure 3.4e, the contrast of the CL in the DEI images was similar to neighboring follicles in many cases; thus, it was difficult to differentiate CL from follicles using DEI.

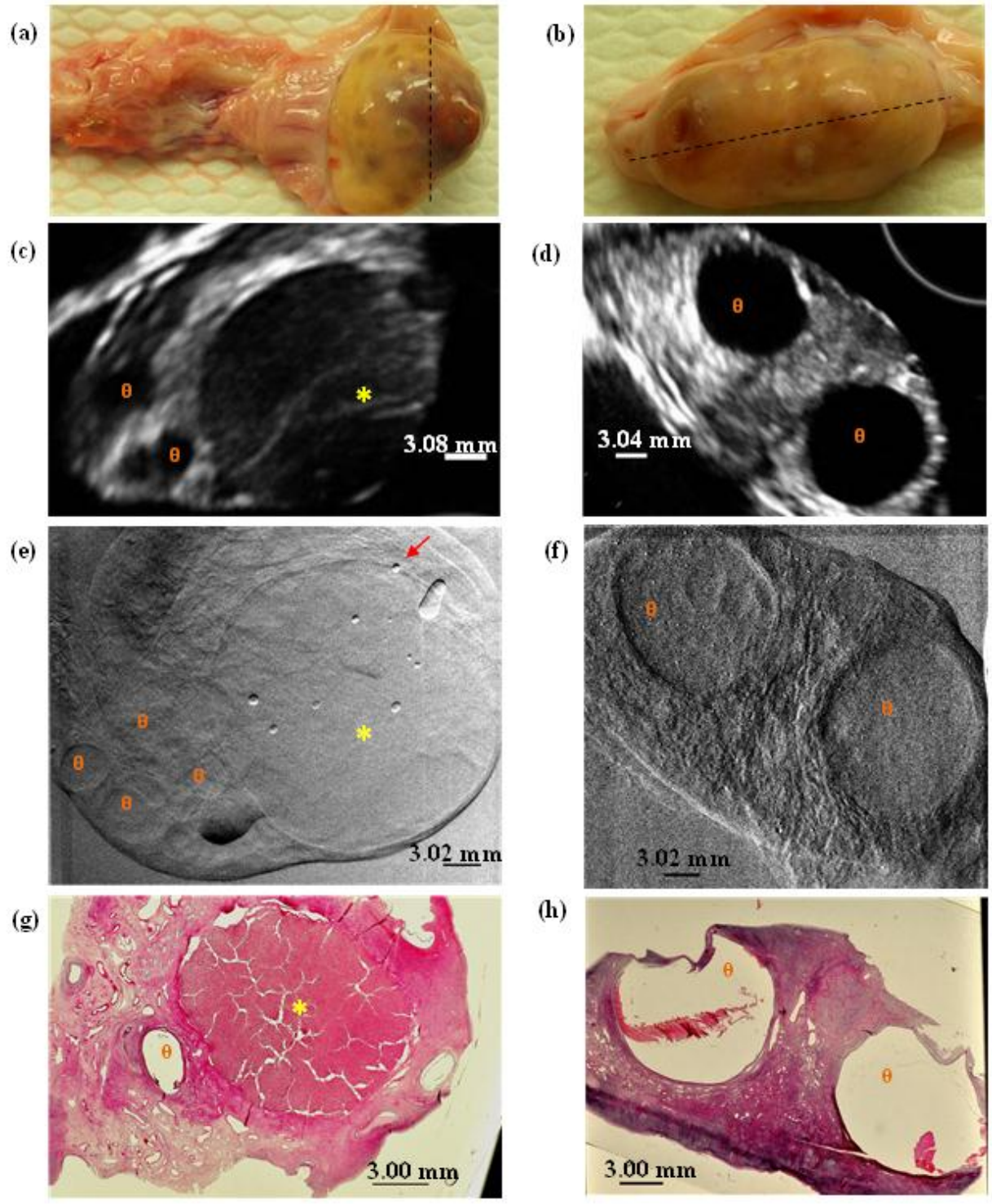


**Figure 3.4** Gross morphology (a, b), ultrasonographic (c, d), DEI (e, f; at +0.5 position on the rocking curve), and histologic (g, h) images of two separate fresh bovine ovaries. Ovarian samples imaged with (a, c, e, g) and without (b, d, f, h) contrast are shown. Examples of ovarian follicles (orange θ), corpora lutea (yellow *), and air bubbles (red arrow) are indicated. Dashed lines on the gross images indicate the plane of sectioning.

Air bubbles were visualized in some DEI images as bright white (high contrast), circular structures <1.0 mm surrounded by a black halo (Figures 3.4e). Several small high contrast circular structures denser than air bubbles (measuring approximately 0.25 mm) were identified in one sample (Figure 3.4f). We postulated that these structures represented microcalcifications of the ovary. However, the identity of these structures was not confirmed in the corresponding histologic images.

The quality of the DEI images was not influenced by the injection of contrast (Figure 3.4 e, f) or preservation (Figure 3.5 a, b)

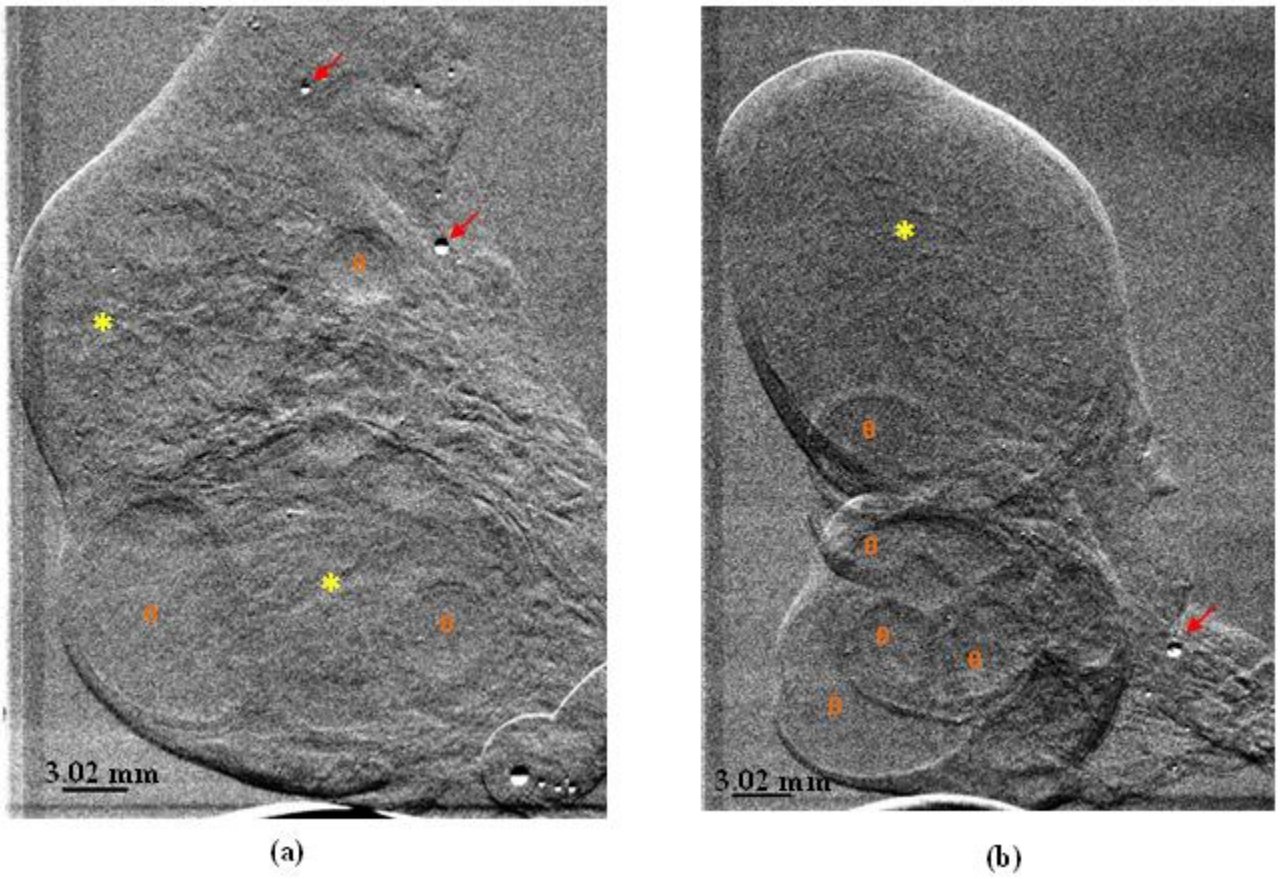


**Figure 3.5** Diffraction enhanced images of a fresh (a) and formalin-fixed (b) bovine ovary. Images were taken at the +0.5 position of the rocking curve. Examples of ovarian follicles (orange θ), corpora lutea (yellow *) and air bubbles (red arrow) are shown. Other follicles not indicated in the image are also present.

### 3.4.2 Quantitative Findings

Corresponding ovarian structures (i.e., follicles, CL) visualized with all three imaging techniques (n=3) were evaluated quantitatively. The DEI image attributes of normal versus atretic were not different (P>0.05); therefore, data for normal and atretic follicles were combined. However, the use of radiographic contrast appeared to confound the effect of imaging techniques on ovarian measurements. Therefore, data are reported separately for ovaries evaluated with versus without contrast.

Follicle ≥2 mm and CL diameter measurements made from DEI, ultrasonographic and histologic images are compared in Table 3.1. Mean follicle diameter in fresh ovaries with contrast was similar between DEI and ultrasonography; however, follicle diameter was greater for both DEI and ultrasonography compared to histology (P = 0.01). Mean follicle diameter in fresh ovaries without contrast was similar among the 3 techniques (P>0.05). Mean CL diameter in fresh ovaries without contrast were similar between DEI, ultrasonography, and histology (P>0.05).

**Table 3.1** Ovarian follicle and corpus luteum (CL) diameter (Mean ± Standard Error) assessed by histology, ultrasonography, and Diffraction Enhanced Imaging (DEI) of 3 fresh excised bovine ovaries (n=number of follicles or corpora lutea)

| Sample Condition | n | Histology (mm) | Ultrasonography (mm) | DEI (mm) | P-value |
|---|---|---|---|---|---|
| *Follicle Diameter* | | | | | |
| Fresh – with contrast | 4 | $2.2 \pm 0.4^{a}$ | $3.9 \pm 0.3^{b}$ | $4.0 \pm 0.4^{b}$ | **0.01** |
| Fresh – no contrast | 4 | $6.9 \pm 1.9^{a}$ | $9.0 \pm 2.6^{a}$ | $9.6 \pm 2.4^{a}$ | 0.70 |
| *CL Diameter* | | | | | |
| Fresh – no contrast | 2 | $9.6 \pm 0.4^{a}$ | $9.3 \pm 0.4^{a}$ | $11.6 \pm 1.7^{a}$ | 0.34 |

[a, b] Within rows, values with different superscripts are different (P < 0.05)

Mean AFC measurements were compared between DEI and ultrasonography (Table 3.2). There were no differences in mean AFC between DEI and ultrasonography for fresh or preserved samples (without contrast P>0.05)

**Table 3.2** Mean Antral Follicle Count (AFC; Mean ± Standard Error) in excised bovine ovaries assessed by ultrasonography versus Diffraction Enhanced Imaging (DEI)

| Ovarian Sample | Number of ovaries | Ultrasonography | DEI | P-value |
|---|---|---|---|---|
| Fresh – with contrast | 1 | 17 | 7 | - |
| Fresh – no contrast | 2 | 6.5± 0.7 | 4.5 ± 0.5 | 0.11 |
| Preserved – with contrast | 1 | 10 | 8 | - |
| Preserved – no contrast | 2 | 6.5 ± 2.5 | 6.5 ± 0.5 | 1.00 |

The imaging sensitivity (defined as the smallest follicle detected) of DEI was similar to that of ultrasonography, (P=0.225) but the sensitivity of both DEI and ultrasonography was inferior to that of histology (3.1 ± 0.4mm, 3.0 ± 0.7mm, 0.4 ± 0.04 mm, respectively; P<0.0001).

### 3. 5 Discussion

In this pilot study, we investigated the effectiveness of DEI synchrotron techniques for evaluating bovine ovaries *ex vivo*. Overall, we concluded that DEI (at 40 keV imaging energy, 20 µm resolution) was not an effective method for imaging the macro and/or microanatomic features of bovine ovaries in comparison to conventional 2D ultrasonography and histology. Thus, our hypothesis was not supported.

DEI was capable of detecting antral ovarian follicles >2 mm as well as CL. However, only 2/3 of follicles and CL imaged ultrasonographically were detected with DEI. The superimposition of follicles in DEI images made identifying individual follicles and CL difficult. It was more challenging to identify individual follicles from ovaries with a larger AFC with DEI versus ultrasonography. Furthermore, we were not able to differentiate antral follicles from CL in DEI images because the contrast of the luteal tissue was similar to that of the follicles. We attributed the inferior contrast resolution of the DEI images to the small variation between the projected refractive indices of the luteal tissues and follicles [26]. Other microscopic details of the ovary observed histologically (including COC, vasculature, cell layers of the follicle wall,

and small follicles <2 mm) were not visualized with either DEI or ultrasonography. Although the ability to consistently detect antral follicles and CL was limited, DEI was as accurate as ultrasonography for measuring follicular and luteal diameter. Both DEI and ultrasonography, however, were inferior to histology for measuring the diameter of follicles and CL in ovaries with contrast. Overall, we concluded that DEI was inferior to ultrasonography for imaging antral follicles and CL.

AFC has been shown to be one of the best predictors of ovarian reserve (i.e., the number of pre-antral and antral follicles within the ovaries) in women. As a result, AFC can be used to predict the timing of onset of menopause as well the ovarian response to human assisted reproductive therapies [39,44,45]. Current methods for measuring AFC are limited to detecting follicles ≥2 mm in diameter. In addition, there is a great degree of intra and interobserver variability in measuring AFC, in particular for follicles < 2 mm. In the present study, AFC for follicles ≥ 2mm was similar using DEI and conventional 2D ultrasonography. However, DEI did not allow the detection and quantification of antral follicles less than 2 mm in diameter. Therefore, we concluded that DEI does not provide an additional advantage over ultrasonography for determining AFC.

One of the biggest limitations of our study was the sample size. In general, it takes about 30 – 60 minutes to obtain five images on the DEI rocking curve. Each ovary took approximately 2-3 hours to image due to beam instability issues, thereby limiting the number of samples we could image within a given period of time. The evaluation of 6 ovarian samples was a suitable starting point for making qualitative assessments in this pilot project. However, the small sample size likely led to error in the quantitative endpoints (i.e., follicle diameter, luteal diameter, AFC) compared among the 3 imaging methods. In addition, it was difficult to determine the precise locations of structures within the ovary when comparing different imaging techniques. Follicles and CL identified with DEI were carefully marked with indelible ink, as a reference point for subsequent ultrasonographic imaging and histologic sectioning. Despite this strategy, small variations in the position of follicles and CL during DEI, ultrasonography and histology imaging may have contributed to error in our study.

DEI is only one phase-sensitive synchrotron imaging technique. Other phase-sensitive techniques for imaging soft tissues include in-line Phase-Contrast Computed Tomography (CT), Talbot grating interferometry, and DEI-CT [28,46,47]. Future research should be conducted to

examine the use of DEI-CT methods for imaging bovine and/or human ovaries. DEI-CT should not result in the overlapping of internal structures associated with planar DEI, and may thereby improve the ability to delineate individual follicles [34,48]. Furthermore, optimization of synchrotron modalities for imaging ovaries may assist in understanding female reproductive pathophysiology (i.e., infertility, ovarian malignancies) and provide a working model for imaging other soft tissues (i.e., prostate, breast).

In summary, Diffraction Enhanced synchrotron techniques used in the present study were inferior for imaging bovine ovaries *ex vivo* compared to conventional 2D ultrasonography. DEI was not an effective tool for detecting antral follicles, CL, or COC within the ovaries. Future research should focus on alternative configurations of DEI and/or different synchrotron imaging techniques for imaging bovine and human ovaries, such as DEI-CT or Phase-Contrast CT. The development of novel high-resolution synchrotron techniques for imaging bovine and human ovaries may provide valuable insight into ovarian physiology such as pre-antral and early antral follicular dynamics as well as follicle-oocyte-interactions.

### 3.6 References


1. **Mihu D. and Nugym C. M.** Ultrasonography of the uterus and ovaries. Medical Ultrasonography. 2011; 13(3): 249 - 252.
2. **Gonzalez-Bulnes A., Pallares P. and Vazquez M. I.** Ultrasonographic imaging in small ruminant reproduction. Reprod Domest Anim. 2010; 45 Suppl 29-20.
3. **Pierson R. A. and Ginther O. J.** Ultrasonic imaging of the ovaries and uterus in cattle. Theriogenology. 1988; 29(1): 21-37.
4. **Hearn-Stebbins B., Jaffe R. and Brown H.** Ultrasonographic evaluation of normal pelvic anatomy. In: R. Jaffe, R. Pierson and J. Abramowicz, eds. *Imaging in Infertility and Reproductive Endocrinology*. Philadelphia: J. B. Lippincott Company; 1994:1-21.
5. **Martin K.** Introduction to B-mode imaging. In: P. Hoskins, K. Martin and A. Thrush, eds. *Diagnostic Ultrasound: Physics and Equipment*. 2nd ed. Cambridge: Cambridge University Press; 2010:1-22.
6. **Pierson R. A., Kastelic J. P. and Ginther O. J.** Basic principles and techniques for transrectal ultrasonography in cattle and horses. Theriogenology. 1988; 29(1): 3-20.
7. **Adams G. and Pierson R.** Bovine model for study of ovarian follicular dynamics in humans. Theriogenology. 1995; 43113-120.
8. **Bomsel-Helmreich O.** Ultrasound and the preovulatory human follicle. Oxf Rev Reprod Biol. 1985; 71-22.
9. **Levi S.** The history of ultrasound in gynecology 1950-1980. Ultrasound Med Biol. 1997; 23(4): 481-552.
10. **Parsons A. K.** Imaging the human corpus luteum. J Ultrasound Med. 2001; 20(8): 811-819.
11. **Saba L., Guerriero S., Sulcis R., Virgilio B., Melis G. and Mallarini G.** Mature and immature ovarian teratomas: CT, US and MR imaging characteristics. Eur J Radiol. 2009; 72(3): 454-463.
12. **Speca S., Summaria V. and Marano P.** Ultrasonography in gynecology: normal anatomy. European Journal of Ultrasound. 1996; 477-89.
13. **Baerwald A., Adams G.P and Pierson R.A.** Characterization of ovarian follicular wave dynamics in women. Biol Reprod. 2003; 691023-1031.
14. **Edmondson A. J., Fissore R. A., Pashen R. L. and Bondurant R. H.** The use of ultrasonography for the study of the bovine reproductive tract. I. Normal and pathological ovarian structures. Anim Reprod Sci. 1986; 12(3): 157-165.
15. **Vassena R., Adams G. P., Mapletoft R. J., Pierson R. A. and Singh J.** Ultrasound image characteristics of ovarian follicles in relation to oocyte competence and follicular status in cattle. Anim Reprod Sci. 2003; 76(1-2): 25-41.
16. **Baerwald A., Dauk S., Kanthan R. and Singh J.** Use of ultrasound biomicroscopy to image human ovaries in vitro. Ultrasound Obstet Gynecol. 2009; 34(2): 201-207.
17. **Zandt-Stastny D., Thorsen M. K., Middleton W. D., Aiman J., Zion A., McAsey M. and Harms L.** Inability of sonography to detect imminent ovulation. AJR Am J Roentgenol. 1989; 152(1): 91-95.
18. **Harris R. A., Follett D. H., Halliwell M. and Wells P. N.** Ultimate limits in ultrasonic imaging resolution. Ultrasound Med Biol. 1991; 17(6): 547-558.
19. **Arfelli F.** Synchrotron light and imaging stystems for medical radiology. Nucl Instrum Meth A. 2000; 45411-25.

20. **Suortti P. and Thomlinson W.** Medical applications of synchrotron radiation. Phys Med Biol. 2003; 48(13): R1-35.
21. **Blattmann H., Gebbers J. O., Bräuer-Krisch E., Bravin A., Le Duc G., Burkard W., Di Michiel M., Djonov V., Slatkin D. N., Stepanek J. and Laissue J. A.** Applications of synchrotron X-rays to radiotherapy. Nucl Instrum Meth A. 2005; 548(1–2): 17-22.
22. **Kocsis M. and Snigirev A.** Imaging using synchrotron radiation. Nucl Instrum Meth A. 2004; 525(1–2): 79-84.
23. **Westneat M. W., Socha J. J. and Lee W. K.** Advances in biological structure, function, and physiology using synchrotron X-ray imaging. Annu Rev Physiol. 2008; 70119-142.
24. **Thomlinson W.** Current status and perspectives of synchrotron radiation in medicine. *V Internatinoal Conference on Applications of Physics in Medicine and Biology*. Trieste, Italy1996:1-9.
25. **Margaritondo G.** Elements of Synchrotron Light for Biology, Chemistry, & Medical Research. Oxford: Oxford University Press; 2002:1-255.
26. **Chapman D., Thomlinson W., Johnston R. E., Washburn D., Pisano E., Gmur N., Zhong Z., Menk R., Arfelli F. and Sayers D.** Diffraction enhanced x-ray imaging. Phys Med Biol. 1997; 42(11): 2015-2025.
27. **Pagot E., Fiedler S., Cloetens P., Bravin A., Coan P., Fezzaa K., Baruchel J., Hartwig J., Von Smitten K., Leidenius M., Karjalainen-Lindsberg M. and Keyrilainen J.** Quantitative comparison between two phase contrast techniques: diffraction enhanced imaging and phase propagation imaging. Phys Med Biol. 2005; 50(4): 709 - 724.
28. **Zhou S.-A. and Brahme A.** Development of phase-contrast X-ray imaging techniques and potential medical applications. Physica Medica. 2008; 24(3): 129-148.
29. **Liu C., Zhang Y., Zhang X., Yang W., Peng W., Shi D., Zhu P., Tian Y. and Huang W.** X-ray diffraction-enhanced imaging of uterine leiomyomas. Med Sci Monit. 2005; 11(5): MT33-38.
30. **Pisano E., Johnston R., Chapman D., Geradts J., Iacocca M., Livasy C., Washburn D., Sayers D., Zhong Z., Kiss M. and Thomlinson W.** Human breast cancer specimens: Diffraction-enhanced imaging with histologic correlation improved conspicuity of lesion detail compared with digital radiography. Radiology. 2000; 214895-901.
31. **Parham C., Zhong Z., Connor D. M., Chapman L. D. and Pisano E. D.** Design and implementation of a compact low-dose diffraction enhanced medical imaging system. Acad Radiol. 2009; 16(8): 911-917.
32. **Li J., Zhong Z., Lidtke R., Kuettner K. E., Peterfy C., Aliyeva E. and Muehleman C.** Radiography of soft tissue of the foot and ankle with diffraction enhanced imaging. J Anat. 2003; 202(5): 463-470.
33. **Faulconer L., Parham C., Connor D., Zhong Z., Kim E., Zeng D., Livasy C., Cole E. B., Kuzmiak C., Koomen M., Pavic D. and Pisano E.** Radiologist evaluation of an x-ray tube-based diffraction-enhanced imaging prototype using full-thickness breast specimens Acad Radiol. 2009; 161329-1337.
34. **Bravin A., Keyrilainen J., Fernandez M., Fiedler S., Nemoz C., Karjalainen-Lindsberg M. L., Tenhunen M., Virkkunen P., Leidenius M., von Smitten K., Sipila P. and Suortti P.** High-resolution CT by diffraction-enhanced x-ray imaging: mapping of breast tissue samples and comparison with their histo-pathology. Phys Med Biol. 2007; 52(8): 2197-2211.

35. **Mollenhauer J., Aurich M. E., Zhong Z., Muehleman C., Cole A. A., Hasnah M., Oltulu O., Kuettner K. E., Margulis A. and Chapman L. D.** Diffraction-enhanced X-ray imaging of articular cartilage. Osteoarthritis and Cartilage. 2002; 10(3): 163-171.
36. **Connor D. M., Zhong Z., Foda H. D., Wiebe S., Parham C. A., Dilmanian F. A., Cole E. B. and Pisano E. D.** Diffraction enhanced imaging of a rat model of gastric acid aspiration pneumonitis. Acad Radiol. 2011; 18(12): 1515-1521.
37. **Hu C., Zhang L., Li H. and Lo S.** Comparison of refraction information extraction methods in diffraction enhanced imaging. Opt Express. 2008; 16(21): 16704-16710.
38. **Christensen C., Singh J. and Adams G.** The use of diffraction enhanced imaging for bovine soft tissue. *Proceedings of the Fifth Annual Users' Meeting and Workshops of the Canadian Light Source*. University of Saskatchewan, Saskatoon2002:26 (Abstract #35).
39. **Adams G. P., Singh J. and Baerwald A. R.** Large animal models for the study of ovarian follicular dynamics in women. Theriogenology. 2012; 78(8): 1733-1748.
40. **Thomlinson W., Suortti P. and Chapman D.** Recent advances in synchrotron radiation medical research. Nucl Instrum Meth A. 2005; 543(1): 288-296.
41. **Krause W. and Cutts J.** The female reproduction system. *Concise Text of Histology*. Baltimore: Williams & Wilkins; 1981:367-371.
42. **Gougeon A.** Human ovarian follicular development: From activation of resting follicles to preovulatory maturation. Ann Endocrinol (Paris). 2010; 71(3): 132-143.
43. **Crisp T.** Organization of the ovarian follicle and events in its biology: oogenesis, ovulation or atresia. Mutation Research/Reviews in Genetic Toxicology. 1992; 296(1-2): 89 - 106.
44. **Ng E., Tang O. and Ho P.** The significance of the number of antral follicles prior to stimulation in predicting ovarian responses in an IVF programme. Hum Reprod. 2000; 151937 -1942.
45. **Gibreel A., Maheshwari A., Bhattacharya S. and Johnson N.** Ultrasound tests of ovarian reserve; a systematic review of accuracy in predicting fertility outcomes. Hum Fertil (Camb). 2009; 1295 - 106.
46. **Fitzgerald R.** Phase-sensitive X-ray imaging. Physics Today. 2000; 53(7): 23-28.
47. **Pinzer B., Cacquevel M., Modregger P., McDonald S., Bensadoun J., Thuering T., Aebischer P. and Stampanoni M.** Imaging brain amyloid deposition using grating-based differential phase contrast tomography. NeuroImage. 2012; 611336 - 1346.
48. **Yuasa T., Hashimoto E., Maksimenko A., Sugiyama H., Arai Y., Shimao D., Ichihara S. and Ando M.** Highly sensitive detection of the soft tissues based on refraction contrast by in-plane diffraction-enhanced imaging CT. Nucl Instrum Meth A. 2008; 591(3): 546-557.

# Chapter 4

## Synchrotron Imaging of Bovine and Human Ovaries *Ex Vivo:* Propagation-based and Talbot Grating Interferometry Computed Tomography Techniques

Upekha Basnayaka MSc[1], Dean Chapman PhD[2], Gregg Adams DVM PhD[3], Tomasz Wysokinski PhD[4], George Belev PhD[4], Rani Kanthan MBBS MS FRCS FRCPSC FCAP MEd[5], Rajni Chibbar MD PhD FRCPC[5], Robert Lewis PhD[6], Naoto Yagi PhD[7], Kentaro Uesugi PhD[7], Masato Hoshino PhD[7], Angela Baerwald, PhD[1]

[1]Department of Obstetrics, Gynecology & Reproductive Sciences, College of Medicine, University of Saskatchewan, Saskatchewan, Canada

[2]Department of Anatomy & Cell Biology, College of Medicine, University of Saskatchewan, Saskatchewan, Canada

[3]Department of Veterinary Biomedical Sciences, Western College of Veterinary Medicine, University of Saskatchewan, Saskatchewan, Canada

[4]Canadian Light Source, Saskatchewan, Canada

[5]Department of Pathology & Laboratory Medicine, College of Medicine, University of Saskatchewan, Saskatchewan, Canada

[6]Office of the Vice President of Research, University of Saskatchewan, Saskatoon

[7]Japan Synchrotron Radiation Research Institute, SPring-8/JASRI, 1 Hyogo Prefecture, Japan.

## 4.0 Preface

The following study (Chapter 4) was conducted to investigate two phase-contrast based synchrotron techniques, Propagation-based Computed Tomography (PB-CT) and Talbot Grating Interferometry (TGI-CT), for imaging bovine and human ovaries. Synchrotron-based PB-CT and TGI-CT of bovine and human ovaries have not been previously investigated.

This manuscript will be submitted for publication in Academic Radiology. The contributions of the primary author (Upekha Basnayaka) to this manuscript include the following: 10% study design, 50% data collection, 65% data analyses/interpretation, 45% manuscript preparation and 80% presentation of study findings. The co-authors are acknowledged for contributing to study design, data collection and revising the manuscript.

The authors would like to thank Dr. David Cooper (Anatomy and Cell Biology, University of Saskatchewan) as well as Adam Webb, Nazanin Samadi, and Zhouping Wei (Canadian Light Source) for their assistance with image reconstruction and optimization. We would also like to acknowledge Dr. Jaswant Singh (Veterinary Biomedical Sciences, University of Saskatchewan) for his assistance with study design and data collection. Sincere thanks are extended to the research participants, whose involvement was essential for the completion of this study. The authors would also like to thank the surgical, nursing, and Pathology staff at Saskatoon City Hospital and Royal University Hospital for assisting with sample collection.

This research was conducted at the Canadian Light Source (CLS, Saskatoon, SK) which is supported by the Natural Sciences and Engineering Research Council of Canada, National Research Council Canada, Canadian Institutes of Health Research (CIHR), Government of Saskatchewan, Western Economic Diversification Canada, and the University of Saskatchewan. The experiment at SPring-8 was performed with an approval of the Japan Synchrotron Radiation Research Institute (2012B1353). Operational funding for this study was provided by a CIHR-Training Grant in Health Research Using Synchrotron Techniques and the College of Medicine at the University of Saskatchewan.

## 4.1 Abstract

**Objective:** To test the hypothesis that Propagation-Based Computed Tomography (PB-CT) and Talbot Grating Interferometry Computed Tomography (TGI-CT) synchrotron techniques would provide greater contrast for imaging ovarian anatomy compared to conventional 2D ultrasonography.

**Materials and Methods:** A prospective, observational study was conducted at the Canadian Light Source to qualitatively and quantitatively compare ovarian imaging using PB-CT, ultrasonography, and histology. Bovine ovaries were imaged as follows: fresh without contrast (n=1); fresh with iodine-based contrast (n=2); and formalin-fixed with contrast (n=1). Human ovaries were imaged without contrast as fresh (n=2) and preserved (n=2) samples. The feasibility of TGI-CT to image preserved bovine (n=1) and human (n=1) ovaries was further evaluated at SPring-8, Japan.

**Results:** 100% of antral follicles ≥2mm and 100% of corpora lutea (CL) detected with ultrasonography were identified with PB-CT. Mean follicle and luteal diameter did not differ between PB-CT, ultrasonography and histology ($P>0.05$). The smallest follicle detected was superior with PB-CT (0.9±0.4mm) compared to ultrasonography (2.2±0.2 mm, $P<0.05$). PB-CT, but not ultrasonography, allowed the detection of the cell layers comprising the follicle wall ($P<0.05$). TGI-CT provided greater contrast for evaluating follicles, CL and vasculature compared to PB-CT and ultrasonography. High contrast spherical structures resembling cumulus oocyte complexes (COC) were detected with both PB-CT and TGI-CT, but not ultrasonography.

**Discussions:** PB-CT was as effective as ultrasonography for measuring follicle and luteal diameter. However, PB-CT was superior to ultrasonography for visualizing ovarian microanatomy, including follicles <2mm, cell layers of the follicle wall, and COC. TG-CT appears to provide the greatest resolution for imaging ovarian anatomy compared to both ultrasonography and PB-CT.



**Keywords:**
Ovary – Human – Bovine – Synchrotron – Propagation-based Imaging – Grating Interferometry

## 4.2 Introduction

Non-invasive imaging technologies are essential for understanding the structural and functional properties of biological tissues. Currently, the most commonly used method for evaluating human reproductive tissues is ultrasonography because it is non-invasive, safe, and portable [1-3]. Ultrasonographic images are comprised of 2D pixels or 3D voxels. Each pixel or voxel displays a varying degree of brightness that corresponds to the amplitude of the echo created as a sound wave is reflected from within a tissue[4, 5]. Obstetrical and gynecologic applications of ultrasonography include, but are not limited to, monitoring ovarian and uterine function during the menstrual cycle (i.e., follicular, luteal, and endometrial development; ovulation), assessment of embryonic, fetal, and placental development, as well as the diagnosis and treatment of infertility and pregnancy disorders [5-12].

Ultrasonography has profoundly improved our ability to monitor reproductive function and early development *in vivo*. However, the detection of ovarian structures <2 mm in size, such as early developing follicles, cell layers of the follicle wall, and oocytes is not currently possible using conventional 2-dimensional ultrasonography [13, 14]. In addition, the resolution of ultrasonographic imaging is restricted by penetration depth [6, 15], as well as artifacts caused by intestinal activity and gas [6, 15, 16]. The development of novel high-resolution imaging technologies may provide a means to increase our understanding of the biologic mechanisms underlying human ovarian function (i.e., follicle development, oogenesis, ovulation and luteogenesis) and female reproductive pathophysiology.

Synchrotron radiation has been used to image normal and pathological states of biological tissues. Synchrotron imaging involves the acceleration of electrons to create a high-energy light beam. Synchrotron imaging can be conducted with a lower radiation exposure compared to conventional X-ray methods due to the selection of a photon beam with a narrow energy range [17-23].

Phase contrast synchrotron imaging utilizes both the refraction and absorption properties of objects to provide images of greater contrast resolution compared to conventional X-ray imaging [24, 25]. As the synchrotron beam traverses an object, the X-rays are refracted and absorbed. The amount of refraction and absorption depends upon the properties of objects, such as thickness and density [24-27]. Contrast, produced the differences in tissue properties, is detected and projected onto the image. Phase contrast imaging is about 1000 times more

powerful for detecting subtle density changes in soft tissues compared to conventional radiography [17, 27-32].

There are three different synchrotron applications that utilize phase-contrast techniques: 1) Diffraction Enhanced Imaging (DEI), 2) Propagation-based imaging (PBI), and 3) Talbot Grating Interferometry (TGI). With each technique, the sample is placed in-line with the incoming X-ray beam. The X-rays that pass through the sample are captured by a detector which converts the X-rays into visible light [30]. The phase contrast techniques above can be combined with Computed Tomography (CT) by rotating the sample and obtaining 2D slices for each projection [33, 34].

In *DEI,* a crystal (known as an analyzer) is placed between the sample and the detector [35]. The incident X-ray beam passes through the sample and refracts onto the analyzer crystal [27]. Only the X-rays that are selectively accepted by the crystal will be diffracted onto the detector [36]. Information regarding the refraction, absorption and scatter rejection of X-rays from a sample can be obtained with DEI [36, 37]. DEI provides high sensitivity for visualizing microcalcifications and subtle distortions in human breast tissue compared to conventional mammography. DEI has been shown to enable the detection of bovine ovarian follicles and corpora lutea (CL) [38] , albeit at a lesser resolution than conventional ultrasonography [35].

With *PBI,* the distance between the sample and detector is increased so that the transmitted X-rays travel further and produce phase distortions [27, 39]. The phase distortions create strong interference patterns between refracted X-rays of the sample and unrefracted X-rays of the background [26, 31]. The interference patterns produce an ‘edge-enhancement effect’ at sample boundaries, which improves the overall image quality [26, 31, 40]. PBI techniques have been used to examine mouse and rabbit lungs [25] as well as the human kidney and prostate [41]. *TGI* imaging uses two crystals to measure the refraction-induced lateral displacement caused by wave interference [39, 42]. The first crystal (i.e., phase grating) is placed behind the sample to create X-ray interference and the second crystal (i.e., absorption grating) is placed between the first crystal and the detector to transform the interference fringes into an intensity signal [43]. TGI imaging is useful for weakly-absorbing soft tissues. However, it is more difficult to implement than other phase-contrast techniques [18]. TGI studies have previously been conducted using the mouse heart [43], knee joint[44], and brain [44, 45]. However, no data have been published on the use of either PB-CT or TGI imaging for imaging ovaries.

The objective of this study was to determine the effectiveness of PB-CT and TGI-CT for imaging bovine and human ovaries. We hypothesized that PB-CT and TGI-CT would provide greater contrast resolution for imaging ovarian structures (i.e., antral follicles, cumulus oocyte complexes (COC), CL) compared to conventional 2D ultrasonography.

## 4.3 Materials and Methods

A prospective, observational pilot study was conducted from 2011 – 2013. Ethical approval for conducting this study was obtained from the Animal Care Committee and the Biomedical Research Ethics Board at the University of Saskatchewan as well as the Strategic Health Information and Planning Services Unit of the Saskatoon Health Region. Research procedures were conducted in accordance with the Tri-Council Policy Statement on the Ethical Conduct for Research Involving Humans, and the Canadian Council on Animal Care. All human participants provided informed consent before initiating study procedures.

### 4.3.1 Imaging Techniques

A. Propagation-Based CT Imaging

*(i) Sample Collection, Set Up and Design*

Phase 1: Fresh bovine ovaries (n=4) were obtained from local abattoirs. The ovarian artery was flushed with saline within 30 minutes of removal. Samples were imaged in the following conditions:

1. fresh without contrast (n=1);
2. fresh with injection of 5-8mL of iodine-based contrast agent (Ioversol, Optiray$^{TM}$240) into the ovary artery (n=2); and,
3. preserved in 10% Formalin with ovarian artery contrast, as described above (n=1).

Phase 2: Formalin-fixed human ovarian tissue sections (n=2) were obtained from the Department of Pathology at Royal University Hospital.

Phase 3: Unfixed fresh ovaries (n=2) were obtained in the operating room from women undergoing laparoscopic bilateral oophorectomies at the Saskatoon City Hospital (mean age = 50.5 years; range= 49-52 years). Indications for oophorectomy were as prophylaxis against breast and ovarian cancer.

For phases 1-3, ovaries were transported in saline at room temperature to the CLS for imaging. PB-CT imaging was conducted on all samples at the BioMedical Imaging and Therapy (05B1-1) beamline (BMIT) at the CLS. Ovaries were placed in a plastic cylindrical container and filled with fresh room temperature saline in preparation for synchrotron imaging. Air bubbles were manually removed from the container prior to imaging. A detector (Hamamatsu, manufacturer, location) with a charge-coupled device camera (Model, C9300-124, Manufacturer, location) was placed 125 cm from the sample. The source was located at a distance of 27m from the sample. A total of 1800 projections with a pixel resolution of 18.8 µm were taken per slice. The imaging time for a 5 mm-slice of the ovary took approximately 1.5 hours.

*(ii) Image Reconstruction*

Tomographic PB-CT images were reconstructed using SyrmepTomoProject (Version 2.0, Elettra Synchrotron Facility, Trieste, Italy). File conversions and editing of images were conducted using ImageJ 1.6.0_20 (National Institutes of Health, USA), HCImage (Version 2.0.1.2, Hamamatsu Corporation) and Avizo Standard (Edition 7.0.1, Visualization Sciences Group). Ring artifacts observed in images were removed using a customized software program [46-50].

B. Talbot Grating Interferometry-CT Imaging

*(i) Sample Collection, Set Up and Design*

TGI-CT imaging was conducted at the SPring-8 synchrotron facility (BL20B2 beamline) in Japan. A preserved bovine ovary (n=1) and a preserved human ovarian tissue section (n=1) were imaged. All ovarian samples were embedded in agarose gel and imaged with an X-ray energy of 25 keV and a pixel resolution of 13.3 µm. Images were obtained with an AA60 (P43 t20um, f=105mm lens) detector with an ORCA_Flash4.0 (f=50mm lens) camera. The total scanning times for the samples were approximately 2.3 hours (whole ovary) and 1.2 hours (tissue section). The CT scan was conducted using 900 projections over 180°. A total of 5 images were obtained by shifting the absorption grating. Specific ovarian regions of interest identified during PB-CT were marked with indelible ink.

*(ii) Image Reconstruction*

Final reconstruction of the TGI-CT images was conducted using a customized software program (Kentaro Uesugi & Masato Hoshino, SPring-8, Japan).

C. Ultrasonographic Imaging

Following synchrotron imaging, all ovaries imaged with PB-CT and TGI-CT were further imaged with 2D ultrasonography using a portable ultrasonographic system (8 MHz curvilinear probe; MyLab$^{TM}$Five, Esaote). Ovaries were imaged in the transverse plane in a saline bath with the following configurations: depth of 6 cm; overall gain of 52%; and, a single focal zone at a depth of 3 cm. Ultrasonography images were evaluated using Sante DICOM Editor (Version 3.1.23, Athens, Greece) and ImageJ 1.6.0_20 (National Institutes of Health, USA). All fresh and human bovine samples were placed in 10% Formalin following synchrotron and ultrasonographic imaging.

D. Histologic Imaging

Upon completion of the synchrotron and ultrasonographic imaging, ovaries were histologically sectioned and imaged. The specific areas of interest in the ovary marked with indelible ink were cut in 3mm slices and histologically processed into paraffin blocks. The blocks were then serially sectioned at 5µm thickness using a microtome and every 4$^{th}$ section was selected for hematoxylin and eosin staining. Digital images of the histological slides were obtained using a digital camera (Nikon D90). Histology images were edited using ViewNX$^{TM}$ (Version 2.3.0). Bovine ovaries were histologically imaged at Veterinary Biomedical Sciences, Western College of Veterinary Medicine, University of Saskatchewan. Histological gross sectioning of the human tissues was conducted in the Departments of Pathology at Royal University Hospital and Saskatoon City Hospital. Microsectioning and staining of the human ovarian samples for histological evaluation was conducted after standard clinical pathological evaluations.

### 4.3.2 Qualitative Evaluations:

Qualitative evaluations were made for all samples imaged sequentially with PB-CT, TGI-CT, ultrasonography and histology. The ability to detect ovarian structures of interest (i.e., follicles, CL, COC) using each of the 3 imaging techniques was tabulated and compared.

Ovarian follicles imaged with histology were labeled as either normal or atretic, based on histologic evaluation [51-53].

### 4.3.3 Quantitative Evaluations:

Quantitative analyses were conducted for PB-CT and corresponding ultrasonography and histologic images. The mean diameter of all antral follicles ≥ 2mm and all CL was calculated as the average of the length and width obtained using the widest follicular/luteal dimension in the transverse plane. The thickness of the follicle wall was measured in replicates at the 2, 4, 8 and 10 o'clock positions and then averaged. The smallest follicle detected was reported for each of the three imaging techniques [54]. The orientation and magnification of images was standardized for each technique. All images were scaled according to their pixel dimensions using ImageJ (Version 1.46, National Institutes of Health, Bethesda, MA, USA). Ultrasound images were magnified 3X for follicle and CL diameter measurements, and 4X for measuring follicle wall thickness. Images obtained with PB-CT were magnified 1.75X for follicle and CL diameter and 2.5X for follicle wall thickness. Histologic images were magnified 2.5X for follicle diameter and wall thickness, and 1.25X for CL diameter. Mean follicle diameter, mean luteal diameter, and the smallest antral follicle detected were compared among PB-CT, ultrasonography, and histology using One-Way ANOVA with Tukey's post hoc tests (SPSS Version 20.0, Chicago, IL, USA).

## 4.4 Results

### 4.4.1 Propagation-Based Computed Tomography

*Qualitative Assessments:*

Correspondent images of gross morphology, ultrasonography, PB-CT and histology of ovarian samples are shown in Fig. 4.1 (a-h). A fresh bovine ovary with contrast (Fig. 4.1 a, c, e, g) and a Formalin-fixed human ovarian tissue section without contrast (Fig. 4.1b, d, f, h) are shown. Ring-artifacts were observed as dark and bright concentric circles in the reconstructed PB-CT images (Fig. 4.1 e, f). The injection of contrast enabled the visualization of ovarian vasculature in one bovine ovary, as shown in Figure 4.2 (a, b).

In Fig. 4.1 (c, d), antral follicles were identified ultrasonographically as dark, anechoic, circular structures with a poorly-defined follicular wall. By comparison, antral follicles in the

PB-CT images were visualized as low contrast circular structures with a more clearly-visualized wall (Fig. 4.1 e, f). All antral follicles ≥ 2mm detected with ultrasonography were detected with PB-CT. The granulosa and theca cell layers comprising the follicular wall were detected 100% of the time (both bovine and human samples) with PB-CT, but only 88% (bovine) and 78% (human) of the time using ultrasonography, when compared to histology (Fig. 4.1 c, e, g).

The developing CL was visualized ultrasonographically as an irregularly-circumscribed structure of mixed echotexture with (Fig. 4.1 d) or without (not shown) a hypo-echogenic blood-filled cavity. Regressing CL, known as corpora albicantia (CA) exhibited greater ultrasonographic echogenicity compared to the surrounding stroma (Fig.4.1 d). CL detected with ultrasonography were also visualized with PB-CT in 100% of cases. In the PB-CT image, the central cystic cavity of CL exhibited greater contrast resolution compared to the luteal wall (Fig. 4.1 f). Therefore, cystic CL was better detected in the PB-CT and histologic images (Fig. 4.1 f, h) compared to ultrasonography (Fig. 4.1a, d). Connective tissues of the CA and CL in the PB-CT images exhibited lower contrast compared to nearby follicles (Fig. 4.1 f).

Preservation of the ovaries caused slight shrinkage of the tissues. However, no noticeable differences in image quality were observed between the fresh and preserved ovaries.

*Quantitative Assessments:*

No differences were observed in mean follicle diameter and follicle wall measurements between normal versus atretic follicles ($P>0.05$). Therefore, quantitative data were combined for normal and atretic follicles. Mean follicle diameter, CL diameter, and follicle wall thickness were calculated separately for fresh and preserved ovaries.

Mean follicle and luteal diameter measurements in bovine and human ovaries were not different among the PB-CT, ultrasonography and histologic images (Table 4.1, $P>0.05$). PB-CT was more sensitive for detecting small antral follicles in bovine, but not human ovaries, compared to ultrasonography (Table 4.2, $P = 0.04$). One of the bovine ovaries was excluded from the calculation of smallest follicle due to inadequate number of histological slices. Mean follicle wall thickness in bovine and human ovaries using both PB-CT and histology was smaller compared to ultrasonography (Table 4.3, $P<0.0001$).

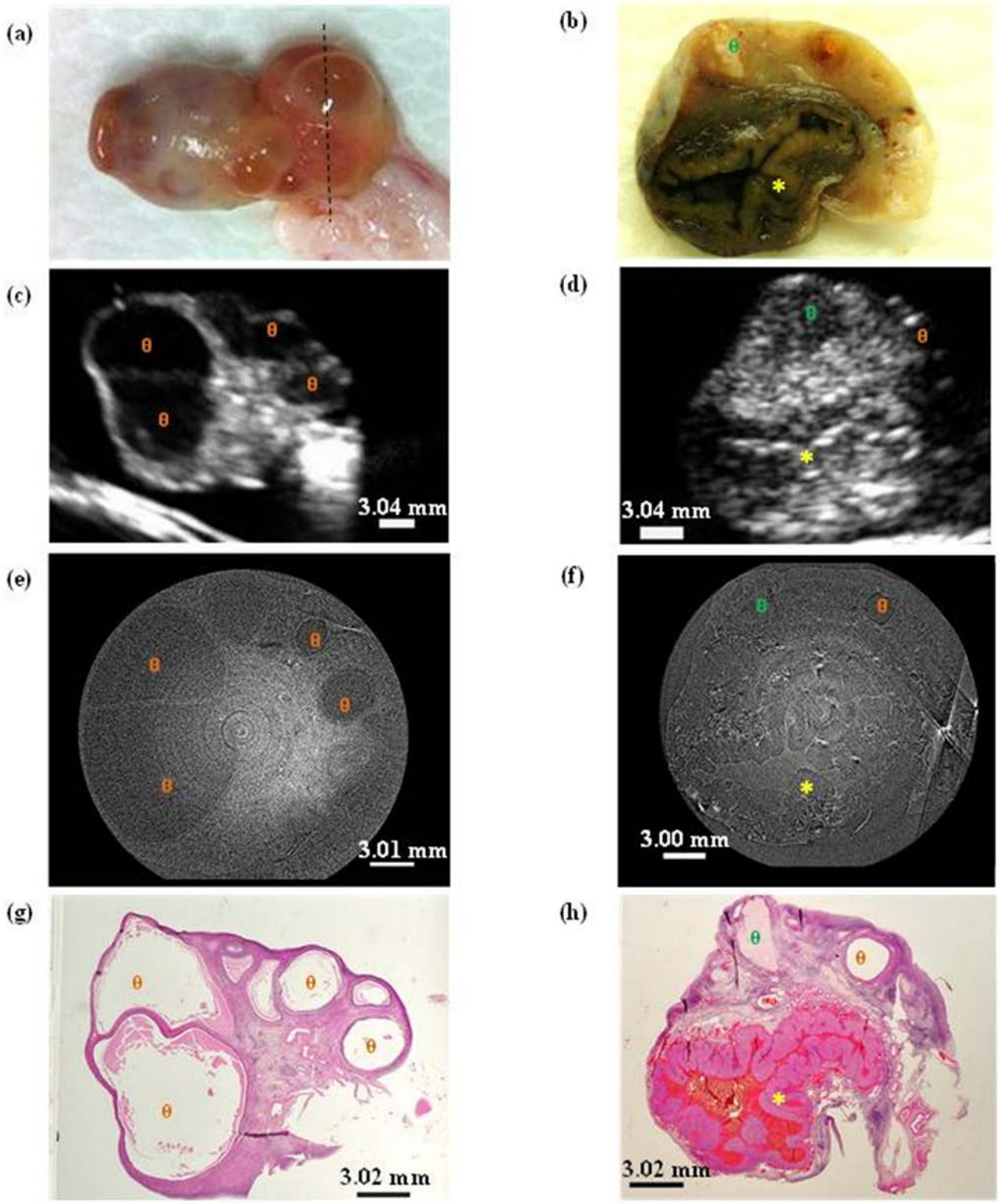


**Figure 4.1** Correspondent images of a fresh bovine ovary with contrast (a, c, e, g) and a Formalin-fixed human ovarian tissue segment without contrast (b, d, f, h). Gross morphology (a, b), ultrasonography (c, d), PB-CT at 18.8 µm resolution (e, f), and histological (g, h) images are displayed. Examples of follicles (orange θ), corpora lutea (yellow *), and corpora albicantia (green θ) are indicated. A dashed line on the gross image (a) indicates the plane of sectioning.

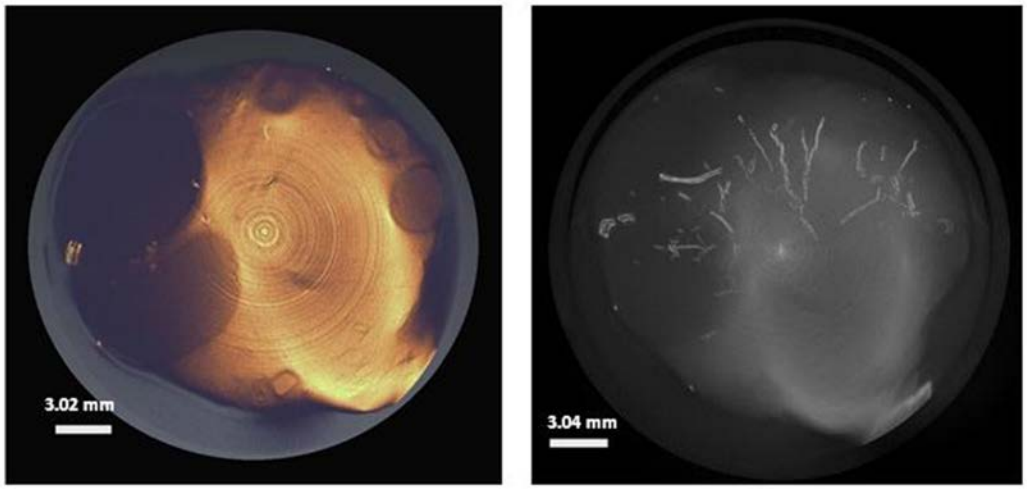


**Figure 4.2** Images of a fresh bovine ovary with contrast obtained with PB-CT at 18.8 µm resolution. A 3D reconstructed image of a bovine ovary section (a) and its maximum intensity projection image with the outline of the ovarian vasculature (b) are shown.

**Table 4.1** Diameter (Mean ± Standard Error) of follicles and corpora lutea in bovine and human ovaries (n = number of follicles or corpora lutea)

| Sample Condition | n | PB-CT (mm) | Ultrasonography (mm) | Histology (mm) | P-value |
|---|---|---|---|---|---|
| *Bovine Ovaries: Follicle Diameter* | | | | | |
| Preserved- with contrast | 11 | 4.2 ± 0.8 | 4.7 ± 0.8 | 3.8 ± 0.7 | 0.72 |
| Fresh - with contrast | 19 | 4.7 ± 0.7 | 5.3 ± 0.6 | 4.0 ± 0.6 | 0.33 |
| Fresh - no contrast | 1 | 4.6 | 5.6 | 5.0 | - |
| *Human Ovaries: Follicle Diameter* | | | | | |
| Preserved- no contrast | 5 | 4.6 ± 0.5 | 4.0 ± 0.43 | 3.7 ± 0.4 | 0.38 |
| Fresh - no contrast | 4 | 6.1 ± 2.5 | 5.0 ± 1.8 | 4.6 ± 1.6 | 0.79 |
| *Human Ovaries: Luteal Diameter* | | | | | |
| Preserved - no contrast | 2 | 8.9 ± 5.4 | 8.1 ± 3.8 | 7.0 ± 3.9 | 0.65 |
| Fresh - no contrast | 2 | 3.4 ± 0.5 | 4.5 ± 0.3 | 3.6 ± 0.3 | 0.16 |

Mean bovine luteal diameter was not calculated, due to an insufficient number of CL detected in the bovine ovaries.

**Table 4.2** Diameter (Mean ± Standard Error) of the smallest follicle detected in bovine and human ovaries

| Sample Condition | n | PB-CT (mm) | Ultrasonography (mm) | Histology (mm) | P-value |
|---|---|---|---|---|---|
| Bovine ovaries | 3 | $0.9 \pm 0.4^{a}$ | $2.2 \pm 0.2^{b}$ | $0.2 \pm 0.1^{a}$ | **0.04** |
| Human ovaries | 4 | $1.2 \pm 0.7^{a}$ | $2.7 \pm 0.4^{a}$ | $0.9 \pm 0.6^{a}$ | 0.11 |

[a, b] Within sample types, values with different superscripts are different ($P < 0.05$)
n= number of ovaries

**Table 4.3** Follicle wall thickness (Mean ± Standard Error) in bovine and human ovaries

| Sample Condition | n | PB-CT (mm) | Ultrasonography (mm) | Histology (mm) | P-value |
|---|---|---|---|---|---|
| *Bovine Ovaries* | | | | | |
| Preserved- with contrast | 10 | $0.15 \pm 0.01^{a}$ | $0.31 \pm 0.01^{b}$ | $0.15 \pm 0.01^{a}$ | **<0.0001** |
| Fresh - with contrast | 17 | $0.16 \pm 0.01^{a}$ | $0.27 \pm 0.01^{b}$ | $0.14 \pm 0.01^{a}$ | **<0.0001** |
| Fresh - no contrast | 1 | 0.31 | 0.14 | 0.14 | - |
| *Human Ovaries* | | | | | |
| Preserved- no contrast | 5 | $0.16 \pm 0.01^{a}$ | $0.28 \pm 0.02^{b}$ | $0.10 \pm 0.01^{a}$ | **<0.0001** |
| Fresh - no contrast | 2 | $0.17 \pm 0.02^{a}$ | $0.30 \pm 0.03^{ab}$ | $0.12 \pm 0.01^{a}$ | 0.10 |

[a, b] Within sample types, values with different superscripts are different ($P < 0.05$)
n = number of follicles

### 4.4.2 Talbot Grating Interferometry Computed Tomography

*Qualitative Assessments:*

Gross morphology, ultrasonography, PB-CT, and TGI-CT images of a bovine (Fig.4.3 a, c, e, g) and human ovarian tissue segment (Fig.4.3 b, d, f, h) were compared. The follicle antrum and the theca and granulosa cell layers comprising the follicle wall were visualized with PB-CT (Fig. 4.3 e) and TGI-CT (Fig.4.3 g) but not ultrasonography (Fig. 4.3 c). Irregular and invaginated walls of the CL were better distinguished with TGI-CT (Fig. 4.3 g, h),compared to PB-CT (Fig. 4.3 e, f) and ultrasonography (Fig. 4.3 c, d). Furthermore, ovarian vasculature was detected with PB-CT (Fig. 4.3 e, f) and TGI-CT (Fig, 4.3 g, h), but not ultrasonography (Fig, 4.3 c, d).

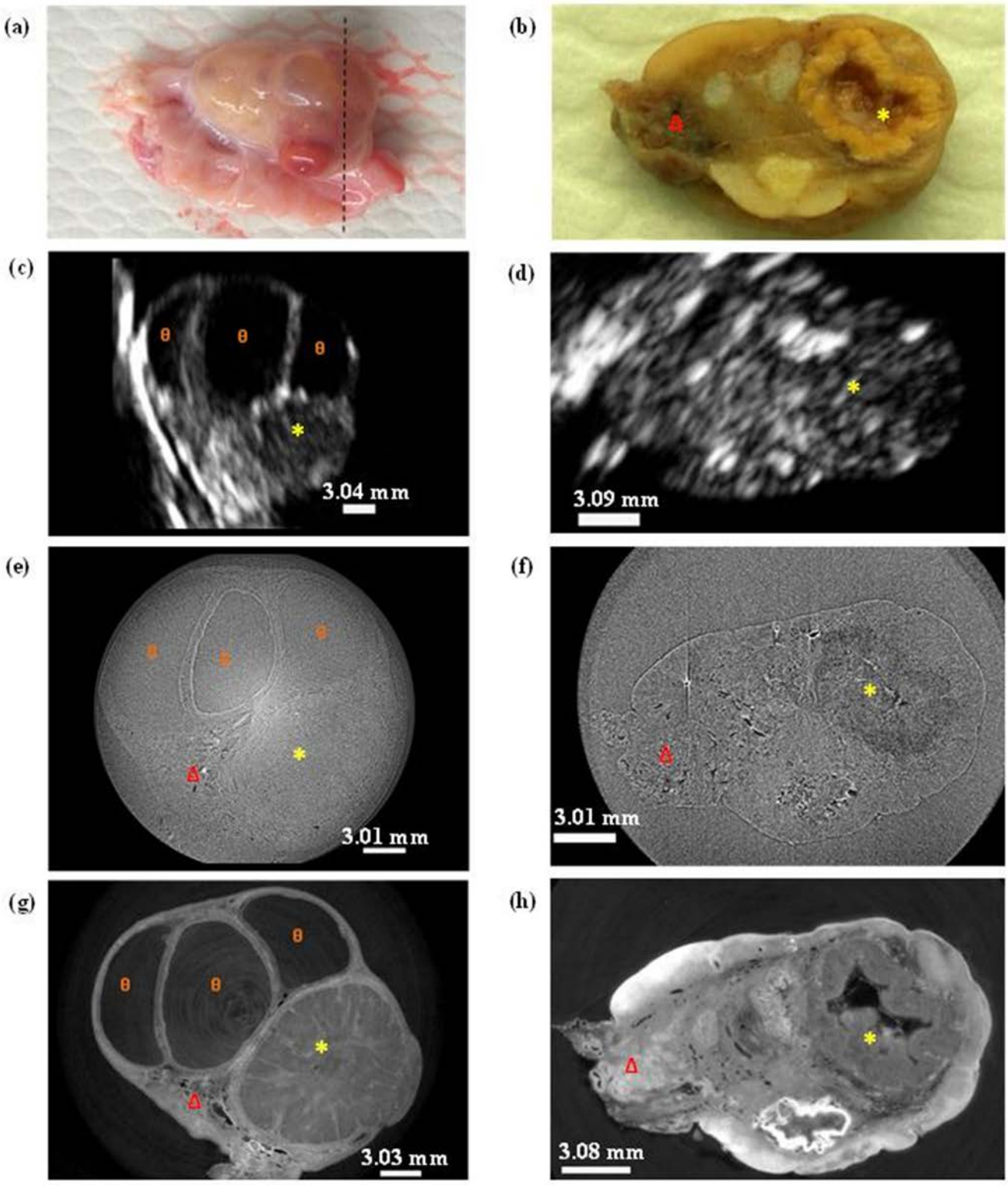


**Figure 4.3** Correspondent images of a preserved bovine ovary (a, c, e, g) and a Formalin-fixed human ovarian tissue segment (b, d, f, h). Gross (a, b), ultrasonographic (c, d), PB-CT at 18.8 µm resolution (e, f), and TGI-CT at 13.3 µm resolution (g, h) images are shown. Ovarian (orange θ), corpora lutea (yellow *), and vasculature (red Δ) are indicated. A dashed line on the gross image (a) indicates the plane of sectioning.

High contrast spherical structures <0.60 mm, protruding into the antrum from the follicle wall were identified bovine ovaries using PB-CT (9 follicles, 3 ovaries) and TGI-CT (7 follicles, 1 ovary) imaging. These location, size, and shape of these protrusions are consistent with COC; however, these structures were not observed in the limited number of histologic sections obtained. An example of one COC identified using both PB-CT and TGI-CT imaging is shown in Fig. 4.4 (a, b).

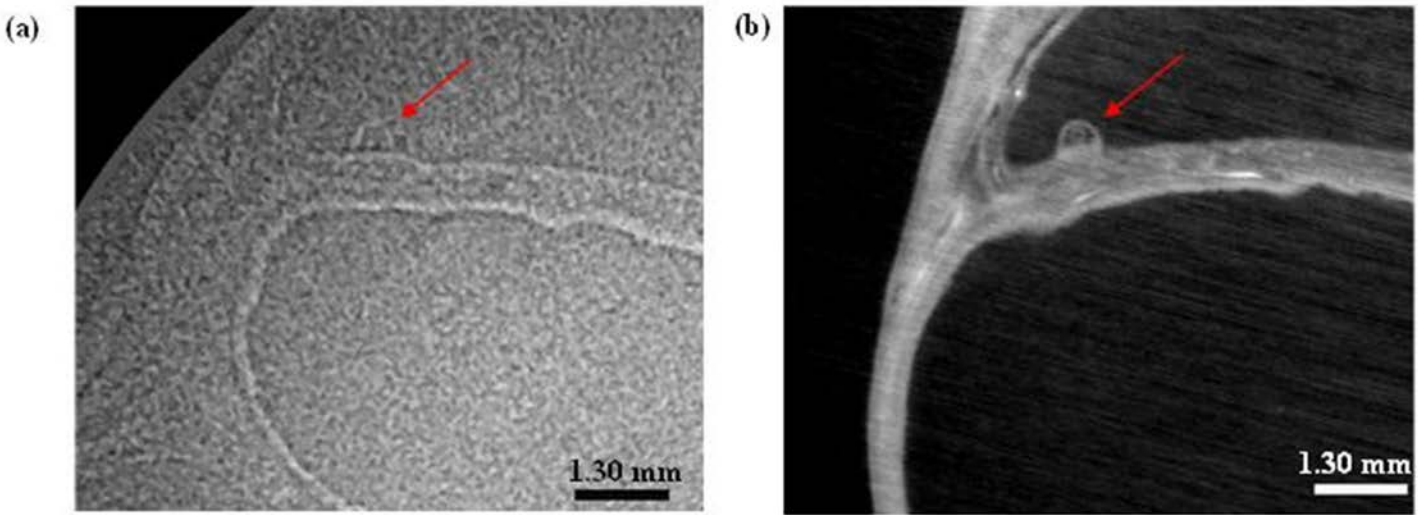


**Figure 4.4** PB-CT (a) and TGI-CT (b) images of the same bovine ovary without contrast. Red arrows indicate cumulus-oocyte-complexes, the oocyte surrounded by cumulus cells.

## 4.5 Discussion

In this pilot study, we examined the effectiveness of PB-CT and TGI-CT synchrotron techniques for imaging bovine and human ovaries *ex vivo*. Overall, we concluded that TGI-CT provided greater contrast resolution for visualizing ovarian anatomy compared to conventional 2D ultrasonography. PB-CT was superior to ultrasonography for detecting small antral follicles <2mm, cell layers of the follicle wall and COC, and equivalent to ultrasonography for measuring follicle and luteal diameters. However, PB-CT was inferior to ultrasonography for visualizing non-cystic CL. We obtained preliminary data to demonstrate that TGI-CT provided the greatest contrast for visualizing ovarian microanatomy compared to both PB-CT and ultrasonography. Thus, our hypotheses were only partially supported.

The follicle is considered the structural and functional unit of an ovary. As such, the ability to evaluate follicular morphology is crucial for our understanding of normal and abnormal female reproductive function. PB-CT imaging was as effective as ultrasonography for measuring antral follicles ≥2 mm in bovine and human ovaries. However, the detection of small antral follicles <2 mm with PB-CT was superior compared to ultrasonography. The detection of small antral follicles has the potential to enhance our knowledge about early follicular development [53, 55, 56]. Bovine and human follicle wall thickness measurements were more accurate with PB-CT versus ultrasonography when both methods were compared with histology. Furthermore, the granulosa and theca layers of the follicle wall could be distinguished on the PB-CT, but not ultrasonographic, images. Ultrasonographic biomicroscopy of human ovaries *ex vivo* has previously been found to be effective for detecting antral follicles <2 mm and the layers of the follicular wall, but was limited in measuring follicles > 7mm [54]. TGI-CT provided more contrast resolution than PB-CT and ultrasonography for delineating antral follicles from the surrounding stromal tissues. TGI-CT appears to be more promising for measuring antral follicles of all sizes and the follicle wall compared to PB-CT, but quantitative comparisons are required to verify these preliminary findings.

We were able to visualize spherical structures within the follicular antrum using PB-CT. We postulated that the spherical structures detected using the synchrotron were COC due to their size, location and similarity in attributes to COC visualized in the previous ultrasound biomicroscopy study in humans [54] and domestic farm animals [55]. Furthermore, circular structures consistent with oocytes within the COC were identified in the TGI-CT images, but not the corresponding PB-CT and ultrasonographic images. We were not able to visualize COC in the human ovaries because of a low follicle count. Lower follicle counts were primarily attributed to the older age of participants in our study. Additional factors which may have influenced follicle counts include genetics, environmental contaminants, and smoking [57]. Further studies should be conducted with an emphasis on visualizing human COC using PB-CT and TGI-CT, preferably with samples from women of reproductive-age (i.e., 18 – 30 years). Synchrotron-based Fourier transform-infrared (FT-IR) microspectroscopy has been used to effectively evaluate the composition, biochemistry and distribution of biological components (i.e., lipid depositions) in mouse oocytes *ex vivo* [56]. Furthermore, synchrotron-based X-ray fluorescence microscopy has been used to evaluate elemental mapping on frog oocytes and

embryos *ex vivo* [58]. The findings from our study provide rationale for evaluating the microanatomy and chemical composition of human oocytes using synchrotron techniques. Currently, the visualization of the oocyte in women *in vivo* is not possible. The ability to visualize the oocyte *in vivo* would be a tremendous advancement to understanding oocyte development, and female reproductive potential [59].

Accurate identification of the CL is imperative for the assessment of ovulation and luteal function in women undergoing fertility investigations and/or assisted reproduction [12, 60]. PB-CT was also as effective as ultrasonography for measuring luteal diameter. However, the contrast resolution for detecting and differentiating follicles from no-cystic CL was inferior with PB-CT. Neither PB-CT nor ultrasonography was capable of detecting all CL that were visualized histologically. The invaginations of the luteal wall in cystic CL were better visualized with PB-CT than ultrasonography. TGI-CT provided greater contrast for visualizing CL with and without a central cystic cavity compared to PB-CT. Therefore, we concluded that TGI-CT was a more promising tool for visualizing the CL compared to PB-CT.

Follicle and luteal vasculature was also better visualized using TGI-CT versus PB-CT and ultrasonography. Thus, the microscopic details visualized in the TGI-CT images of the ovaries appeared to better resemble histology than PB-CT. The multiple scans obtained with CT synchrotron techniques enabled us to evaluate the ovary in serial cross sections and track the appearance of follicles within. Therefore, PB-CT and TGI-CT techniques were more suitable for identifying individual follicles than single projection images obtained previously using planar DEI (Chapter 3) [35]. Our study findings can also be used to determine and predict suitable parameters for synchrotron imaging for other types of soft tissues, such as the prostate and breast. Similarities in the capabilities of synchrotron methods for imaging both bovine and human ovaries further supports the idea that the bovine species is an appropriate model for studying human ovarian structure and function [10, 61].

One of the biggest limitation of this study was the time required for imaging the ovaries using synchrotron techniques. The total length of time required for sample set-up, beamline preparation, and imaging of a whole ovary (dimensions of approximately 3 x 2 x 1.5 cm) was about 8 hours. Therefore, imaging time limited the number of ovaries we could evaluate. Furthermore, we were not able to confirm the detection of COC in the synchrotron images histologically, because we were only able to analyze ¼ of the entire ovary in a reasonable period

of time. Imaging a greater number of ovarian specimens and a greater number of slices/specimen would have increased the probability of detecting COC in the correspondent histologic images. However, these modifications were not practical to implement over the duration of our pilot study. Another limitation of our study was the presence of ring artifacts in the PB-CT images which decreased our ability to resolve ovarian microanatomy. Ring artifacts were attributed to imperfect detector elements and were therefore removed using customized software in the present study [48, 50]. However, removal of the artifacts resulted in an overall reduction in image quality. We propose that use of a different detector type in future studies may improve the quality of synchrotron images.

Infrastructural differences, technical capabilities between SPring-8 and the CLS, and study design must be taken into consideration when visually comparing the PB-CT and TGI-CT images. The study was not designed to quantitatively compare PB-CT and TGI-CT techniques; only a single bovine and a single human ovary were imaged at Spring-8. It is also important to consider that the SPring-8 synchrotron is a larger facility and operates at a higher energy compared to the CLS (8.0 GeV vs. 2.9 GeV). Ovaries were embedded in agarose gel for TGI-CT imaging, compared to preparation in saline for PB-CT. The powerful energy source available at SPring-8 and stabilization of samples may have contributed to the improved contrast in the TGI-CT images of the ovaries. We could not rule out the processes implemented at different synchrotron facilities as confounding factor in this study. The establishment of a TGI-CT imaging system at the CLS and preliminary investigations on the use of TGI-CT to image soft tissues including ovarian samples are currently underway.

Future synchrotron studies should focus on improving PB-CT image quality and comparing our TGI-CT findings with ultrasonography and histology. Imaging of ovaries with a combination of two or more synchrotron-based phase-contrast techniques, such as DEI and PB-CT should also be examined in prospective studies [25]. We hope that our study findings will lead to the development of novel techniques for imaging reproductive tissues *in vivo.* The clinical applications of imaging human ovaries *in vivo* using synchrotron techniques are not fully understood. To ensure patient safety, a suitable energy and safe radiation exposure time is required without compromising the resolution and quality of the images [39, 62]. Developing methods to reduce imaging and reconstruction time will make the synchrotron a more suitable tool for conducting *in vivo* research and clinical work. *In vivo* imaging of ovaries may help

determine the underlying causes of reproductive dysfunctions and enhance our understanding of ovarian anatomy and physiology [63].

In summary, we have determined that PB-CT is as effective for visualizing ovarian macroanatomy (i.e., antral follicles ≥ 2mm and cystic-CL), and superior for detecting ovarian microanatomy (i.e., small antral follicles <2 mm, follicle wall, COC) compared to conventional ultrasonography. Preliminary findings from our SPring-8 study have further indicated that TGI-CT appears to be even more promising than PB-CT for imaging ovaries. Future research should focus on evaluating fresh human ovaries using TGI-CT,

## 4.6 References


1. **Mihu D. and Nugym C. M.** Ultrasonography of the uterus and ovaries. Medical Ultrasonography. 2011; 13(3): 249 - 252.
2. **Gonzalez-Bulnes A., Pallares P. and Vazquez M. I.** Ultrasonographic imaging in small ruminant reproduction. Reprod Domest Anim. 2010; 45 Suppl 29-20.
3. **Pierson R. A. and Ginther O. J.** Ultrasonic imaging of the ovaries and uterus in cattle. Theriogenology. 1988; 29(1): 21-37.
4. **Martin K.** Introduction to B-mode imaging. In: P. Hoskins, K. Martin and A. Thrush, eds. *Diagnostic Ultrasound: Physics and Equipment*. 2nd ed. Cambridge: Cambridge University Press; 2010:1-22.
5. **Pierson R. A., Kastelic J. P. and Ginther O. J.** Basic principles and techniques for transrectal ultrasonography in cattle and horses. Theriogenology. 1988; 29(1): 3-20.
6. **Hearn-Stebbins B., Jaffe R. and Brown H.** Ultrasonographic evaluation of normal pelvic anatomy. In: R. Jaffe, R. Pierson and J. Abramowicz, eds. *Imaging in Infertility and Reproductive Endocrinology.* Philadelphia: J. B. Lippincott Company; 1994:1-21.
7. **Bomsel-Helmreich O.** Ultrasound and the preovulatory human follicle. Oxf Rev Reprod Biol. 1985; 71-22.
8. **Saba L., Guerriero S., Sulcis R., Virgilio B., Melis G. and Mallarini G.** Mature and immature ovarian teratomas: CT, US and MR imaging characteristics. Eur J Radiol. 2009; 72(3): 454-463.
9. **Speca S., Summaria V. and Marano P.** Ultrasonography in gynecology: normal anatomy. European Journal of Ultrasound. 1996; 477-89.
10. **Adams G. P. and Pierson R. A.** Bovine model for study of ovarian follicular dynamics in humans. Theriogenology. 1995; 43(1): 113-120.
11. **Levi S.** The history of ultrasound in gynecology 1950-1980. Ultrasound Med Biol. 1997; 23(4): 481-552.
12. **Parsons A. K.** Imaging the human corpus luteum. J Ultrasound Med. 2001; 20(8): 811-819.
13. **Baerwald A., Adams G. and RA P.** Characterization of ovarian follicular wave dynamics in women. Biol Reprod. 2003; 691023-1031.
14. **Edmondson A. J., Fissore R. A., Pashen R. L. and Bondurant R. H.** The use of ultrasonography for the study of the bovine reproductive tract. I. Normal and pathological ovarian structures. Anim Reprod Sci. 1986; 12(3): 157-165.
15. **Harris R. A., Follett D. H., Halliwell M. and Wells P. N.** Ultimate limits in ultrasonic imaging resolution. Ultrasound Med Biol. 1991; 17(6): 547-558.
16. **Martin K.** Properties, limitations and artefacts of B-mode images. In: P. Hoskins, K. Martin and A. Thrush, eds. *Diagnostic Ultrasound: Physics and Equipment*. Cambridge: Cambridge University Press; 2010:64-74.
17. **Suortti P. and Thomlinson W.** Medical applications of synchrotron radiation. Phys Med Biol. 2003; 48(13): R1-35.
18. **Margaritondo G.** Elements of Synchrotron Light for Biology, Chemistry, & Medical Research. Oxford: Oxford University Press. 2002:1-255.
19. **Arfelli F.** Synchrotron light and imaging stystems for medical radiology. Nucl Instrum Meth A. 2000; 45411-25.

20. **Blattmann H., Gebbers J. O., Bräuer-Krisch E., Bravin A., Le Duc G., Burkard W., Di Michiel M., Djonov V., Slatkin D. N., Stepanek J. and Laissue J. A.** Applications of synchrotron X-rays to radiotherapy. Nucl Instrum Meth A. 2005; 548(1–2): 17-22.
21. **Kocsis M. and Snigirev A.** Imaging using synchrotron radiation. Nucl Instrum Meth A. 2004; 525(1–2): 79-84.
22. **Westneat M. W., Socha J. J. and Lee W. K.** Advances in biological structure, function, and physiology using synchrotron X-ray imaging*. Annu Rev Physiol. 2008; 70119-142.
23. **Thomlinson W.** Current Status and Perspectives of Synchrotron Radiation in Medicine. *V Internatinoal Conference on Applications of Physics in Medicine and Biology*. Trieste, Italy1996:1-9.
24. **Lewis R. A.** Medical applications of synchrotron radiation in Australia. Nucl Instrum Meth A. 2005; 548(1-2): 23-29.
25. **Kitchen M. J., Lewis R. A., Yagi N., Uesugi K., Paganin D., Hooper S. B., Adams G., Jureczek S., Singh J., Christensen C. R., Hufton A. P., Hall C. J., Cheung K. C. and Pavlov K. M.** Phase contrast X-ray imaging of mice and rabbit lungs: a comparative study. The British Journal of Radiology. 2005; 781018-1027.
26. **Arfelli F., Bonvicini V., Bravin A., Cantatore G., Castelli E., Palma L., Michiel M., Fabrizioli M., Longo R., Menk R., Olivo A., Pani S., Pontoni D., Poropat P., Prest M., Rashevsky A., Ratti M., Rigon L., Tromba G., Vacchi A., Vallazza E. and Zanconati F.** Mammography with synchrotron radiaiton: Phase-detection techniques. Radiology. 2000; 215286 - 293.
27. **Zhou S. A. and Brahme A.** Development of phase-contrast X-ray imaging techniques and potential medical applications. Phys Med. 2008; 24(3): 129-148.
28. **Takeda T., Momose A., Itai Y., Jin W. and Hirano K.** Phase-contrast imaging with synchrotron x-rays for detecting cancer lesions. Acad Radiol. 1995; 2(9): 799-803.
29. **Momose A., Washiro W., Takeda Y., Suzuki Y. and Hattori T.** Phase-imaging with an x-ray talbot interferometer. JCPDS-International Centre for Diffraction Data. 2006; 21-30.
30. **Socha J. J., Westneat M. W., Harrison J. F., Waters J. S. and Lee W.-K.** Real-time phase-contrast x-ray imaging: a new technique for the study of animal form and function. BMC Biology. 2007; 5(6).
31. **Snigirev A., Snigireva I., Kohn V., Kuznetsov S. and Schelokov I.** On the possibilities of x-ray phase contrast microimaging by coherent high-energy synchrotron radiation. Rev. Sci. Instrum. 1995; 66(12): 5486 - 5492.
32. **Ritman E.** X-ray phase-based imaging: The third wave. Acad Radiol. 2009; 16909-910.
33. **Schlegel P.** Computed tomography of testicular anatomy and pathology. In: R. Jaffe, R. Pierson and J. Abramowicz, eds. *Imaging in Infertility and Reproductive Endocrinology*. Philadelphia: J.B. Lippincott Company; 1994:307-333.
34. **Wu X., Liu H. and Yan A.** Phase-contrast X-ray tomography: Contrast mechanism and roles of phase retrieval. Eur J Radiol. 2008; 68(3, Supplement): S8-S12.
35. **Basnayaka U., Adams G., Chapman D., Wysokinski T., Belev G., Webb A. and Baerwald A.** Investigating synchrotron techniques for imaging ovaries ex situ. *Canadian Fertility and Andrology Society 58th Annual Meeting*. Westin Ottawa Hotel, Ottawa, ON: Canadian Fertility and Andrology Society; 2012:205.
36. **Chapman D., Thomlinson W., Johnston R. E., Washburn D., Pisano E., Gmur N., Zhong Z., Menk R., Arfelli F. and Sayers D.** Diffraction enhanced x-ray imaging. Phys Med Biol. 1997; 42(11): 2015-2025.

37. **Chapman D., Pisano E., Thomlinson W., Zhong Z., Johnston R. E., Washburn D., Sayers D. and Malinowska K.** Medical applications of diffraction enhanced imaging. Breast Dis. 1998; 10(3-4): 197-207.
38. **Christensen C., Singh J. and Adams G.** The use of diffraction enhanced imaging for bovine soft tissue. *Proceedings of the Fifth Annual Users' Meeting and Workshops of the Canadian Light Source*. University of Saskatchewan, Saskatoon2002:26 (Abstract #35).
39. **Fitzgerald R.** Phase-sensitive X-Ray imaging. Physics Today. 2000; 53(7): 23-26.
40. **Margaritondo G.** Applications of synchrotron light *Elements of synchrotron light for Biology, Chemistry, & Meidcal Research*. Oxford: Oxford University Press; 2002.
41. **Yoon C. Y., Sung D. J., Lee J. H., Kim A. R., Oh C. W., Je J. H., Weon B. M., Seol S. K., Pyun A., Hwu Y., Margaritondo G., Joo K. J. and Yoon D. K.** Imaging of renal and prostate carcinoma with refractive index radiology. Int J Urol. 2007; 14(2): 96-103.
42. **Pinzer B., Cacquevel M., Modregger P., McDonald S., Bensadoun J., Thuering T., Aebischer P. and Stampanoni M.** Imaging brain amyloid deposition using grating-based differential phase contrast tomography. NeuroImage. 2012; 611336 - 1346.
43. **Weitkamp T., David C., Bunk O., Bruder J., Cloetens P. and Pfeiffer F.** X-ray phase radiography and tomography of soft tissue using grating interferometry. Eur J Radiol. 2008; 68(3, Supplement): S13-S17.
44. **Zhu P., Zhang K., Wang Z., Liu Y., Liu X., Wu Z., McDonald S., Marone F. and Stampanoni M.** Low-dose, simple, and fast grating-based X-ray phase-contrast imaging. Proc Natl Acad Sci U S A. 2010; 107(31): 13576-135781.
45. **Pinzer B. R., Cacquevel M., Modregger P., McDonald S. A., Bensadoun J. C., Thuering T., Aebischer P. and Stampanoni M.** Imaging brain amyloid deposition using grating-based differential phase contrast tomography. Neuroimage. 2012; 61(4): 1336-1346.
46. **Wei Z., Wiebe S. and Chapman D.** Ring artifacts removal from synchrotron CT image slices. J Instrum. 2013; In press.
47. **Boin M. and Haibel A.** Compensation of ring artefacts in synchrotron tomographic images. Optics Express. 2006; 14(25): 12071-12075.
48. **Sijbers J. and Postnov A.** Reduction of ring artefacts in high resolution micro-CT reconstructions. Phys. Med. Biol. 2004; 49N247 - N253.
49. **Kyriakou Y., Prell D. and Kalender W.** Ring artifact correction for high-resolution micro CT. Phys. Med. Biol. 2009; 54N385 - N391.
50. **Munch B., Trtik P., Marone F. and Stampanoni M.** Stripe and ring artifact removal with combined wavelet - Fourier filtering. Optics Express. 2009; 17(10): 8567 - 8591.
51. **Gougeon A.** Dynamics for human follicular growth: Morphologic, dynamic, and functional aspects. In: P. Leung and E. Adashi, eds. *The Ovary*. 2nd ed. San Diego, California: Elseiver Academic Press; 2004:25 - 38.
52. **Krause W. and Cutts J.** The female reproduction system. *Concise Text of Histology*. Baltimore: Williams & Wilkins; 1981:367-371.
53. **Crisp T.** Organization of the ovarian follicle and events in its biology: oogenesis, ovulation or atresia. Mutation Research/Reviews in Genetic Toxicology. 1992; 296(1-2): 89 - 106.
54. **Baerwald A., Dauk S., Kanthan R. and Singh J.** Use of ultrasound biomicroscopy to image human ovaries in vitro. Ultrasound Obstet Gynecol. 2009; 34(2): 201-207.

55. **Pfeifer L. F., Siqueira L. G., Adams G. P., Pierson R. A. and Singh J.** In vivo imaging of cumulus-oocyte-complexes and small ovarian follicles in cattle using ultrasonic biomicroscopy. Anim Reprod Sci. 2012; 131(1-2): 88-94.
56. **Wood B. R., Chernenko T., Matthaus C., Diem M., Chong C., Bernhard U., Jene C., Brandli A. A., McNaughton D., Tobin M. J., Trounson A. and Lacham-Kaplan O.** Shedding new light on the molecular architecture of oocytes using a combination of synchrotron Fourier transform-infrared and Raman spectroscopic mapping. Anal Chem. 2008; 80(23): 9065-9072.
57. **Fauser B. C.** Follicle pool depletion: factors involved and implications. Fertil Steril. 2000; 74(4): 629-630.
58. **Kim A. M., Vogt S., O'Halloran T. V. and Woodruff T. K.** Zinc availability regulates exit from meiosis in maturing mammalian oocytes. Nat Chem Biol. 2010; 6(9): 674-681.
59. **Eppig J.** Oocyte control of ovarian follicular development and function in mammals. Reproduction. 2001; 122829 - 838.
60. **Baerwald A. R., Adams G. P. and Pierson R. A.** Form and function of the corpus luteum during the human menstrual cycle. Ultrasound Obstet Gynecol. 2005; 25(5): 498-507.
61. **Adams G. P., Singh J. and Baerwald A. R.** Large animal models for the study of ovarian follicular dynamics in women. Theriogenology. 2012; 78(8): 1733-1748.
62. **Lewis R.** Medical phase contrast x-ray imaging: current status and future prospects. Phys Med Biol. 2004; 493573 - 3583.
63. **Bushnik T., Cook J., Yuzpe A., Tough S. and Collins J.** Estimating the prevalence of infertility in Canada. Hum Reprod. 2012; 27(3): 738-746.

# Chapter 5

# GENERAL DISCUSSION

The ovary is the primary endocrine organ of the female reproductive system. The ovary contains follicles which house the female germ cells or “oocytes”. Hormonal secretions from the ovary regulate the growth of both follicles and oocytes, and regulate development of the uterine lining throughout the menstrual cycle. The development of non-invasive imaging techniques over the past 40 years has provided a greater understanding of female reproductive function and dysfunction. The most common modality for imaging the ovaries *in vivo* is conventional 2D ultrasonography. However, the current resolution of ultrasonography prevents the accurate and consistent detection of the structures <2 mm in the ovaries [1, 2]. As such, the development of novel high-resolution techniques for imaging the ovaries is required.

X-ray imaging has been used for more than 80 years to assist in clinical diagnoses and to guide surgical procedures [3]. The optimization of X-ray techniques has led to the development of various biomedical applications, including synchrotron imaging. The synchrotron accelerates electrons in a circular path, which results in the generation of high-energy electromagnetic light [4]. Medical applications of synchrotron light include, but are not limited to, mammography, angiography, microtomography, bronchography and radiotherapy [3]. The use of early synchrotron technologies for imaging bovine ovaries *ex vivo* was conducted in 2002 at the University of Saskatchewan. The investigators of this proof-of-principle study visualized follicles >4 mm and corpora lutea within the bovine ovary using synchrotron-based Diffraction Enhanced Imaging (DEI) [5]. However, comparisons of synchrotron imaging with conventional imaging methods were not made. To date, the effectiveness of synchrotron techniques for imaging ovaries is not fully understood. The studies conducted as constituents of this thesis are a progression from initial research at the University of Saskatchewan to qualitatively and quantitatively compare synchrotron techniques for imaging bovine and human ovaries with conventional 2D ultrasonography and histology.

We conducted two studies at the Canadian Light Source to examine synchrotron imaging of ovaries *ex vivo*. Diffraction Enhanced Imaging (DEI) (Chapter 3) and Propagation-based Computed Tomography (PB-CT) (Chapter 4) synchrotron techniques were evaluated to image bovine and human ovaries. We conducted a third study, in collaboration with scientists at the

SPring-8 Synchrotron Facility in Japan, to explore the usefulness of Talbot Grating Interferometry-Computed Tomography (TGI-CT) for imaging bovine and human ovaries (Chapter 5). Qualitative and quantitative image attributes obtained with DEI and PB-CT were compared with both conventional 2D ultrasonographic images and histologic images. Qualitative comparisons were made between images obtained using DEI-CT, PB-CT, and TGI-CT. Qualitative endpoints included the detection and differentiation of ovarian structures of interest (i.e., follicles, cell layers comprising the follicle wall, corpora lutea and cumulus oocyte complexes). Quantitative evaluations included comparisons of follicle and luteal diameter, Antral Follicle Count, follicle wall thickness, and the smallest antral follicle detected. The bovine species has been previously validated as a model for studying human reproductive function [6-9]. Thus, bovine ovaries were included in the first phase of our research, with subsequent phases conducted to evaluate preserved and fresh human ovaries. Results from the initial bovine investigations were used to develop and optimize the experimental conditions for imaging human ovaries with the synchrotron. No differences in synchrotron image quality were detected between fresh and preserved ovarian samples; these findings were consistent with previous research to evaluate human articular cartilage [10] and human breast tissue [11].

Overall, we demonstrated that DEI was not an effective technique for visualizing antral follicles, corpora lutea, and cumulus oocyte complexes when compared to ultrasonography and histology. PB-CT was as effective as ultrasonography for measuring follicle and luteal diameter. Furthermore, PB-CT was superior to ultrasonography for detecting small antral follicles <2 mm, the cell layers comprising the follicle wall and cumulus oocyte complexes. However, preliminary data suggested that TGI-CT provided the greatest contrast resolution for visualizing antral follicles, the follicle wall, corpora lutea, cumulus oocyte complexes and vasculature compared to both PB-CT and ultrasonography. Therefore, the general hypothesis that synchrotron techniques would provide greater contrast resolution for imaging ovaries when compared to ultrasonography was partially supported.

### 5.1 Diffraction Enhanced Imaging

DEI enabled the visualization of ovarian follicles ≥2mm and corpora lutea, but not small follicles <2mm, cumulus oocyte complexes, the granulosa and theca cell layers comprising the follicle wall, or vasculature. Approximately 2/3 of all antral follicles and corpora lutea that were

visualized with ultrasonography were visualized with DEI. With that said, Antral Follicle Count (defined as the number of follicles ≥2mm) did not statistically differ between DEI and ultrasonography. Similarly, diameter measurements of follicles >2mm and corpora lutea did not differ among DEI, ultrasonographic, and histologic images. We attributed the lack of statistical differences between groups, at least in part, to a small sample size.

Accurate assessment of the number and diameter of antral follicles and corpora lutea is clinically relevant for monitoring ovarian function during natural menstrual cycles, predicting the ovarian response to human assisted reproductive treatment, as well as determining the timing of the onset of menopause [7, 12, 13]. The differentiation of antral follicles from corpora lutea was not possible using DEI, but it was possible using both ultrasonography and histology. We attributed the challenge in identifying and differentiating follicles from corpora lutea with DEI to the use of projection or planar based imaging rather than CT. We found that the superimposition of follicles and luteal glands in the DEI planar images restricted our ability to differentiate between the various structures. Furthermore, the small variation in the projected refractive indices between the luteal tissues and follicles (presumably due to similar tissue densities) may have contributed to the similarities in contrast [14]. Our findings are similar to previous reports of suboptimal Diffraction Enhanced image interpretation of human breast tissue caused by superimposition of tissue structures [15].

One advantage that planar DEI demonstrated over PB-CT and TGI-CT was a shorter imaging duration, irrespective of the time taken for beam set-up and stabilization. Images were obtained within minutes using planar DEI, but required hours when performing a CT scan. Furthermore, the reconstruction was simpler and less time consuming for planar DEI compared to tomographic reconstruction required for PB-CT. Despite these advantages, planar DEI did not prove to be a superior method for imaging the ovaries compared to conventional 2D ultrasonography. By comparison, DEI-CT is a technique which involves obtaining multiple DEI projection images of a sample. Thus, DEI-CT can be used to construct 3D volumetric images of objects. DEI-CT was not used in the present study. However, it is plausible that DEI-CT will be a more effective modality for visualizing ovarian microanatomy (i.e., follicles, corpora lutea, cumulus oocyte complexes, composition of the follicle wall) compared to planar methods. We postulate that the incorporation of an additional plane of imaging will improve the resolution of follicles and corpora lutea within ovaries [16-18].

## 5.2 Propagation-Based CT Imaging

PB-CT was as effective as ultrasonography for measuring the diameter of follicles ≥2mm and corpora lutea. However, identifying the corpora lutea (especially corpora lutea that did not contain a central cystic cavity) was very challenging in PB-CT images. The image contrast of non-cystic corpora lutea and surrounding stromal tissues was very similar, making it difficult to identify the corpora lutea within the ovaries. Cystic corpora lutea were more easily visualized with PB-CT because of a greater contrast resolution between the fluid within the cavity and the neighboring luteal tissues. The difference in follicular and luteal echogenicity in the ultrasonographic images was greater (i.e., more obvious) compared to the difference in follicular versus luteal contrast in the PB-CT images. Therefore, we concluded that ultrasonography was more effective than PB-CT for differentiating corpora lutea and follicles. The imaging of follicles and corpora lutea is crucial for evaluating female reproductive function and dysfunction. It has been previously shown that the brightness of pixels in ultrasonographic images changes during stages the menstrual/estrous cycle, in association with morphologic and endocrinologic aspects of follicle and luteal development [19, 20]. Similar studies evaluating synchrotron imaging of ovarian follicle and luteal development *in vivo* have not yet been conducted.

PB-CT provided an advantage over ultrasonography for detecting small antral follicles <2 mm (minimum diameter = 0.85 ± 0.42 mm for PB-CT versus 2.18 ± 0.18 mm for ultrasonography). Similarly, spherical structures protruding from the follicle wall (resembling cumulus oocyte complexes) as well as the cell layers comprising the follicle wall were visualized with PB-CT, but not ultrasonography. It has been previously documented that conventional ultrasonography is not a reliable tool for visualizing cumulus oocyte complexes during the spontaneous menstrual cycle [21] or in-vitro fertilization cycles [22]. Moreover, detection of cumulus oocyte complexes using ultrasonography has been limited to only those follicles that are >15 mm in diameter. Researchers in our lab have recently documented the visualization of follicles <2 mm and cumulus oocyte complexes in human ovaries [23] and domestic farm animals [24] using ultrasound biomicroscopy. However, the depth of tissue penetration with ultrasound biomicroscopy is limited, depending on the resolution of the transducer that you use [23]. In the present study, we were able to visualize the cumulus oocyte complexes in follicles as small as 2 mm in diameter, while imaging the entire ovary. Limitations to the depth of imaging observed previously with ultrasound biomicroscopy were not observed with PB-CT imaging.

Therefore, we conclude that PB-CT synchrotron imaging provides an advantage over both conventional and biomicroscopic ultrasonography for imaging the cumulus oocyte complexes.

Doppler ultrasonographic imaging is used to assess ovarian vasculature in relation to the normal follicular and corpora lutea function as well as the development of ovarian malignancies [25-27]. Doppler ultrasonography was not a focus of this thesis and was not evaluated in our investigations. However, vasculature was visualized using PB-CT (but not DEI), following the injection of radiographic contrast into the ovarian artery of 1/3 bovine ovaries. Vasculature surrounding individual dominant follicles was visualized, albeit not consistently. Technical difficulties in injecting contrast into the ovarian arteries (i.e., ligation of very small vessels, time-sensitive nature of the injections post-ovariectomy) may have contributed, in part, to the poor visualization of vasculature in our samples. Continued research should be conducted to determine the effectiveness of DEI and PB-CT synchrotron techniques for imaging bovine and human ovaries.

### 5.3 Talbot Grating Interferometry-CT Imaging

TGI-CT imaging of bovine and human ovaries was conducted as a case series due to technical, practical and ethical challenges in shipping ovarian tissues to Japan for evaluation at the SPring-8 facility. As a result, TGI-CT was conducted on a single preserved bovine ovary and a single preserved human ovarian tissue segment. We visually observed a remarkable improvement in contrast in the TGI-CT images compared to PB-CT images. Specifically, we saw a clear delineation of individual structures within the ovary, such as follicles, non-cystic and cystic corpora lutea, granulosa and theca cells layers of the follicle wall, cumulus oocyte complexes, and vasculature. Small antral follicles <2mm were detected in TGI-CT, but not PB-CT or ultrasonographic images. The contrast resolution of the TGI-CT images also show promise for visualizing pre-antral follicles (i.e., <0.2 mm) which is not possible with current ultrasonographic technology. The entire duration of follicle development from the primordial to preovulatory stage is approximately 175 days [28]. Development of antral follicles beyond 2 mm comprises only about 15 days of the entire lifespan of follicle development [28]. Thus, visualization of small antral follicles is necessary to increase our knowledge about early stages of follicle growth, which are not well understood. A greater understanding about pre-antral and early antral folliculogenesis has clinical applications for monitoring follicle development,

determining early symptoms of ovarian pathophysiology and for improving treatments for infertility.

Cumulus oocyte complexes were more consistently observed protruding from the follicle wall in TGI-CT versus PB-CT images. Furthermore, the oocyte was observed as a bright circular structure within the cumulus oocyte complexes in TGI-CT, but not PB-CT, images. In contrast, no cumulus oocyte complexes were observed ultrasonographically in our study. Currently, oocytes are visualized histologically (following surgical removal of the ovaries) or by microscopic evaluation of aspirated oocytes *in vitro*. More recently, ultrasound biomicroscopy has been used to image bovine cumulus-oocyte complexes *in vivo*; the resolution of the images obtained and the depth of penetration for imaging the ovaries was limited [24]. In addition, synchrotron-based FT-IR research methods have been used to examine the composition and biochemical properties of animal oocytes in-culture [29, 30]. Our findings are novel in that we documented the visualization of both cumulus oocyte complexes and oocytes within the cumulus cells in both bovine and human ovaries. The resolution of images obtained in the present study appeared greater than that obtained in previous studies [24, 29, 30]. Based on these exciting findings, we believe that TGI-CT has potential to provide great benefit for evaluating oocyte development, documenting ovulation, and increasing our understanding of follicle-oocyte interactions in both animals and humans [31]. We believe that TGI-CT methods used in our research may also be applied to the future development of novel synchrotron imaging techniques for other soft tissues, such as tissues of the breast, brain, heart, kidney and prostate.

We believe that improvements in image quality obtained with TGI-CT versus PB-CT were primarily attributed to differences in hardware and software (i.e., technical capabilities) available at the SPring-8 versus CLS synchrotron facilities. Statistical comparisons of TGI-CT versus PB-CT images were not possible due to the small number of samples imaged with TGI-CT. However, the establishment of a TGI-CT system is currently underway at the CLS. We expect that TGI-CT images obtained at the CLS will be similar to those obtained at SPring-8 in Japan. The establishment of TGI-CT at the CLS has the potential to markedly improve biomedical imaging of soft tissues, and will be an important step for the development of novel, *in vivo* high-resolution synchrotron imaging of soft tissues.

## 5.4 Future Directions and Clinical Applications

The results presented in the thesis have provided important information about imaging of ovaries using synchrotron techniques. We have come a long way in our ability to image ovarian structure and function. However, continued research is required to build upon the present findings to further evaluate synchrotron techniques for imaging ovaries. We believe that strategies to improve synchrotron ovarian imaging in the future should include optimizing X-ray energy, increasing signal filtrations to reduce noise, and enhancing detector sensitivity to minimize ring artifacts. Findings from the studies presented indicate that TGI-CT is a more promising technology than DEI and PB-CT for imaging ovaries. Therefore, we propose that future studies should focus on quantitatively comparing TGI-CT of fresh human ovaries with ultrasonography and histology to confirm whether TGI-CT is superior to conventional imaging techniques. In addition, the effectiveness of DEI-CT for imaging human ovaries is not currently known and requires further investigation [32].

The biomedical imaging applications of synchrotron techniques have been initially investigated in animal and human tissue samples or whole animals post-mortem. Limited studies have been conducted in live animals and no research has been conducted yet in men and women *in vivo*. Synchrotron-based PB-CT techniques have been used previously to examine lung function in live mice [33] and rabbits [34]. PB-CT imaging in live mice was found to be effective for visualizing fine micron sized structures, as well as natural movements of internal organs [35]. A clinical system for imaging human breast tissues using synchrotron phase contrast techniques has already been implemented at the ELETTRA synchrotron in Italy [36, 37]. Further research is required to establish a synchrotron-based system for *in vivo* imaging of human and animal reproductive organs, including ovaries. Synchrotron imaging of ovaries has the potential to be used for detecting reproductive dysfunction, including benign and malignant ovarian cysts and masses. Clinical *in vivo* imaging of ovaries with the synchrotron will require a suitable energy and safe radiation exposure time without compromising the image contrast [38-40]. Tomographic imaging of live humans and animals may be challenging because, unlike conventional CT imaging, the sample is rotated and the X-ray beam is stationary. With that said, the speed at which the samples are rotated is slow (i.e., 20 seconds for one degree turn) and should not lead to patient discomfort. Living animals or humans can also produce motion artifacts due to subtle movements such as respiration [41]. Continued research to optimize

imaging parameters, decrease imaging time, and maximize patient safety and comfort can help to overcome the present challenges in synchrotron imaging of ovaries. Synchrotron techniques have the potential to image soft tissues at greater resolution and lower radiation exposure compared to X-ray CT and Magnetic Resonance Imaging. The ultimate goal of continued research in this area is to incorporate synchrotron techniques into clinical practice that will likely improve patient care and well-being.

### 5.5 Significance

As part of the research work presented in this thesis, we were able explore the advantages and limitations of synchrotron based-imaging techniques for visualizing human and bovine ovaries. We were able to determine that synchrotron techniques, especially TGI-CT, are capable of detecting structures that are undetected by conventional ultrasonographic imaging methods (i.e., oocyte, cumulus oocyte complexes, cell layers of the follicle wall and follicles <2mm). Therefore, the synchrotron holds great potential for investigating early antral and pre-antral folliculogenesis, oogenesis and luteogenesis. The improved contrast resolution of synchrotron images also show promise for differentiating between normal ovaries and those containing pathology (i.e., ovarian tumors and malignant cysts). As such, the synchrotron can be used as a tool for understanding early determinants of fertility. Our research methodology and findings may be applied to synchrotron imaging of other types of soft tissues, such as breast, prostate and kidney. Furthermore, our work can be used as a guide for optimizing beamline instrumentation and image reconstruction programs for improving synchrotron biomedical imaging in Canada and abroad.

### 5.6 Summary

In summary, DEI was not found to be an effective technique for evaluating ovarian anatomy compared to ultrasonography. In contrast, PB-CT was equally effective to ultrasonography for detecting and measuring follicles ≥2mm and corpora lutea. The resolution for visualizing structural details within follicles and corpora lutea was superior for PB-CT versus ultrasonography; however, PB-CT did not allow the differentiation of follicles from non-cystic corpora lutea within the ovaries. Finally, we obtained preliminary data to indicate that TGI-CT synchrotron imaging provides the greatest contrast resolution for visualizing ovarian macro- and

micro-anatomy, including follicles, corpora lutea, the cell layers comprising the follicle wall and oocytes, compared to both PB-CT and conventional 2D ultrasonography. We believe that future research to develop synchrotron methods for imaging soft tissues in animals and humans should be focused on TGI-CT imaging.

## 5.7 References


1. **Baerwald A., Adams G. and RA P.** Characterization of ovarian follicular wave dynamics in women. Biol Reprod. 2003; 691023-1031.
2. **Edmondson A. J., Fissore R. A., Pashen R. L. and Bondurant R. H.** The use of ultrasonography for the study of the bovine reproductive tract. I. Normal and pathological ovarian structures. Anim Reprod Sci. 1986; 12(3): 157-165.
3. **Suortti P. and Thomlinson W.** Medical applications of synchrotron radiation. Phys Med Biol. 2003; 48(13): R1-35.
4. **Margaritondo G.** Elements of synchrotron light for biology, chemistry, & medical research. Oxford: Oxford University Press; 2002:1-255.
5. **Christensen C., Singh J., Adams G., Choo-Smith L.-P. and Jackson M.** Infrared and Raman spectroscopic imaging of bovine corpora lutea. Microsc Microanal. 2004; 10(Suppl 2): 1324-1325.
6. **Adams G. P. and Pierson R. A.** Bovine model for study of ovarian follicular dynamics in humans. Theriogenology. 1995; 43(1): 113-120.
7. **Adams G. P., Singh J. and Baerwald A. R.** Large animal models for the study of ovarian follicular dynamics in women. Theriogenology. 2012; 78(8): 1733-1748.
8. **Baerwald A. R.** Human antral folliculogenesis: what we have learned from the bovine and equine models. Anim. Reprod. 2009; 6(1): 20-29.
9. **Baerwald A. R., Adams G. P. and Pierson R. A.** Ovarian antral folliculogenesis during the human menstrual cycle: a review. Hum Reprod Update. 2012; 18(1): 73-91.
10. **Mollenhauer J., Aurich M. E., Zhong Z., Muehleman C., Cole A. A., Hasnah M., Oltulu O., Kuettner K. E., Margulis A. and Chapman L. D.** Diffraction-enhanced X-ray imaging of articular cartilage. Osteoarth Cartilage. 2002; 10(3): 163-171.
11. **Arfelli F.** Synchrotron light and imaging stystems for medical radiology. Nucl Instrum Meth A. 2000; 45411-25.
12. **Gibreel A., Maheshwari A., Bhattacharya S. and Johnson N.** Ultrasound tests of ovarian reserve; a systematic review of accuracy in predicting fertility outcomes. Hum Fertil (Camb). 2009; 1295 - 106.
13. **Ng E., Tang O. and Ho P.** The significance of the number of antral follicles prior to stimulation in predicting ovarian responses in an IVF programme. Hum Reprod. 2000; 151937 -1942.
14. **Chapman D., Thomlinson W., Johnston R. E., Washburn D., Pisano E., Gmur N., Zhong Z., Menk R., Arfelli F. and Sayers D.** Diffraction enhanced x-ray imaging. Phys Med Biol. 1997; 42(11): 2015-2025.
15. **Pagot E., Fiedler S., Cloetens P., Bravin A., Coan P., Fezzaa K., Baruchel J., Hartwig J., Von Smitten K., Leidenius M., Karjalainen-Lindsberg M. and Keyrilainen J.** Quantitative comparison between two phase contrast techniques: diffraction enhanced imaging and phase propagation imaging. Phys Med Biol. 2005; 50(4): 709 - 724.
16. **Bravin A., Keyrilainen J., Fernandez M., Fiedler S., Nemoz C., Karjalainen-Lindsberg M. L., Tenhunen M., Virkkunen P., Leidenius M., von Smitten K., Sipila P. and Suortti P.** High-resolution CT by diffraction-enhanced x-ray imaging: mapping of breast tissue samples and comparison with their histo-pathology. Phys Med Biol. 2007; 52(8): 2197-2211.

17. **Hu C Z. T., Zhang L, Li H, Zhao X, Luo S**. Information extraction and CT reconstruction of liver images based on diffraction enhanced imaging. Prog Nat Sci. 2009; 19955-962.
18. **Yuasa T., Hashimoto E., Maksimenko A., Sugiyama H., Arai Y., Shimao D., Ichihara S. and Ando M.** Highly sensitive detection of the soft tissues based on refraction contrast by in-plane diffraction-enhanced imaging CT. Nucl Instrum Meth A. 2008; 591(3): 546-557.
19. **Singh J., Pierson R. A. and Adams G. P.** Ultrasound image attributes of the bovine corpus luteum: structural and functional correlates. J Reprod Fertil. 1997; 109(1): 35-44.
20. **Baerwald A. R., Adams G. P. and Pierson R. A.** Form and function of the corpus luteum during the human menstrual cycle. Ultrasound Obstet Gynecol. 2005; 25(5): 498-507.
21. **Kerin J. F., Edmonds D. K., Warnes G. M., Cox L. W., Seamark R. F., Matthews C. D., Young G. B. and Baird D. T.** Morphological and functional relations of Graafian follicle growth to ovulation in women using ultrasonic, laparoscopic and biochemical measurements. Br J Obstet Gynaecol. 1981; 88(2): 81-90.
22. **Cacciatore B., Liukkonen S., Koskimies A. I. and Ylostalo P.** Ultrasonic detection of a cumulus oophorus in patients undergoing in vitro fertilization. J In Vitro Fert Embryo Transf. 1985; 2(4): 224-228.
23. **Baerwald A., Dauk S., Kanthan R. and Singh J.** Use of ultrasound biomicroscopy to image human ovaries in vitro. Ultrasound Obstet Gynecol. 2009; 34(2): 201-207.
24. **Pfeifer L. F., Siqueira L. G., Adams G. P., Pierson R. A. and Singh J.** In vivo imaging of cumulus-oocyte-complexes and small ovarian follicles in cattle using ultrasonic biomicroscopy. Anim Reprod Sci. 2012; 131(1-2): 88-94.
25. **Secil M. and Dogra V. S.** Color flow doppler evaluation of uterus and ovaries and its optimization techniques. Ultrasound Clinics. 2008; 3(3): 461-482.
26. **Ottander U., Solensten N.-G., Bergh A. and Olofsson J. I.** Intraovarian blood flow measured with color doppler ultrasonography inversely correlates with vascular density in the human corpus luteum of the menstrual cycle. Fertil Steril. 2004; 81(1): 154-159.
27. **Deb S., Kannamannadiar J., Campbell B. K., Clewes J. S. and Raine-Fenning N. J.** The interovarian variation in three-dimensional ultrasound markers of ovarian reserve in women undergoing baseline investigation for subfertility. Fertil Steril. 2011; 95(2): 667-672.
28. **Gougeon A.** Human ovarian follicular development: From activation of resting follicles to preovulatory maturation. Ann Endocrinol (Paris). 2010; 71(3): 132-143.
29. **Wood B. R., Chernenko T., Matthaus C., Diem M., Chong C., Bernhard U., Jene C., Brandli A. A., McNaughton D., Tobin M. J., Trounson A. and Lacham-Kaplan O.** Shedding new light on the molecular architecture of oocytes using a combination of synchrotron Fourier transform-infrared and Raman spectroscopic mapping. Anal Chem. 2008; 80(23): 9065-9072.
30. **Carnevali O., Conti C., Ferraris P., Garavaglia M. G., Gioacchini G., Giorgini E., Rubini C., Sabbatini S. and Tosi G.** FT-IR Microspectroscopy on molecular building of Zebrafish oocytes. J Mol Struct. 2009; 938(1–3): 207-213.
31. **Eppig J.** Oocyte control of ovarian follicular development and function in mammals. Reproduction. 2001; 122829 - 838.

32. **Ketcham R. and Carlson W.** Acquisition, optimization and interpretation of X-ray computed tomographic imagery: applications to the geosciences. Comput Geosci. 2001; 27381-400.
33. **Yue W., Zhang G., Liu P., Sun J., Hwu Y., Je J. H., Tan M. and Li Y.** Aerosol-induced lung injuries observed by synchrotron radiation X-ray phase-contrast imaging technique. Nucl Instrum Meth B. 2007; 262(2): 304-312.
34. **Lewis R., Yagi N., Kitchen M., Morgan M., Paganin D., Siu K., Pavlov K., Williams I., Uesugi K., Wallace M., Hall C., Whitley J. and Hooper S.** Dynamic imaging of the lungs using x-ray phase contrast. Phys Med Biol. 2005; 505031-5040.
35. **Lee K. H., Hwu Y. K., Je J. H., Tsai W. L., Choi E. W., Kim Y. C., Kim H. J., Seong J. K., Yi S. W., Ryo H. S. and Margaritondo G.** Synchrotron radiation imaging of internal structures in live animals. Yonsei Med J. 2002; 43(1): 25-30.
36. **Dreossi D., Abrami A., Arfelli F., Bregant P., Casarin K., Chenda V., Cova M. A., Longo R., Menk R. H., Quai E., Quaia E., Rigon L., Rokvic T., Sanabor D., Tonutti M., Tromba G., Vascotto A., Zanconati F. and Castelli E.** The mammography project at the SYRMEP beamline. Eur J Radiol. 2008; 68(3, Supplement 1): S58-S62.
37. **Pani S., Longo R., Dreossi D., Montanari F., Olivo A., Arfelli F., Bergamaschi A., Poropat P., Rigon L., Zanconati F., Dalla Palma L. and Castelli E.** Breast tomography with synchrotron radiation: preliminary results. Phys Med Biol. 2004; 49(9): 1739-1754.
38. **Fitzgerald R.** Phase-sensitive X-ray imaging. Physics Today. 2000; 53(7): 23-26.
39. **Lewis R.** Medical phase contrast x-ray imaging: current status and future prospects. Phys Med Biol. 2004; 493573 - 3583.
40. **Zhang X., Yang X. R., Chen Y., Li H. Q., Liu W. Y., Yuan Q. X. and Chen S. L.** Diffraction-enhanced radiography of various mouse organs. Am J Roentgenol. 2010; 195(3): 545-549.
41. **Donnelley M., Parsons D., Morgan K. and Siu K.** Animals in synchrotrons: Overcoming challenges for high-resolution, live, small-animal imaging. In: K. K. W. Siu, ed. *6th International Conference on Medical Applications of Synchrotron Radiation.* Vol 1266: American Institute of Physics; 2010:30-34.

# Chapter 6

## GENERAL CONCLUSIONS

The studies conducted in this thesis provided detailed information regarding synchrotron biomedical techniques for imaging bovine and human ovaries, in comparison to ultrasonography and histology. The specific conclusions derived from the study findings are listed below.

1. DEI did not provide an advantage over ultrasonography for detecting ovarian anatomy.
    a. DEI was as effective as ultrasonography for measuring antral follicles ≥2 mm and corpora lutea; however, the resolution for differentiating follicular and luteal anatomy was inferior with DEI.
    b. Neither DEI nor ultrasonography allowed the visualization of antral follicles <2 mm, follicle wall and cumulus oocyte complexes.

2. PB-CT imaging provided an advantage over ultrasonography for visualizing ovarian anatomy.
    a. PB-CT was as effective as ultrasonography for detecting and measuring follicles ≥2 mm and cystic corpora lutea. However, the ability to differentiate antral follicles from non-cystic corpora lutea was inferior with PB-CT versus ultrasonography.
    b. PB-CT was superior to ultrasonography for visualizing small antral follicles <2 mm, the theca and granulosa cell layers comprising the follicle wall, and cumulus oocyte complexes.

3. TGI-CT appeared to provide an advantage over ultrasonography for visualizing both macro- and microanatomy of the ovary.
    a. TGI-CT provided superior contrast resolution for visualizing antral follicles, theca and granulosa cell layers comprising the follicle wall, cystic and non-cystic corpora lutea, cumulus oocyte complexes, oocytes, and vasculature, compared to both PB-CT and ultrasonography.